



LEHIGH  
UNIVERSITY

Library &  
Technology  
Services

The Preserve: Lehigh Library Digital Collections

# Origin and characteristics of erbium emission in tellurite glasses and fibers.

## Citation

Marjanovic, Sasha - Lehigh University. *Origin and Characteristics of Erbium Emission in Tellurite Glasses and Fibers*. 2004, <https://preserve.lehigh.edu/lehigh-scholarship/graduate-publications-theses-dissertations/theses-dissertations/origin-0>.

Find more at <https://preserve.lehigh.edu/>

*This document is brought to you for free and open access by Lehigh Preserve. It has been accepted for inclusion by an authorized administrator of Lehigh Preserve. For more information, please contact [preserve@lehigh.edu](mailto:preserve@lehigh.edu).*

**Origin and Characteristics of Erbium Emission in Tellurite Glasses and Fibers**

by

Sasha Marjanovic

Presented to the Graduate and Research Committee

of Lehigh University

in Candidacy for the Degree of

Doctor of Philosophy

in

Physics

Lehigh University

June 24<sup>th</sup>, 2004

UMI Number: 3147324

### INFORMATION TO USERS

The quality of this reproduction is dependent upon the quality of the copy submitted. Broken or indistinct print, colored or poor quality illustrations and photographs, print bleed-through, substandard margins, and improper alignment can adversely affect reproduction.

In the unlikely event that the author did not send a complete manuscript and there are missing pages, these will be noted. Also, if unauthorized copyright material had to be removed, a note will indicate the deletion.

**UMI<sup>®</sup>**

---

UMI Microform 3147324

Copyright 2005 by ProQuest Information and Learning Company.

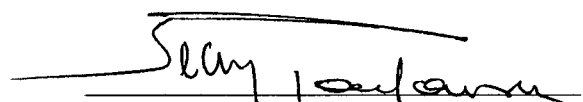
All rights reserved. This microform edition is protected against unauthorized copying under Title 17, United States Code.

ProQuest Information and Learning Company  
300 North Zeeb Road  
P.O. Box 1346  
Ann Arbor, MI 48106-1346

Approved and recommended for acceptance as a dissertation in partial fulfillment of the requirements for the degree of Doctor of Philosophy in Physics

June, 2004


Date

  
Prof. Jean Toulouse, ~~Dissertation~~  
Director, Chair of Committee

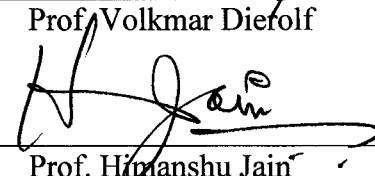
July, 2004

Accepted date

Committee Members

  
Prof. Volkmar Dierolf

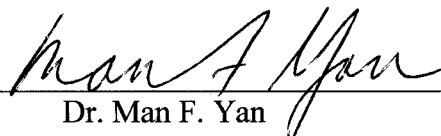
8/12/04  
date

  
Prof. Himanshu Jain

7/12/04  
date

  
Dr. Ahmet R. Kortan

6/22/04  
date

  
Dr. Man F. Yan

July 28, 2004  
date

*Посвећено Сашки*

## Acknowledgments

I wish to acknowledge the help and support given to me by my dissertation committee and other Lehigh University members. I am especially grateful to Jean Toulouse for his strong guidance of my thesis and for his valuable support of my research in general. I owe a great debt of gratitude to Ahmet R. Kortan from Lucent Technologies (later OFS Laboratories) for his time, for use of his research facilities, and for his generous help and continuous encouragement at every stage of my research. He was nothing but an excellent instructor and colleague. I am extremely appreciative of Volkmar Dierolf for his tremendous assistance and support. It is my pleasure to acknowledge Himanshu Jain for helping me understand the material science aspect of tellurite glasses. I also wish to express my appreciation of Man F. Yan from OFS Laboratories for his useful comments, suggestions and for supplying the alumina-silica fibers used in this study.

Sincere thanks go to Christian Sandmann and Zackery D. Fleischman for their help in measuring erbium emission spectra at low temperature. Additionally, I want to say thanks to Radha K. Pattnaik, Iavor Velchev, Michael Stavola and Gang Shi for their assistance at crucial time. I thank Jas Sanghera from Naval Research Laboratory for tungsten-tellurite samples. Finally, I thank Sheldon H. Radin for his offer to me for PhD studies at Lehigh University.

*The deepest gratitude goes to my mother and father, who always wanted only the best for me. Special thanks are in order to my wife Paulina for her dedication as a wife of*

*a physicist. She deserves my whole respect for that. In addition, I thank my family and friends for their kindness and generosity toward me.*

*I was told that having a child during graduate school would, if not jeopardize, than definitely slow down the graduation process. Cutting the umbilical cord of Aleksandra and seeing her growing day by day gave to me at the most crucial time even more strength to maintain the high course of my research goals. It is because of these reasons why I dedicate this thesis to her. It would be the greatest joy to me as a father if I see one day that this modest gesture would become her inspiration for a bright future.*

# Contents

<b>Abstract</b>	1
<b>Chapter 1 Introduction</b>	2
<b>Bibliography</b>	8
<b>Chapter 2 Background</b>	10
2.1 Rare earth elements in oxide glasses.....	10
2.2 Quantum mechanics description of dipole transitions and Judd-Ofelt theory...	20
2.3 Electronic polarizability and index of refraction.....	27
<b>Bibliography</b>	32
<b>Chapter 3 Techniques and materials</b>	35
3.1 Samples preparation.....	35
3.2 Raman spectroscopy.....	39
3.3 X-ray photoelectron spectroscopy (XPS).....	44
3.4 Fiber characterization.....	47
3.5 High-resolution combined excitation-emission spectroscopy (CEES).....	50
3.6 Electron-phonon interaction.....	52
<b>Bibliography</b>	52
<b>Chapter 4 Results</b>	54
4.1 Raman spectra.....	55
4.1.1 Raman effect in zinc-tellurite glasses.....	55



4.1.2 Raman spectra of tungsten-tellurite glasses.....	65
4.2 An increase of glass transition temperature with WO <sub>3</sub> .....	74
4.3 XPS data.....	75
4.4 Er <sup>3+</sup> emission.....	78
4.5 CEES results.....	86
4.6 Absorption results.....	99
<b>Bibliography</b>	107
<b>Chapter 5 Discussion</b>	110
5.1 Influence of dopants on the Raman spectra of TeO <sub>2</sub> glasses.....	110
5.2 Supporting XPS results.....	116
5.3 High refractive index of tellurite glasses.....	119
5.3.1 Electronic polarizability and ion electronegativity in doped tellurite glasses	120
5.3.2 Dependence of polarizability on the nature and the number of network bonds	122
5.3.3 Dependence of polarizability on network connectivity.....	123
5.4 The role of phonons in erbium emission.....	125
<b>Bibliography</b>	133
<b>Chapter 6 Conclusion</b>	136
<b>Publications and presentations</b>	137
<b>Selected publications</b>	139
<b>Selected presentations</b>	141
<b>Vita</b>	144

## List of Tables

2.1 Calculated Judd-Ofelt parameters for different oxide glasses.....	27
2.2 Optical characteristics of binary tellurite glasses.....	29
2.3 Average electronegativity & electronic polarizability of ZnO & WO <sub>3</sub> tellurite glass	31
3.1 Sodium-zinc-tellurite glass compositions used in experiments.....	35
3.2 Alkali-tungsten-tellurite glass compositions used in experiments.....	37
3.3 Glass composition and glass transition temperature.....	39
4.1 The oscillator strengths of Er <sup>3+</sup> in sodium-zinc-tellurite & alumina-silica fibers.	102
4.2 Refractive indexes, Judd-Ofelt parameters & luminescence lifetime of fibers used.	103
5.1 Number of network bonds per unit volume for ZnO and WO <sub>3</sub> tellurite glass....	122
5.2 Bond strengths for some natural diatomic molecules.....	123
5.3 The energy separation between emission peaks observed in FIG. 5.3.....	129

## List of Figures

2.1 A portion of the energy levels for $\text{Pr}^{3+}$ ions with $4f$ -electrons .....	13
2.2 $\text{Er}^{3+}$ energy levels split due to the Stark effect, inhomogeneous and homogeneous broadening .....	15
2.3 Energy level diagram of $\text{Er}^{3+}$ ion .....	17
2.4 Multiphonon decay rates for rare-earth ions in five oxide glasses plotted as a function of the energy gap to the next-lower level.....	18
3.1 Ternary diagram of $\text{Na}_2\text{O}$ - $\text{ZnO}$ - $\text{TeO}_2$ glasses used in this study.....	36
3.2 Ternary diagram of $\text{Li}_2\text{O}$ - $\text{WO}_3$ - $\text{TeO}_2$ glasses used in this study.....	38
3.3 Conservation Laws for the Vibrational Raman effect in crystalline solids.....	42
3.4 Binding energy of: a) The O-1s and b) the Te-3d <sub>5/2</sub> electrons.....	45
3.5 A typical experimental setup used for fiber measurements.....	47
3.6 Mechanical splice.....	48
3.7 The cross-section of the sample with capillary tube and Er-doped tellurite fiber inside. Magnification (from upper left to bottom right): 5x, 20x, 50x, 150x.....	49
3.8 Schematic diagram of high-resolution CEES (courtesy of C. Sandmann).....	50
3.9 A typical CEES contour spectra (courtesy of C. Sandmann).....	51
4.1. Peak deconvolution of unpolarized Raman spectra of ternary tellurite glasses containing 5% $\text{Na}_2\text{O}$ and 15% $\text{ZnO}$ , with fitting results, at the room temperature...	56

4.2 Evolution of the Raman spectra during the crystallization of $\text{TeO}_2$ glass into the $\gamma$ -phase (crosses) and then into the $\alpha$ -phase (black circles) [Noguera <i>et al.</i> ]	60
4.3 Raman spectra of zinc-tellurite glasses: a) binary, and b) with 5% $\text{Na}_2\text{O}$ ; unpolarized, at room temperature.	61
4.4 Peak ratio A/C dependence on dopants concentration (lines are drawn through data symbols). Insert shows the B peak intensity dependence on concentration.	63
4.5 Peak ratio A/C dependence on dopants concentration (lines are drawn through data symbols).	64
4.6 A model for $\text{WO}_3$ - $\text{TeO}_2$ glasses proposed by Kozhukharov <i>et al.</i>	66
4.7 The comparison of the unpolarized Raman spectra of sodium-zinc-tellurite with tungsten-telluride glasses.	67
4.8 Peak deconvolution of unpolarized Raman spectra of $5.0\text{Li}_2\text{O} \cdot 24.9\text{WO}_3 \cdot 70\text{TeO}_2$ , at room temperature.	68
4.9 Unpolarized Raman spectra of tungsten-telluride glasses with constant concentration of lithium, at the room temperature.	71
4.10 Unpolarized Raman spectra of tungsten-telluride glasses with constant concentration of tungsten, at the room temperature.	72
4.11 Unpolarized Raman spectra of tungsten-telluride glasses with $\text{Li} \rightarrow \text{K}$ substitution, at the room temperature.	73
4.12 Glass transition temperature of $10\text{Li}_2\text{O} \cdot x\text{WO}_3 \cdot (90-x)\text{TeO}_2$ glasses (with 0.1 wt% $\text{Tm}_2\text{O}_3$ ) [Lim <i>et al.</i> ]	75
4.13 Dependence on $\text{TeO}_2$ concentration of: a) NBO and b) $\text{N}_3$ (lines are drawn through data symbols).	76

4.14 a) O-1s XPS spectra, b) Te-3d XPS spectra of $x\text{K}_2\text{O} \cdot (10-x)\text{Li}_2\text{O} \cdot 25\text{WO}_3 \cdot 65\text{TeO}_2$ glass system [Lim <i>et al.</i> ]	77
4.15 ASE spectra in an Er-Te fiber, a counter-pumping with: a) 980 nm and b) 1480 nm laser	80
4.16 ASE spectra of Er-doped tellurite fiber for different fiber lengths	82
4.17 Output signal power vs. wavelength	83
4.18 a) The $\text{Er}^{3+}$ emission spectra for 1.3 m long tellurite and alumina-silica fibers, counter-pumped with 980 nm light; b) the $\text{Er}^{3+}$ emission spectra for 1.3 m long tellurite and alumina-silica fibers, co- and counter-pumped with 980 nm light, for a pump power of 75 mW	84
4.19 CEES spectra of $\text{Er}^{3+}$ in alumina-silica glass, near 1.5 $\mu\text{m}$ , at room T	87
4.20 CEES spectra of $\text{Er}^{3+}$ in zinc-tellurite glass, near 550 nm, at room T	88
4.21 The $5\text{Na}_2\text{O} \cdot 15\text{ZnO} \cdot 79\text{TeO}_2$ sample, at different T: a) CEES spectra, b) normalized CEES spectra	89
4.22 The $\text{Er}^{3+}$ emission in $\text{ZnO-TeO}_2$ and $\text{Al}_2\text{O}_3\text{-SiO}_2$ fibers, near 550 nm: a) at $T = 4 \text{ K}$ and b) at $T = 260 \text{ K}$	91
4.23 The $\text{Er}^{3+}$ emission spectra in $\text{Al}_2\text{O}_3\text{-SiO}_2$ , $\text{ZnO-TeO}_2$ and $\text{WO}_3\text{-TeO}_2$ , near 1.5 $\mu\text{m}$ , at: a) $T = 4.2 \text{ K}$ ; b) room T	93
4.24 Wavelength assignment of $\text{Er}^{3+}$ ion fluorescence from the $^4\text{I}_{13/2}$ to the $^4\text{I}_{15/2}$ for an $\text{Al}_2\text{O}_3\text{-SiO}_2$ glass host: (a) the Stark levels and related fluorescence transition, and (b) the spectral composition of the room-temperature fluorescence for the alumina-silica host [Desurvire & Simpson]	94

4.25 Deconvolution of peaks of $\text{Er}^{3+}$ emission spectrum in three different host materials, at $T = 4.2 \text{ K}$ : (a) alumina-silica, (b) zinc-tellurite, and (c) tungsten-tellurite.....	96
4.26 Deconvolution of peaks of $\text{Er}^{3+}$ emission spectrum in three different host materials, at room temperature: (a) alumina-silica, (b) zinc-tellurite, and (c) tungsten-tellurite..	97
4.27 Erbium emission spectra of Er-Te glass, near 550 nm, for different temperatures.....	99
4.28 Absorption spectra of $\text{Er}^{3+}$ doped $\text{Al}_2\text{O}_3\text{-SiO}_2$ fibers of different lengths.....	100
4.29 Ground state absorption spectra of $\text{Er}^{3+}$ -doped zinc-tellurite and alumina-silica fibers.....	101
4.30 Local field correction factors for electric dipole transitions: spontaneous emission probability (solid line) and emission cross section (dashed line).....	103
4.31 The radiative lifetime measurements in alumina-silica & zinc-tellurite fiber....	105
4.32 Comparison of erbium absorption in $\text{Al}_2\text{O}_3\text{-SiO}_2$ , $\text{ZnO-TeO}_2$ & $\text{WO}_3\text{-TeO}_2$ hosts	106
5.1 Raman spectra of $x\text{Na}_2\text{O} \cdot (1-x-y)\text{ZnO} \cdot y\text{TeO}_2$ glasses.....	114
5.2 Chain-like $\text{Te}_3\text{O}_8^{4-}$ units, present in $\text{ZrTe}_3\text{O}_8$ crystals.....	121
5.3 Emission spectra of $\text{Er}^{3+}$ emission in $\text{TeO}_2$ fiber at different temperatures.....	128
5.4 Schematic figure of electron-phonon resonant coupling process.....	130
5.5 Raman spectra of zinc- and tungsten-tellurite glass. Inset shows Raman spectra of silica glass [Champagnon <i>et al.</i> ], for comparison.....	130

## Abstract

Tellurite glasses offer promising choices for photonics applications primarily due to their excellent optical, but also because of their good chemical and physical properties. In this thesis, we explain the strong and broad erbium emission in tellurite glasses and fibers. We study the glass network and electron-phonon characteristics of these glasses in order to understand the fundamental origin of their optical properties. In addition, we compare the absorption and emission properties of  $\text{Er}^{3+}$ -doped tellurite and alumina-silica glasses and fibers. We show that the strength of emission properties of erbium and effects of emission in fibers are strong due to a high refractive index of tellurite glass, which increases the local field correction at an activator site and leads to larger radiative transition probabilities. It is due to this reason that rare earth ions in tellurite glasses typically have larger stimulated emission cross-sections over a large bandwidth compared to other binary oxide glasses. Tellurite glasses also have phonons up to  $930\text{ cm}^{-1}$  (for  $\text{WO}_3\text{-TeO}_2$ ), which is of great importance for non-radiative transitions from upper energy levels. At the same time, these glasses have a strong Raman scattering intensity at low phonon frequencies ( $100 - 400\text{ cm}^{-1}$ ). Since this frequency range corresponds to the extent of the Stark splitting of the ground state of  $\text{Er}^{3+}$  ions, Raman scattering allows efficient resonant electron-phonon processes. We show that these processes are the main reason for broader emission in glasses with strong phonon frequency in the  $100 - 400\text{ cm}^{-1}$  range, particularly in  $\text{WO}_3\text{-TeO}_2$ .

# **Chapter 1**

## **Introduction**

Information technology has been going through a worldwide revolution. The combination of semiconductor lasers and low-loss optical fibers forever changed the way information is handled. Optical fiber communication developed very fast and has had a dramatic impact on the ability to transmit information. One of the reasons for such impact is the fact that this field combined expertise from many other sectors of optoelectronic science and technology, such as optical physics, materials science, condensed matter physics, optical computing, optical sensing, etc.

In particular, Rare-earth emission in glasses and fibers has had a very important effect on the development of optical communication systems. Providing an effective way to amplify signals has allowed optical communications over ever longer distances, replacing electrically regenerative repeaters that required costly high-speed electronics with fiber amplifiers, where no such electronics is needed. One of the developments in the field that has received special attention is erbium doped fiber amplifiers (EDFA), even though the amplifiers mechanism is quite simple: it uses stimulated emission of optically excited rare-earth ions in the fiber core. The operating principle of fiber amplifiers is the same as of that of lasers, except that amplifiers do not need a cavity whereas lasers need one for oscillation.

There are two aspects to this: the emission properties of erbium in glass and distributed effects of such emission in fibers. Our goal was to study the emission in both, glasses and fibers, for a complete understanding of its nature. We hoped that once we



understood erbium emission in different host materials, we would be able to predict the materials with the strongest effects.

EDFA have been mostly made from silica glasses, mainly because the fiber fabrication process is well known and relatively easier than that of other glasses. We chose tellurite glasses as a starting point in this study, hoping that their somewhat inferior physical properties would be offset by much better than silica rare-earth emission properties. Preliminary results on signal gain and erbium emission spectra in fibers that we made with Dr. Ahmet R. Kortan from OFS Laboratories were very good. The net small signal gain was about 30 dB for as short as 1 m long fiber. Using 980 nm pump, a spectrally ~180 nm (at 30 dB from max) broad erbium amplified spontaneous emission (ASE) is observed around 1.5 micron. Tellurite glass fibers of different lengths were tested and all found to lase in the 1530-1610 nm range. These results proved that erbium doped tellurite fibers offer strong potential for optical applications. Unfortunately, the fabrication of such fibers is extremely difficult and, at this point of development, there are still not many centers capable of fabricating of such fibers.

The work presented here is the result of a careful study, covering both the basic phenomena of rare-earth emission and the practical aspects of using them in amplifiers. This is a thorough analysis of observed emission effects in different host materials, with important pointers on the origin of such effects. Hereby, we show how the vibrational characteristics of the host material affect emission properties.

Over the years, numerous oxide glasses have been tested for different applications in photonics. Among them, tellurite glasses have appeared promising choices primarily due to their excellent optical, but also because of their good chemical and physical

properties. They possess high refractive index (larger than 2.0) [Mazurin *et al.*<sup>1</sup>], wide band infrared transmittance (extending up to 6  $\mu\text{m}$ ) [Kim *et al.*<sup>2</sup>, Wang *et al.*<sup>3</sup>], and large third order non-linear optical susceptibility [Kim *et al.*<sup>2</sup>, Wang *et al.*<sup>3</sup>, El-Mallawany<sup>4</sup>]. In addition, tellurite glasses combine the attributes of a short wavelength UV edge (about 350 nm), good glass stability, rare earth ion solubility, a slow corrosion rate, and relatively low phonon energy among oxide glass formers [El-Mallawany<sup>4</sup>, Jacobs & Weber<sup>5</sup>, Weber *et al.*<sup>6</sup>, Heo *et al.*<sup>7</sup>].  $\text{Er}^{3+}$ -doped tellurite glasses have been attractive for upconversion emission, especially due to their low phonon energy [Tanabe *et al.*<sup>8</sup>, Nii *et al.*<sup>9</sup>]. The higher refractive index of tellurite glass increases the local field correction at an activator site and leads to larger radiative transition probabilities [Jacobs & Weber<sup>5</sup>]. Thus, rare earth ions in tellurite glasses typically have larger stimulated emission cross-sections over a broad bandwidth compared to other binary oxide glasses [El-Mallawany<sup>4</sup>, Weber *et al.*<sup>6</sup>].

They are also very important for multiphonon non-radiative transitions due to their maximal phonon energy of about 930  $\text{cm}^{-1}$  [Nii *et al.*<sup>9</sup>, Sekiya *et al.*<sup>10,13</sup>, Himei *et al.*<sup>11,12</sup>]. Doped with rare-earth atoms, tellurite glasses have been used for many fiber laser and amplifier applications [Desurvire<sup>14</sup>, Sudo<sup>15</sup>, Becker *et al.*<sup>16</sup>]. The emission spectrum from erbium in tellurite glasses is almost twice as broad as the corresponding spectrum in silica [Desurvire<sup>14</sup>, Sudo<sup>15</sup>, Becker *et al.*<sup>16</sup>, Marjanovic *et al.*<sup>17</sup>].  $\text{Er}^{3+}$  emission spectra show a higher and flatter signal gain over shorter lengths in tellurite fibers [Marjanovic *et al.*<sup>17-19</sup>]. This demonstration has attracted attention since a flat and large bandwidth gain of erbium doped fiber amplifiers is key in increasing the transmission capacity in wavelength-division-multiplexing systems.

Several reasons were believed to be the cause for emission properties: the structure of the host materials, site-to-site difference of the rare earth environment in such a host, the transition probability dependence on host material, etc. The purpose of this study is, therefore, to determine the glass network and electron-phonon characteristics of tellurite glasses, which will ultimately help understand the fundamental origin of their optical properties. We will show that tellurite glasses are a good host material for erbium ions due to: a) their maximal phonon frequency in the range of  $780\text{ cm}^{-1}$  (in pure and zinc-tellurite glass) to  $930\text{ cm}^{-1}$  (for tungsten-tellurite), which is of great importance for non-radiative transitions from upper energy levels, and b) tellurite glasses exhibit a strong Raman scattering intensity at low phonon frequencies. This is very important because that frequency range corresponds to the Stark splitting of the ground state of  $\text{Er}^{3+}$  ions, which allows resonant electron-phonon coupling processes.

A structural study of bulk glass is important to determine the vibrational properties of the rare earth environment. Several research groups have investigated the network, electronic structure and phonon characteristics of tellurite glasses by using different experimental methods. For example, binary tellurite glasses containing alkali oxides have been studied by infrared [Nii *et al.*<sup>9</sup>, Sekiya *et al.*<sup>10,13</sup>, Himei *et al.*<sup>11-12</sup>], Raman [Himei *et al.*<sup>11-12</sup>, Sekiya *et al.*<sup>13</sup>, Marjanovic *et al.*<sup>17</sup>, Suzuki<sup>20</sup>, Moawad *et al.*<sup>21</sup>], and X-ray photoelectron spectroscopies [Nii *et al.*<sup>9</sup>, Marjanovic *et al.*<sup>17</sup>, Moawad *et al.*<sup>21</sup>, Lim *et al.*<sup>22</sup>]. Here, we conduct a two-prong investigation of new tellurite glasses: a Raman study that provides detailed information on the microscopic structure of these glasses, and a study of the erbium emission in fibers fabricated from these glasses. In

particular, we report on the emission from fibers of different lengths and for different pumping schemes.

Although individual elements introduced in glasses can act as network formers or modifiers, the combination of several of these elements, e.g. alkali and transition metals, can modulate or even alter the effect of the individual elements. Our Raman results demonstrate this principle. Specifically, we compare the Raman spectra of alkali-zinc and alkali-tungsten tellurite glasses and extract a few guiding principles on how to construct a tellurite glass with the desired microstructure, molecular units and network topology. In our particular case, these glasses are of interest for their optical properties, especially erbium emission.

To check the emission site-to-site difference, one needs to measure a narrow linewidth, with a pump source that only excites a small subset of the ions in the sample, those that are resonant with the excitation frequency (fluorescence line narrowing). Such measurements need to be done at low temperature; otherwise, the homogeneous broadening of the line will be large enough that essentially all ions will be excited. As the excitation source is swept in frequency, the spectra then show the fluorescence spectra corresponding to the different sites that the ions can occupy.

Hereby, we have carried out a study of tellurite glasses using high-resolution combined excitation-emission spectroscopy (CEES) to investigate Er emission at low temperatures [Marjanovic *et al.*<sup>17</sup>]. Different lasing lines observed by measurements in fibers are seen to correspond to the erbium transitions identified in the CEES study. We show that specific lasing lines can be selected by adjusting the length of the fiber [Marjanovic *et al.*<sup>17-23</sup>]. As the length of the fiber is increased, lower energy transitions

contribute to the lasing. Emission spectra from both techniques show erbium transitions obeying electric dipole transition selection rules calculated for these glasses.

We compare the absorption and emission properties of double-clad  $\text{Er}^{3+}$ -doped tellurite and ultra highly doped alumina-silica single mode fibers. Absorption and lifetime measurements were carried out in fibers of different lengths, from a few centimeters to 2.5m. Short samples were measured in order to avoid re-absorption and re-emission processes, and long ones for the opposite reason – to investigate the energy transfer to lower energy transitions. For a quantitative description of absorption and emission processes, we use the well-established Judd-Ofelt theory.

In Chapter 2, we present the background of the rare-earth emission in glasses used for photonics. Chapter 3 is devoted to experimental techniques used in this study of  $\text{TeO}_2$  glasses and their fibers. This chapter also gives a full description on the materials used, with explanation on sample preparation. Chapter 4 contains the absorption-emission results on erbium-doped tellurite glasses and fibers. These results are compared with emission in alumina-silica fibers. A discussion of these results is presented in Chapter 5, and the conclusion with guidelines for future research is given in Chapter 6.

## Bibliography

- [1] O. Mazurin, M. Stretsina, T. Shvaiko-Shvaikovskaya (Eds.), *Handbook of Glass data: Single component and Binary Non-Silicate Oxide Glasses*, Physical Science Data **15**, Part B (Elsevier, Amsterdam, 1985).
- [2] S.H. Kim, T. Yoko, S. Sakka, *J. Am. Ceram. Soc.* **76** (1993) 2486.
- [3] J.S. Wang, E.M. Vogel, E. Snitzer, *Opt. Mat.* **3** (1996) 187.
- [4] R.A.H. El-Mallawany, *Tellurite Glasses Handbook* (CRC Press, Boca Raton, 2001).
- [5] R.R. Jacobs, M.J. Weber, *IEEE J. Quantum Electron* **12** (1976) 102.
- [6] M.J. Weber, J.D. Myers, D.H. Blackburn, *J. Appl. Phys.* **52** (1981) 2944.
- [7] J. Heo, D. Lam, G.H. Sigel, Jr., E.A. Mendoza, D. A. Hensley, *J. Am. Ceram. Soc.* **75** (1992) 277.
- [8] S. Tanabe, K. Hirao, N. Soga, *J. Non-Cryst. Solids* **122** (1990) 79.
- [9] H. Nii, K. Ozaki, M. Herren, M. Morita, *J. Lumin.* **76/77** (1998) 116.
- [10] T. Sekiya, N. Mochida, A. Ohtsuka, M. Tonokawa, *J. Non-Cryst. Solids* **144** (1992) 128.
- [11] Y. Himei, A. Osaka, T. Nanba, Y. Miura, *J. Non-Cryst. Solids* **177** (1994) 164.
- [12] Y. Himei, Y. Miura, T. Nanba, A. Osaka, *J. Non-Cryst. Solids* **211** (1997) 64.
- [13] T. Sekiya, N. Mochida, S. Ogawa, *J. Non-Cryst. Solids* **176** (1994) 105.
- [14] E. Desurvire, *Erbium Doped Fiber Amplifiers* (John Wiley & Sons, Inc., New York, 1994).
- [15] S. Sudo, (Ed.), *Optical Fiber Amplifiers* (Artech House, Inc., Boston, 1997).

- [16] P.C. Becker, N.A. Olsson, J.R. Simpson, *Erbium-Doped Fiber Amplifiers: Fundamentals and Technology* (Academic Press, San Diego, 1999).
- [17] S. Marjanovic, J. Toulouse, H. Jain, C. Sandmann, V. Dierolf, A. R. Kortan, N. Kopylov, R.G. Ahrens, *J. Non-Cryst. Solids* **322** (2003) 311.
- [18] S. Marjanovic, J. Toulouse, C. Sandmann, Z. Fleischman, V. Dierolf, M.F. Yan, V.S. Johnson, P.W. Wisk, A.R. Kortan, N. Kopylov, R.G. Ahrens, *Optical Fiber Communication Conference on CD-ROM* (The Optical Society of America, Washington, D.C., 2004), ThA5.
- [19] S. Marjanovic, J. Toulouse, C. Sandmann, Z. Fleischman, V. Dierolf, M.F. Yan, V.S. Johnson, P.W. Wisk, A.R. Kortan, N. Kopylov, R.G. Ahrens, *CLEO/IQEC Conference on CD-ROM* (The Optical Society of America, Washington, D.C., 2004), CTuU6.
- [20] K. Suzuki, *J. Non-Cryst. Solids* **95-96** (1978) 15.
- [21] H.M. Moawad, J. Toulouse, H. Jain, O. Latinovic, A.R. Kortan, *Proceedings of the Optoelectronic and Technology in the Information Age symposium at the 103rd Annual Meeting*, (The American Ceramic Society, Westerville, OH, 2001), p. 45.
- [22] J.W. Lim, H. Jain, J. Toulouse, S. Marjanovic, J.S. Sanghera, R. Miklos, I.D. Aggarwal, *Proceedings of the 16<sup>th</sup> University Conference on Glass Science* (RPI, Troy, NY, 2003).
- [23] S. Marjanovic, J. Toulouse, A. R. Kortan and N. Kopylov, *OSA Trends in Optics and Photonics (TOPS)*, Vol. **73**, Conference on Lasers and Electro-Optics, OSA Technical Digest, Post Conference Edition (The Optical Society of America, Washington, D.C., 2002), p. 18.

## **Chapter 2**

### **Background**

We shall begin this study by a brief description of glasses as host materials for photonics applications. In addition, we shall describe rare-earth ions and their emission properties, especially in glass-host materials. Main glass formers and modifiers could be used for oxide, fluoride and chalcogenide glass systems. Here, we restrict ourselves to tellurite-oxide glasses and their comparison to silica-oxide glass.

#### **2.1 Rare earth elements in oxide glasses**

In general, glass is a supercooled liquid that bypasses below the melting temperature. The viscosity of glasses increases to such a high value that they become solid with a disordered arrangement of atoms. Thus, they exhibit a short-range order and form a three-dimensional matrix, but lack the uniformity, symmetry and structure of crystalline materials and have no long-range periodicity.

Some oxides, called glass formers, such as  $\text{SiO}_2$ ,  $\text{GeO}_2$ ,  $\text{BaO}_3$ ,  $\text{TeO}_2$ ,  $\text{P}_2\text{O}_5$ , etc., have the ability to form glasses by themselves or by mixing with other network formers. They are all capable of forming a three-dimensional network with oxygen, thus providing very strong covalent bonds, which give these glasses their characteristic properties. On the other hand, some oxides, which are commonly called network modifiers, cannot form a glass by themselves but can form a glass as a mixture with network formers in certain



compositional range. Oxides of alkali metals and alkali-earth metals such as  $\text{Li}_2\text{O}$ ,  $\text{Na}_2\text{O}$ ,  $\text{K}_2\text{O}$ ,  $\text{CaO}$ ,  $\text{SrO}$ , etc. are typical network modifiers. The introduction of modifiers in the glass disrupts the glass network, opens up the network structure, lowering the density of the glass, weakening the bond strength and lowering the viscosity of the glass. In addition, oxides such as  $\text{ZnO}$ ,  $\text{MgO}$ ,  $\text{Al}_2\text{O}_3$ ,  $\text{PbO}$ , etc., have characteristics that fall between those of network formers and network modifiers [Sudo<sup>1</sup>].

The rare-earth elements are a series of 15 transition metals, with very similar electronic configurations based on the gradual filling of the  $4f$  subshell along the series. All these elements have the electronic configuration of  $1s^2, 2s^2, 2p^6, 3s^2, 3p^6, 3d^{10}, 4s^2, 4p^6, 4d^{10}, 4f^x, 5s^2, 5p^6, 6s^2$ . All orbits consist of closed shells except for the  $4f^x$  level,  $x = 1, 2, \dots, 14$ . The preferential trivalent ( $3+$ ) ionization removes the electrons of  $6s^2$  and  $4f^1$ , and the electronic configuration of these ions becomes equivalent to that of xenon plus a certain number (1-13) of  $4f$  electrons. Therefore, the electronic state of these rare-earth ions is determined by the electronic configuration of the  $4f^x$  level, and their observed IR and visible optical spectra are a consequence of transitions between  $4f$  states (we will show later that these transitions actually occur between  $4f$  and admixed  $5d$  orbitals due to selection rules). However, since the electrons of  $5s^2$  and  $5p^6$  shield  $4f^x$  electrons, the effect of the environment on  $4f^x$  electron is reduced to perturbation of the free ion orbitals [Sudo<sup>1</sup>].

Thus, the electronic energy levels of the rare-earth ions are determined by the electronic configuration of the  $4f^x$  level and the effect of the environment on the  $4f^x$  electrons, although such effects are moderate. Schrödinger equations for many-electron atoms are extremely complicated because all the electrons interact with one another in

various ways. In such many-electron atoms, two types of interactions are mainly considered: coulombic interaction between electrons with spin correlation (electrostatic), and spin-orbit coupling (magnetic). Therefore, the Hamiltonian of the many-electron system can be described as

$$H = H_c + H_{el-el} + H_{so} , \quad (2.1)$$

where  $H_c$  is the Hamiltonian for the central field,  $H_{el-el}$  is the Hamiltonian for the electrostatic interaction between electrons, and  $H_{so}$  is the Hamiltonian for the spin-orbit coupling. Particularly, the  $4f$  electron of rare-earth ions in condensed matter experiencing interactions and effects from the structural environment in addition to those with other  $4f$  electrons. The interactions with the environment can be treated as a perturbation of the Hamiltonian of the isolated erbium atom or ion. Therefore, the Hamiltonian can be written for an individual rare-earth ion and decomposed as

$$H = H_c + H_{el-el} + H_{so} + V_{ion-static-lattice} + \\ + V_{ion-dynamic-lattice} + V_{electromagnetic} + V_{ion-ion} . \quad (2.2)$$

Here, the first three terms describe the free ion (in complete isolation) and the others, the interactions of the ions with the host (static and dynamic), electromagnetic field and among themselves. Taking these interactions in account, one can describe the energy levels of rare-earth ions, as shown in FIG 2.1 [Sudo<sup>1</sup>].

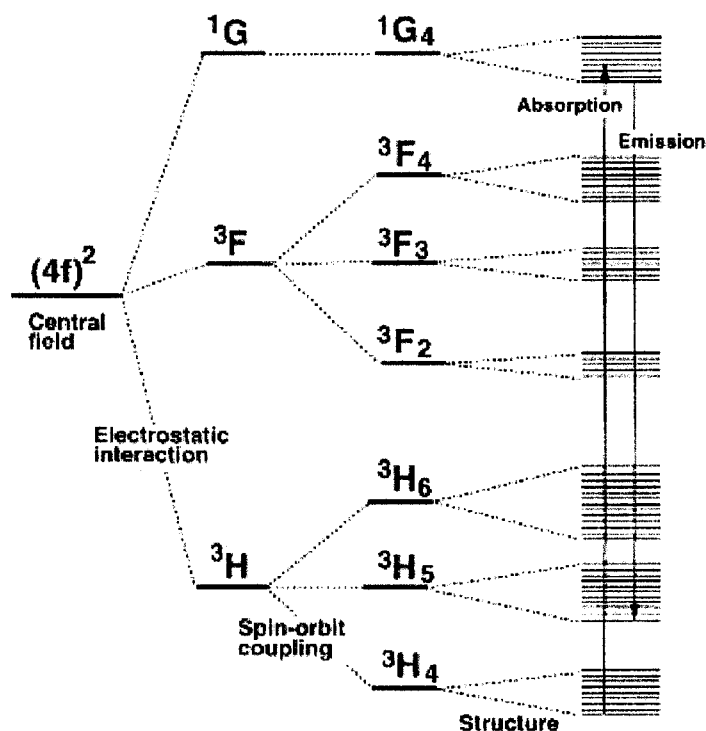


FIG. 2.1 A portion of the energy levels for  $\text{Pr}^{3+}$  ions with 4f-electrons [Sudo<sup>1</sup>].

As an example, FIG. 2.1 shows a portion of the energy levels for praseodymium ions with two 4f-electrons, in the central field approximation. The valence electrons in the central field interact electrostatically (coulombic interaction between electron and spin correlation). As a result, their central field energy level splits into seven sublevels with different energies such as  $1S$ ,  $3P$ ,  $1D$ ,  $3F$ ,  $1G$ ,  $3H$ , and  $1I$  [Herzberg<sup>2</sup>]. This does not reflect the actual order of these energy levels, which have to be reordered based on Hund's law. Then, due to the spin-orbit coupling, the energy levels of  $3H$  and  $3F$  that have parallel spin ( $\uparrow\uparrow$ ,  $S = 1$ , triplet) split into three levels, whereas the energy level of  $1G$  does not split because of the paired spins ( $\uparrow\downarrow$ ,  $S = 0$ , singlet). Shown on the same figure is the split of the energy levels due to Zeeman and Stark effects, depending on whether the ions find themselves in a magnetic or electric field.

In glass materials, the electrostatic interaction between the ions and the lattice is dominant, so the energy levels are split because of the Stark effect. The number of split levels caused by the Stark effect is  $2J+1$ , where  $J$  is the total angular momentum. In addition, the magnitude of the energy splitting depends on the magnitude of the local electric fields, which vary depending on the location of the ions. This variation in Stark splitting energy provides the basis for the spectral band in the absorption and fluorescence characteristics of rare-earth ions. Consequently, different materials possess different spectral characteristics of absorption and fluorescence of rare-earth ions because of their different Stark splitting energy levels.

FIG. 2.2 shows the energy levels of  $\text{Er}^{3+}$  due to the coulombic interaction between electrons, including spin correlations and spin-orbit coupling, and the Stark effect due to the crystal field and local coordination symmetry. The magnitude of the full Stark splitting is several hundred  $\text{cm}^{-1}$  for  $\text{Er}^{3+}$ -doped glasses, as can be seen in the literature (for example, see [Desurvire & Simpson<sup>3</sup>]). However, the magnitude of the full Stark splitting can differ slightly for Er ions in different sites. Therefore, particular transitions can give rise to broadened lines. This broadening is inhomogeneous in nature. In addition, the individual Stark levels can fluctuate and broaden because of the fluctuation of the crystal fields caused by atomic motions (phonons): this is then called lifetime broadening or homogeneous broadening. The respective magnitudes of inhomogeneous and homogeneous broadening range from 27 to 60  $\text{cm}^{-1}$  and 8 to 49  $\text{cm}^{-1}$ , respectively (see page 80 in [Sudo<sup>1</sup>] for complete listing of the literature). The energy spacing  $\Delta E$  between adjacent Stark sublevels ranges from 20 to 80  $\text{cm}^{-1}$  and its average value is 50  $\text{cm}^{-1}$ . In a state of thermal equilibrium, the energy population of  $\text{Er}^{3+}$  ions has a

Boltzmann distribution. Since the ratio between two adjacent Stark sublevel populations is  $\exp(-\Delta E/kT) = 0.78$  (with  $\Delta E$ , at room temperature), there can be large difference in the population of those sublevels. In FIG 2.2, the gray scale of the Stark sublevels indicates such population difference in the sublevels; that is, the sublevels with lower energy have a higher population of ions [Sudo<sup>1</sup>]. Positions of the Stark levels of the  $\text{Er}^{3+}$   $^4\text{I}_{13/2}$  and  $^4\text{I}_{15/2}$  multiplets in Al-Ge silica can also be found in the literature [Backer *et al.*<sup>4</sup>].

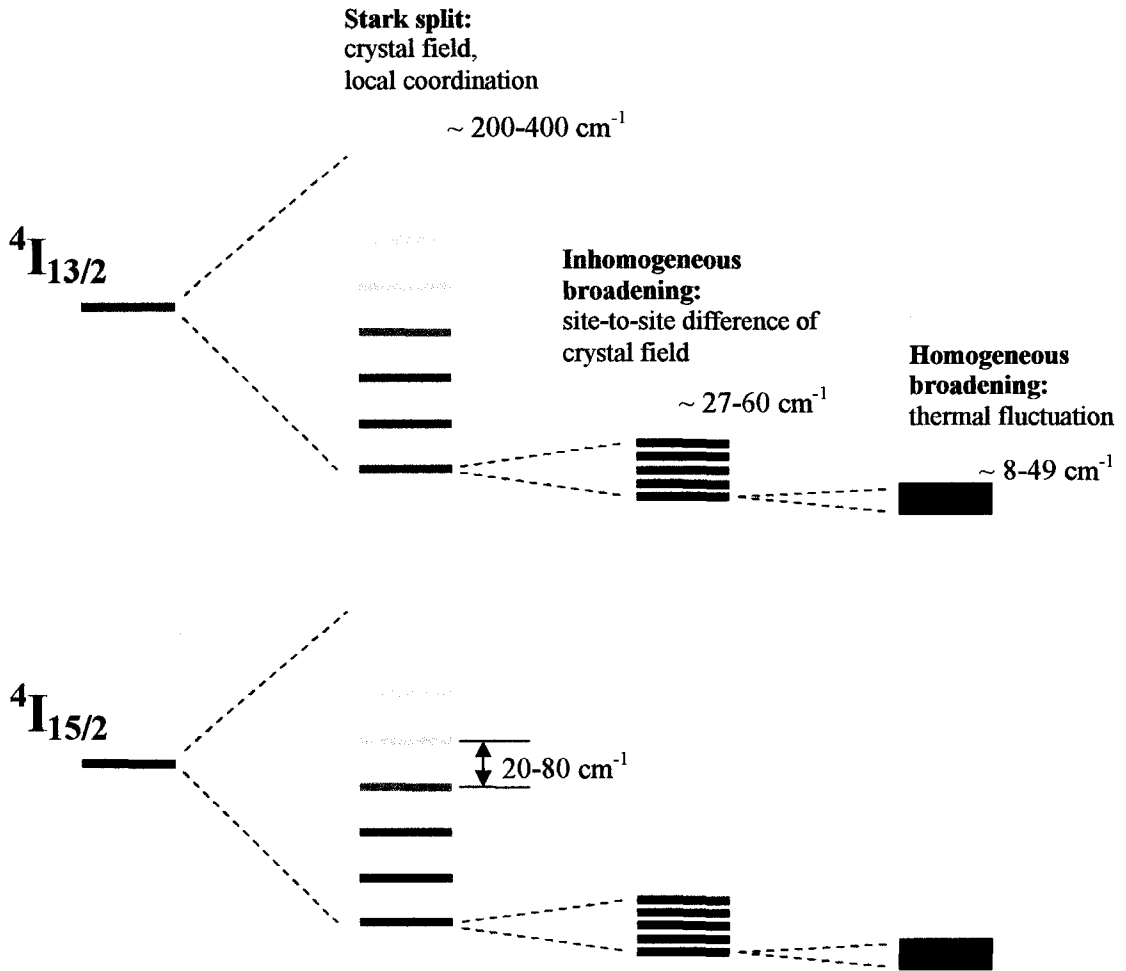


FIG. 2.2  $\text{Er}^{3+}$  energy levels split due to the Stark effect, inhomogeneous and homogeneous broadening.

Our main interest in this study is the erbium emission and its use for efficient signal amplification. Several requirements should be met for such amplification. The first is that rare earth ions should decay radiatively with high quantum efficiency. This indicates no quenching effect of ions, a low nonradiative transition caused by multiphonon relaxation, and a high optical intensity in the core part. The high optical intensity in the core increases the stimulated emission rate because the stimulated emission rate is proportional to the intensity of the electromagnetic field, whereas the spontaneous emission rate is independent of it [Yariv<sup>5</sup>]. The second requirement is that of efficient pumping, which means a high-level pumping power and effective absorption of the pump light by rare earths. The third one is that the fiber host should exhibit low loss, including low scattering loss and low absorption loss, even for fibers with high refractive index and high levels of rare earth doping.

The energy level diagram of erbium ions for 1.5  $\mu\text{m}$  amplification is shown in FIG 2.3. Erbium ions are pumped at 980 nm or 1480 nm. The signal is amplified by the transition from  $^4\text{I}_{13/2}$  to  $^4\text{I}_{15/2}$ . This is a three-level (or, quasi four-level) system with high quantum efficiency. An efficient relaxation process occurs when  $\text{Er}^{3+}$  ion goes from  $^4\text{I}_{11/2}$  to  $^4\text{I}_{13/2}$  level. However, two major degradation processes can affect amplification: the excited-state absorption (ESA) with 980 nm pumping [Quimby *et al.*<sup>6-8</sup>], and cooperative upconversion with 1.48- $\mu\text{m}$  pumping [Quimby *et al.*<sup>6</sup>, Ainslie *et al.*<sup>10</sup>]. A 980-pump ESA appears during high-power operation and cooperative upconversion appears when the erbium ion concentration is high.

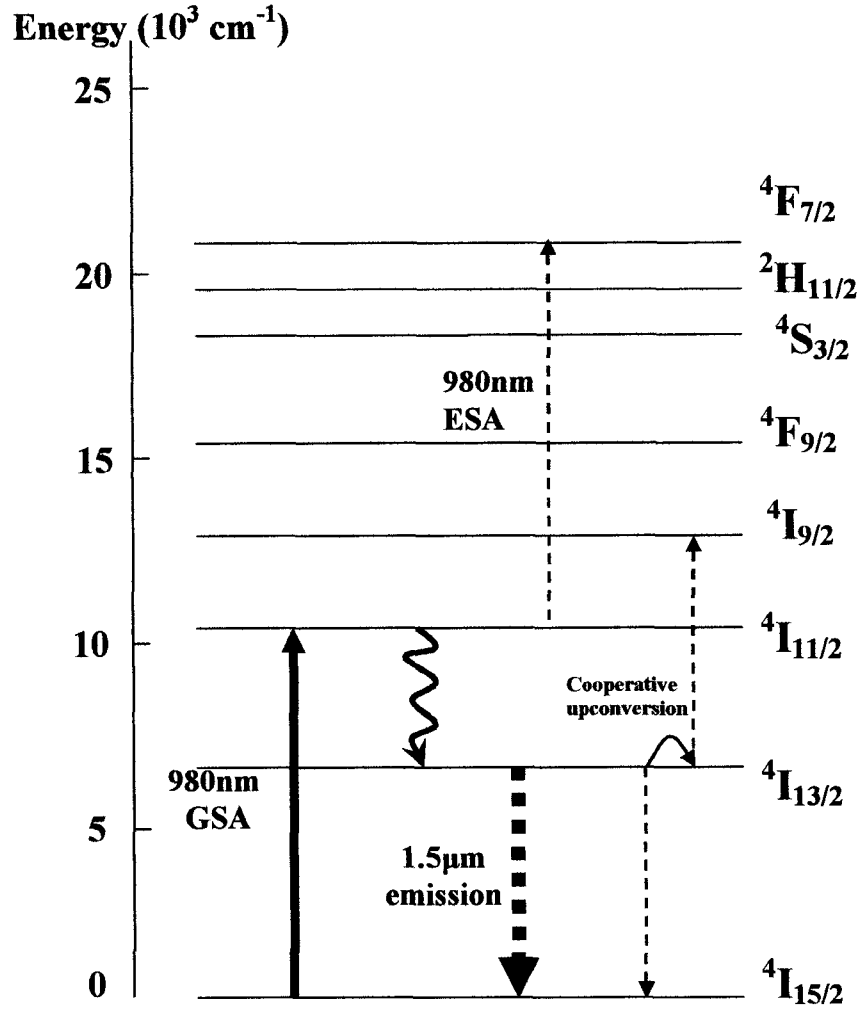


FIG. 2.3 Energy level diagram of  $\text{Er}^{3+}$  ion [Sudo<sup>1</sup>].

It is also important to point out that the excited electronic states of rare earth ions in solids can decay nonradiatively by exciting lattice vibrations. When the energy gap between the excited state and the next-lower state is larger than the maximum phonon energy in the material, emission of several phonons is required to conserve energy. The decay rates are determined predominantly by the number of phonons required to bridge the energy gap. Since the highest-energy phonons can conserve energy in the lowest-order process, they contribute most to the relaxation. Because of the different vibrational

spectra of different glasses, the rate of multiphonon processes is host dependent. The dependence on specific-rare-earth or electronic states involved is negligible unless there are strong selection rules.

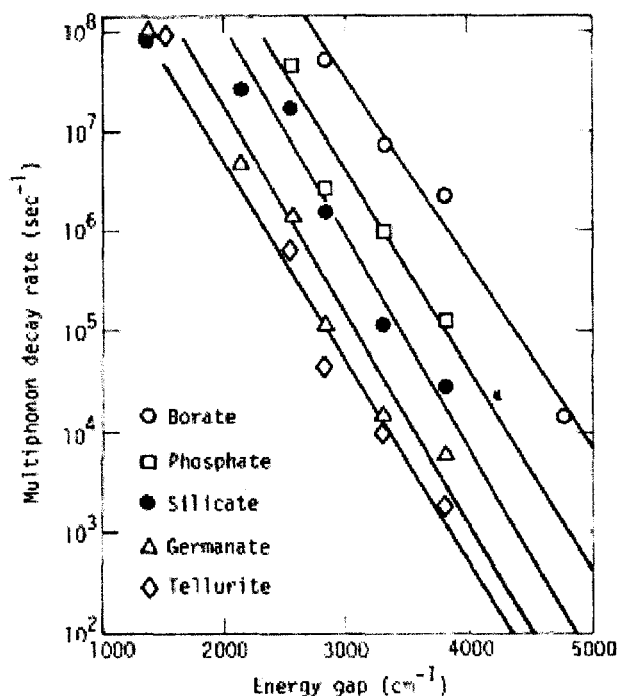


FIG. 2.4 Multiphonon decay rates for rare-earth ions in five oxide glasses plotted as a function of the energy gap to the next-lower level [Layne *et al.* <sup>11</sup>].

In FIG. 2.4, the nonradiative decay rates measured in each of five oxide glasses (borate, phosphate, silicate, germanate and tellurite) are plotted on a semilogarithmic scale versus energy gap [Layne *et al.* <sup>11</sup>]. The approximate frequencies of the high-energy phonons in each glass are: borate – 1350 cm<sup>-1</sup>; phosphate – 1100 cm<sup>-1</sup>; silicate – 1000 cm<sup>-1</sup>; germanate – 900 cm<sup>-1</sup>; and – 800 cm<sup>-1</sup>. The rates for each glass follow the simple exponential dependence on energy gap. Authors found a strong dependence of the rates on the host composition. The fastest decays occur in borate glass, followed in order



by phosphate, silicate, germanate, and tellurite. For each level, the decay rate in tellurite glass is approximately  $10^{-3}$  times the corresponding rate in borate glass; still the rates in tellurite are ten times greater than the fastest rates measured in crystal host materials.

Multiphonon processes of rare earths in glasses arise from the same general physical processes as in crystals. The rare earth has oxygen or other anions as nearest neighbors. The vibrations of these and more distant ions contribute to the fluctuating Stark field that induces nonradiative transitions, as in the case of crystals. There are, however, several differences in decay properties between glasses and crystals.

First, the spectrum and nature of vibrations in amorphous materials are different and their understanding is still incomplete. For multiphonon relaxation, one is interested in the highest frequency phonons. In glasses, these are the stretching vibrations of the glass network former polyhedron, a “molecular” vibration that is localized and weakly coupled to the network as a whole. In addition to these vibrations, there is a spectrum of lower-frequency modes, which will turn to be of great importance in this study, which will be explained in details in Chapter 5.

A second difference is the energies of the highest-frequency vibrations in glasses. For oxide glasses, these range from 700 to 1400 wavenumbers and are much higher than the highest optical-mode frequencies in most oxide and halide crystals commonly used as rare-earth hosts. Therefore, for a given rare-earth excited state and for comparable ion-phonon coupling strengths, a lower order multiphonon process in such glasses will be capable of bridging the energy gap. The resulting relaxation is faster. However, this is not of great significance in this thesis since we focus on 1.5-micron emission achieved with 980 or 1480 nm pumping.

Finally, additional advantage of glasses over crystals as hosts for photonics is that rare earths in glass can occupy nonequivalent sites which results in different crystal-field symmetries and strengths. Depending upon the type of network modifier ions present, there are site-to-site variations in the Stark splitting as evidenced in the inhomogeneously broadened optical absorption and emission lines, and the radiative transition probability, as evidenced in the nonexponential fluorescence decays.

## 2.2 Quantum mechanics description of dipole transitions and Judd-Ofelt theory

Interest in the intensities of rare-earth  $f \leftrightarrow f$  spectra can be said to have begun with a paper published in 1937 by Van Vleck [Van Vleck<sup>12</sup>]. At that time, it had not been established whether the sharp lines in the spectra of trivalent lanthanide ions were in fact due to transitions within the  $4f^N$  configuration or due to transitions between that configuration and one of higher energy, such as  $4f^{N-1}5d$ . Electric dipole, magnetic dipole and electric quadrupole mechanisms were all considered to account for the observed intensities. Later [Boer *et al.*<sup>13</sup>], it was calculated that electric quadrupole transitions would have much less intensity than is observed, and that magnetic dipole transitions would usually be observed only if electric dipole induced transitions were absent.

A mere knowledge of the position of energy levels is clearly not sufficient to determine the transition probabilities associated with each pair of levels. Using quantum theory, such transition probabilities between quantum states  $|\psi_a\rangle$  can actually be calculated. Both types, the electric dipole (ED) transitions and magnetic dipole (MD) transitions should be considered. The Radiative emission probabilities corresponding to

either type of transitions can then be calculated using perturbation theory through the matrix element of the corresponding interaction Hamiltonian operator, taken between the initial and final states.

For optical transitions between levels of a particular  $4f^N$  configuration, the electric dipole radiation is forbidden in first order, because the electric dipole operator has uneven parity and the transition matrix element must have even parity, by Laporte selection rule. For a free ion, transitions that involve a redistribution of electrons in a single quantum shell are forbidden. Although, if the environment about the ion lacks a center of symmetry (as in tetrahedral coordination, for example), mixing of the  $3d$  and  $4p$  (or  $5d$  and  $4f$ , for rare earths) orbitals may occur and Laporte transitions may occur. In addition, vibronic (vibrational and electronic) coupling between wavefunctions with opposite parities may occur. Thus, the crystal-field Hamiltonian can contain odd-parity terms in cases where the site symmetry is not a center of inversion. These terms introduce into the  $4f$  wavefunctions small admixtures of opposite parity states from higher energy configurations, like  $4f^{N-1}5d$ . The intensity of a particular transition is determined by the amount of opposite-parity configuration that has been mixed into the initial and final states. Crystal vibrations of odd symmetry can also admix odd-parity  $4f^{N-1}n1$  configurations into the  $4f^N$  manifold. For a centrosymmetric crystal, this is the only source of, so called, forbidden ED transitions. MD transitions are allowed since no change in parity is involved in this process. However, their intensities are in the order of magnitude to those of the so-called forbidden ED transitions, for non-centrosymmetric crystals. Also, there are fewer MD transitions allowed since they must satisfy the selection rules:  $\Delta J = 0, \pm 1$ ,  $\Delta L = 0$ ,  $\Delta S = 0$ , and  $J = 0 \rightarrow J = 0$  transitions are forbidden.

Including the admixture from higher energy configuration, the wavefunction for a particular ion can be written using first-order perturbation theory:

$$|\psi_i\rangle = \sum_{S,L,J,J_z} \left[ |4f^N \alpha[SL]JJ_z\rangle + \sum_{\psi'} \frac{|\psi'\rangle \langle \psi' | V_{odd} | 4f^N \alpha SLJJ_z \rangle}{E(\psi') - E(4f^N \alpha SLJJ_z)} \right] \quad (2.3)$$

where  $V_{odd}$  represents the odd-parity part of the crystal field added to unperturbed  $4f^N \alpha SLJ$  part and  $|\psi'\rangle$  represents the possible intermediate states of the system. The matrix element of the electric dipole operator  $\vec{D}$  between the states  $|\psi_i\rangle$  and  $|\psi_f\rangle$  of the  $4f^N$  configuration will thus involve a sum over intermediate states of the form

$$\sum_{\psi'} \frac{\langle \psi_f | \vec{D} | \psi' \rangle \langle \psi' | V_{odd} | \psi_i \rangle}{E(\psi') - E(4f^N \alpha SLJJ_z)} \quad (2.4)$$

where the states  $|\psi_i\rangle$  and  $|\psi_f\rangle$  are written in zeroth order.

This problem as such is practically mathematically unsolvable: in the case of electric dipole transitions, such a direct theoretical calculation is subject to numerous and severe difficulties. Judd-Ofelt [Judd<sup>14</sup>, Ofelt<sup>15</sup>] theory made the ED problem finally tractable. It does not provide a full quantum mechanical solution over a complete set of eigenfunctions of the Schrodinger equation, but rather the angular solution. Their work is based on two assumptions. First, the spread in energy of the excited configuration is assumed small compared to the average difference in energy between that configuration and the ground  $4f^N$  configuration. This is not a good approximation for rare earth ions for which the  $4f^{N-1}5d$  configuration does not lie very much higher in energy than the  $4f^N$  ground configuration. Second, all crystal field states are assumed to be equally populated and the transitions between any two terms to have the same energy. Despite these

arbitrary assumptions, numerous authors have used this theory and have reported excellent agreement of calculated quantities with experimental measurements.

The Judd-Ofelt is powerful and important in that it can be used to obtain stimulated emission cross sections for laser transitions, to look for new laser transitions, and to assess parasitic transitions. This allows us to assess the suitability of new laser hosts and to understand the performance limitations imposed on active media [Sudo<sup>1</sup>]. The fundamental result of this theory is that the line strength  $S_{ed}$  of an electronic dipole transition taking place between states  $|\psi_i\rangle$  and  $|\psi_f\rangle$ , corresponding to  $^{2S+1}L_J$  and  $^{2S'+1}L'_{J'}$ , respectively, is given by the relation:

$$S_{J'J}^{ed} = \frac{1}{e^2} \left| \langle \psi_f | H_{ed} | \psi_i \rangle \right|^2 = \sum_{k=2,4,6} \Omega_k \left| \langle f^N \gamma [SL] J | U^{(k)} | f^N \gamma [S'L'] J' \rangle \right|^2. \quad (2.5)$$

In equation (2.5),  $H_{ed}$  is the ED Hamiltonian, and  $U^{(k)}$  are reduced tensor operator components with matrix elements that are constants virtually independent of the host [Desurvire<sup>16</sup>]. Their values are tabulated, and could be found for  $\text{Er}^{3+}$  in [Weber<sup>17</sup>, Chamberlain *et al.*<sup>18</sup>].  $S$ ,  $L$ , and  $J$  are the total spin, the total orbital momentum, and the total angular momentum respectively,  $\gamma$  is an additional index, designating Russell-Saunders (RS) manifolds for repeated RS terms of the  $4f^N$  electronic configuration with the same quantum numbers  $S$  and  $L$ .

The  $\Omega_k$  coefficients, the three Judd-Ofelt parameters  $\Omega_k$  ( $k = 2, 4, 6$ ) (by Judd-Ofelt theory, these are only non-zero parameters), have so far been assumed to arise solely from the crystal field: they can be regarded as phenomenological coefficients that reflect the crystalline host influence on the  $4f \rightarrow 4f$  radiative transition probabilities. However, they can also contain contributions from admixtures by lattice vibrations.

Unfortunately, this theory does not distinguish between crystal field and lattice vibrations contribution to dipole transitions. The Judd-Ofelt parameters values are empirically determined by comparing the theoretical line strength  $S_{ed}$  in Eq. (2.5) with the experimental result, through a least squares fitting algorithm. The experimental study of how glass composition affects the intensity parameters  $\Omega_k$  enables us to determine the relative contributions of coupling effects (both crystal field and vibrational) in each type of glass. Once these have been determined for a given rare-earth-host combination, they can be used to calculate electric dipole transition strengths (absorption and emission) between any two levels of the system.

The theoretical oscillator strength  $\bar{f}_{JJ'}^{ed}$  can be calculated using formula

$$\bar{f}_{JJ'}^{ed}(calc) = \frac{8\pi^2 m_e c}{3h(2J+1)\bar{\lambda}} \left[ \frac{(\bar{n}^2 + 2)^2}{9\bar{n}} \right] S_{JJ'}^{ed}, \quad (2.6)$$

where  $J = 15/2$  is the total angular momentum of the  $^4I_{15/2}$  ground state of the activator  $Er^{3+}$  ions,  $\bar{\lambda}$  and  $\bar{n} = \bar{n}(\bar{\lambda})$  are the mean wavelength of the  $^4I_{15/2} \rightarrow J'$  absorption band and the refractive index of the crystal at this wavelength  $\bar{\lambda}$ . In our work, the experimental oscillator strengths  $\bar{f}_{JJ'}^{ed(exp)}$  were obtained from absorption spectra of  $Er^{3+}$ -doped sodium-zinc-tellurite glass fibers using the formula:

$$\bar{f}_{JJ'}^{ed}(exp) = \frac{1}{N_O} \cdot \frac{m_e c}{\pi \omega^2} \cdot \left[ \frac{9\bar{n}}{(\bar{n}^2 + 2)^2} \right] \int k(\lambda) d\lambda, \quad (2.7)$$

where  $N_O$  is the number of  $Er^{3+}$  ions per  $cm^3$  of the host glass, and  $\int k(\lambda) d\lambda$  is the integrated absorption coefficient referred to the corresponding  $^4I_{15/2} \rightarrow J'$  (excited states)

absorption band. The  $\int k(\lambda)d\lambda$  values are calculated from the absorption spectra of  $\text{Er}^{3+}$ -doped sodium-zinc-tellurite glass fibers using a standard graphical integration procedure.

The ED transition probability  $A_{SLJ,S'L'J'}^{ed}$  underlying the spontaneous emission from  $(S'L'J')$  to  $(SLJ)$  states is given by [Reisfeld<sup>19</sup>]:

$$A_{SLJ,S'L'J'}^{ed} = \frac{64\pi^4 e^2 \bar{n}}{3h\bar{\lambda}^3} \frac{\chi_{ed}}{2J+1} S_{JJ'}^{ed} \quad (2.8)$$

where  $\chi_{ed} = (n^2 + 2)^2/9$  is a local field correction and  $S_{ed}$  is the ED oscillator strength given by Eq. (2.5). For magnetic dipole transitions, the line strength  $S_{md}$  is given by:

$$S_{JJ'}^{md} = \left( \frac{e\hbar}{2m_e c} \right)^2 \left| \left\langle f^N \gamma [SL]J \left| \left( \hat{L} + 2\hat{S} \right) f^N \gamma [S'L']J' \right\rangle \right|^2 \quad (2.9)$$

where  $\hat{L} + 2\hat{S}$  is the MD operator. The spontaneous emission probability  $A_{SLJ,S'L'J'}^{md}$  corresponding to MD transitions is given by:

$$A_{JJ'}^{md} = \frac{64\pi}{3\bar{\lambda}^3} \frac{\chi_{md}}{2J+1} S_{JJ'}^{md} \quad (2.10)$$

where  $\chi_{ed} = n^3$  is the local field correction for MD transitions, and  $S_{md}$  is the MD oscillator strength given by Eq. (3.15). However, in glasses, the contributions of magnetic dipole and electric quadrupole transitions are usually weak in comparison to the electric dipole contribution. This fact can be attributed to the low degree of symmetry associated with the rare earth site in the glass medium [Reisfeld<sup>19</sup>].

The standard method for obtaining  $\Omega_k$  parameters is to choose the values that minimize the root mean square deviation between observed oscillator strengths given by Eq. (2.7) and those calculated by Eq. (2.6). The oscillator strength for any emission can be calculated using the  $\Omega_k$  parameters obtained with Eq. (2.6). The total radiative

probability  $A_{JJ'}$  of intermanifold  $J \rightarrow J'$  transitions for erbium ion in our glass (the formula is valid for any lanthanide ion in any host) is the sum of ED and MD transition probabilities,  $A_{JJ'}^{ed}$  and  $A_{JJ'}^{md}$ , respectively, and it might be calculated using the formula

$$A_{JJ'} = A_{JJ'}^{ed} + A_{JJ'}^{md} = \frac{64\pi^4 e^2}{3h(2J+1)\lambda^3} \left[ \frac{(\bar{n}^2 + 2)^2}{9\bar{n}} S_{ed} + \bar{n}^3 S_{md} \right]. \quad (2.11)$$

The emission cross section is related to the radiative probability by the transition

$$\sigma(\lambda_p) = \frac{\lambda_p^4}{8\pi n^2 \Delta\lambda_{eff}} A_{JJ'} \quad (2.12)$$

where the linewidth  $\Delta\lambda_{eff}$  is used for glasses because the emission bands as well as absorption bands are characteristically asymmetrical. The radiative lifetime of level  $J$  can be expressed in terms of spontaneous emission probabilities as

$$\tau_J^{-1} = \sum_{J'} A_{JJ'} \quad (2.13)$$

where the summation is over all terminal levels  $J'$ . The Judd-Ofelt analysis makes it possible to obtain spectroscopic parameters, such as the stimulated emission transition cross-section or the radiative lifetime for any  $4f - 4f$  transition.

The Judd-Ofelt formalism has been applied to the analysis of a number of systems. In most cases, the crystal field splitting of the terms was neglected. Therefore, the total absorption intensities between the ground term and the excited terms were analyzed with only three empirical parameters  $\Omega_k$  ( $k = 2, 4, 6$ ). Values of Judd-Ofelt parameters for different oxide glasses are given in Table 2.1 [Chen *et al.*<sup>20</sup>].



Type of glasses		Tellurite glass	Germanate glass	Cadmium Phosphate	Calcium Phosphate	Strontium Phosphate	Barium Phosphate	Silicate glass
J-O parameters ( $10^{-20} \text{ cm}^2$ )	$\Omega_2$	6.30	4.76	5.34	5.48	5.04	5.02	4.05
	$\Omega_4$	1.55	1.20	1.22	1.29	1.29	1.27	0.70
	$\Omega_6$	1.29	0.80	0.85	0.76	0.93	0.92	0.40
Error (%)		1.2	6.4	5.8	13.0	0.2	10.9	4.1

Table 2.1 Calculated Judd-Ofelt parameters for different oxide glasses.

As can be seen from the Table 2.1, Judd-Ofelt parameters are the largest for tellurite glasses, suggesting the strongest erbium transitions in that particular host.

### 2.3 Electronic polarizability and index of refraction

Equations (2.6) – (2.11) show the strong dependence of the emission on the refractive index ( $n$ ): glasses and fibers with higher  $n$  should exhibit a stronger oscillator strengths and emission than those with a lower refractive index. In order to understand why tellurite glasses have higher  $n$  values, we need to consider the number of polarizable atoms/unit volume ( $N/V$ ), the electronic polarizability ( $\alpha_e$ ) of the ion, and the ionic polarizability ( $\alpha_{\text{ionic}}$ ). The values of  $n$  in  $\text{TeO}_2$  glasses (2.2) differ from to that of the crystal (2.37) due to the difference in density  $\rho$  of the glass ( $5.1 \text{ g/cm}^3$ ) compared to that of the crystal ( $5.99 \text{ g/cm}^3$ ). Note, that  $n_{\text{crystal}}/n_{\text{glass}} = 1.077$ , which is close to  $\rho_{\text{crystal}}/\rho_{\text{glass}} = 1.175$ . The dielectric constant and static polarizability  $\alpha$  are lower in the glass than in the crystal form of  $\text{TeO}_2$ . Tellurite glass has a lower  $n$  than tellurite crystal from lower electronic polarizability  $\alpha$ , lower  $N/V$  and lower number of bonds per unit

volume  $n_b$ . All these quantities of the  $\text{TeO}_2$  unit are crucial in determining the  $n$  of binary and ternary tellurite glasses.

At optical frequencies, where the refractive index is usually measured, the dielectric constant arises almost entirely from electronic polarizability, which can be written as:

$$\alpha = \frac{e^2 h^2}{4\pi^2 \epsilon_0 m_e} \sum_k \frac{f_k}{E_k^2 - (h\nu)^2}, \quad (2.14)$$

where  $e$  is the electronic charge ( $1.602 \times 10^{-19}$  C),  $h$  is Planck constant ( $6.626 \times 10^{-34}$  J·s),  $m_e$  is the electron mass ( $9.11 \times 10^{-31}$  kg),  $f_k$  represents the oscillator strength from the ground state to an excited state  $k$ ,  $E_k$  is the excitation energy, and  $\nu$  is the frequency of the incident photons.

According to Maxwell's theory, the relationship  $n^2 = \epsilon_{\lambda \rightarrow \infty}$  holds for long wavelengths. The Clausius-Mossotti equation presents relation between  $n$  (or  $\epsilon$ ) and  $\alpha$ :

$$\frac{4\pi}{3} \sum_i \frac{N_i \alpha_i}{V} = \frac{\epsilon_\infty - 1}{\epsilon_\infty + 2} = \frac{n^2 - 1}{n^2 + 2} = \frac{4\pi}{3} \frac{\rho}{M} N_A \alpha_m = \frac{4\pi}{3} \frac{\alpha_m}{V_m}, \quad (2.15)$$

where  $N_i/V$  is the number of type  $i$  atoms per unit volume, which has electronic polarizabilities  $\alpha_i \equiv p_i/E_{loc}$  ( $p_i$  is the dipole moment and  $E_{loc}$  is local electric field),  $\rho$  is a density,  $M$  is a molecular weight,  $N_A$  is the Avogadro's number, and  $V_m$  is the molar volume. Here  $\alpha_m$  is the polarizability of the atoms that make up the molecular formula unit, where additivity is assumed: the polarizabilities are additive and are the same in different compounds for the same molecular units [Burns<sup>21</sup>, Tessman *et al.*<sup>22</sup>]. Molar volumes for our tellurite glasses are calculated from the molecular weight and density of the glass:

$$V_m = M_g / \rho, \quad (2.16)$$

$$M_g = xM(\text{dopant}) + (1-x)M(\text{TeO}_2), \quad (2.17)$$

with  $\rho$  as the density.

As indicated in Eq. (2.15), called the Lorenz-Lorentz equation for  $n^2 = \epsilon_{\lambda \rightarrow \infty}$ , the refractive index depends upon the composition of an optical material; the more polarizable the outer electronic shell, the higher the refractive index (inner electrons are in filled shells that do not contribute as much to atom polarizability). In general, ionic polarizability that results from the displacement of ions of opposite signs from their regular sites due to the applied electric field should also be taken in account, but its order of magnitude is much smaller than that of an electronic polarizability, and does not contribute at optical frequencies.

Glass	Atom, Valence Z, Coordination number, Electronegativity $\chi$	Oxide (mol %)	$\rho$ (g/cm <sup>3</sup> )	$n_0$	$V_m$ (cm <sup>3</sup> /mol)	$a_m$ (Å <sup>3</sup> )
Li <sub>2</sub> O [25]	<sup>3</sup> Li, Li <sup>+</sup> 4,6 0.98	15	5.005	1.99	28.00	5.518
		20	4.895	1.98	27.30	5.343
		25	4.799	1.95	26.50	5.077
		30	4.624	1.92	26.10	4.887
Na <sub>2</sub> O [26]	<sup>11</sup> Na, Na <sup>+</sup> 4,6 0.93	5	5.406	2.13	28.62	6.145
		10	5.242	2.07	28.58	5.928
		13	5.050	2.03	29.09	5.885
		17	4.849	2.001	29.49	5.855
		20	4.647	1.93	30.14	5.693
K <sub>2</sub> O [26]	<sup>19</sup> K, K <sup>+</sup> 6,10,12 0.82	23	4.450	1.887	30.82	5.631
		4.85	5.315	2.11	29.44	6.248
		9.40	5.037	2.05	30.47	6.243
		12.90	4.802	2.005	31.48	6.267
		15.60	4.619	1.964	32.34	6.260
ZnO [26]	<sup>30</sup> Zn, Zn <sup>2+</sup> 4,6 1.65	17.30	4.516	1.925	32.83	6.178
		10.1	5.556	2.13	27.32	5.868
		20.0	5.534	2.08	26.01	5.430
		30.0	5.465	2.03	24.91	5.039
		40.0	5.457	1.982	23.51	4.610
WO <sub>3</sub> [27]	<sup>74</sup> W, W <sup>6+</sup> 6-12 2.36	45.0	5.408	1.954	23.00	4.422
		10	5.730	2.166	29.09	6.373
		20	5.892	2.169	29.55	6.472
		30	5.984	2.172	30.25	6.650

Table 2.2 Optical characteristics of binary tellurite glasses.

The values of coordination number, valence  $Z$ , electronegativity  $\chi$ , density  $\rho$ , linear refractive index  $n_0$ , molar volume  $V_m$ , and molar polarizability  $\alpha_m$ , of some binary tellurite glasses are given in Table 2.3 (density of pure  $\text{TeO}_2$  glass is  $\sim 5.1 \text{ g/cm}^3$  and index of refraction is  $\sim 2.2$ ) [Dimitrov & T. Komatsu<sup>23</sup>, Katagiri *et al.*<sup>24</sup>, Mazurin *et al.*<sup>25</sup>, Kim *et al.*<sup>26</sup>, Vogel<sup>27</sup>, Greenwood & Earnshaw<sup>28</sup>, Lide<sup>29</sup>]. From Table 2.2 we see that the density, linear refractive index and polarizability per unit volume all decrease with increasing concentration of dopants in all cases, except for tungsten for which the trend is the opposite. Valence and coordination number are highest in case of tungsten-tellurite glass. Here, we show that this is the main reason for overall the strongest erbium emission in tungsten-tellurite among all oxide glasses.

Electronegativity was defined by Pauling as the power of an atom in a molecule to attract electrons to it. The effect of polarizability of the first neighbor ions could be expressed through the concept of average electronegativity introduced by Asokamani and Manjula [Asokamani & Manjula<sup>30</sup>]. They defined an average electronegativity parameter ( $\chi_{lav}$ ) in the following manner:

$$(\chi_{lav}) = \frac{\sum_{i=1}^N \chi_i n_i}{N} \quad (2.18)$$

where  $\chi_i$  is the Pauling [Reddy & Ahammed<sup>31</sup>] electronegativity,  $n_i$  the number of atoms of the  $i$ th elements and  $N$  is the number of elements present in the compound. From [Duffy & Ingram<sup>32-34</sup>, Duffy<sup>35</sup>, Reddy *et al.*<sup>36</sup>], the following empirical relation is derived for the average electronic polarizability of the oxygen ion ( $\alpha_{O^{2-}}$ ):

$$\alpha_{O^{2-}} = 4.624 - 0.7569 \chi_{lav} \quad (2.19)$$

By taking the average electronegativity values of simple oxides, the average electronegativities for the binary oxide glasses of the form  $XA_pO_qYB_rO_s$  can be calculated as:

$$\chi_{2av} = \frac{X\chi_f + Y\chi_s}{X + Y}, \quad (2.20)$$

where  $\chi_{2av}$  is the average electronegativity of the binary oxide glasses.  $X$  and  $Y$  are the first and second oxide (in mol %) compositions in binary oxide glasses,  $\chi_f$  and  $\chi_s$  are the average electronegativities of first and second oxides in the binary oxide glasses [Reddy *et al.*<sup>37</sup>]. For  $TeO_2$  as second oxide in the composition and alkaline and alkaline earth oxides, the oxygen average polarizability was:

$$\alpha_{O^{2-}} = 3.319 - 0.3422\chi_{2av}. \quad (2.21)$$

The average electronegativity  $\chi_{2av}$  and theoretical values of the average oxygen electronic polarizability  $\alpha_{O^{2-}}$  ( $\times 10^{-24} \text{ cm}^3$ ) of ZnO- and  $WO_3$ -doped tellurite glasses, used in this thesis, are given in Table 2.3 [Duffy<sup>35</sup>].

Species		$\chi_{2av}$	$\alpha_{O^{2-}} (\times 10^{-24} \text{ cm}^3)$
ZnO		$\chi_{1av} = 2.580$	...
ZnO- $TeO_2$ ZnO (mol %)	10.1	2.96	2.318
	20	2.918	2.275
	30	2.876	2.258
	40	2.833	2.212
	45	2.812	2.205
$WO_3$		$\chi_{1av} = 2.975$	...
$WO_3$ - $TeO_2$ $WO_3$ (mol %)	10	3.002	2.344
	20	2.997	2.349
	30	2.994	2.387
$TeO_2$		$\chi_{1av} = 3.003$	...

Table 2.3 Average electronegativity and electronic polarizability of ZnO and  $WO_3$  tellurite glass.

The average oxygen electronic polarizability  $\alpha_{O^{2-}}$  decreases for increasing ZnO concentration. In case of tungsten-oxide,  $\alpha_{O^{2-}}$  value first increases when up to 20% of  $WO_3$  is added to  $TeO_2$  glass. Then,  $\alpha_{O^{2-}}$  value decreases as more  $WO_3$  is added. Since the average oxygen electronic polarizability is directly related to the index of refraction, we should expect the same trend of  $n$ . Interestingly enough, this suggests that the highest index of refraction of  $WO_3$ - $TeO_2$  glass would be for 20%  $WO_3$ .

## Bibliography

- [1] S. Sudo, (Ed.), *Optical Fiber Amplifiers* (Artech House, Inc., Boston, 1997).
- [2] G. Herzberg, *Atomic Spectra and Atomic Structure* (Dover, New York, 1944), pp. 120-151.
- [3] E. Desurvire, J.R. Simpson, *Optics Lett.*, **15** (1990) 547.
- [4] P.C. Backer, N.A. Olsson, J.R. Simpson, *Erbium-Doped Fiber Amplifiers – Fundamentals and Technology* (Academic Press, San Diego, 1999).
- [5] A. Yariv, *Optical Electronics*, 3<sup>rd</sup> ed. (Holt, Rinehart, and Wilson, New York, 1985), p. 130. [6] R.S. Quimby, W.J. Miniscalco, B. Thompson, *Fiber Laser Sources and Amplifiers*, Vol. **1581** (SPIE, 1991), pp. 72-79.
- [7] R.S. Quimby, *Appl. Optics* **30** (1991) 2546.
- [8] R.S. Quimby, W.J. Miniscalco, B. Thompson, *Tech. Digest of OAA '92*, Vol. **17** (1992) 67.

- [9] R.S. Quimby, W.J. Miniscalco, B. Thompson, *Fiber Laser Sources and Amplifiers*, Vol. **1789** (SPIE, 1992), pp. 50-57.
- [10] B.J. Ainslie, S.P. Craig-Ryan, S.T. Davey, J.R. Armitage, C.G. Atkins, R. Wyatt, *Tech. Digest of IOOC '89*, Vol. **3** (1989), pp. 22-23.
- [11] C.B. Layne, W.H. Lowdermilk, M.J. Weber, *Phys. Rev. B*, **16** (1977) 10.
- [12] J.H. Van Vleck, *J. Chem. Phys.* **41** (1937) 67.
- [13] L.J.F. Broer, C.J. Gorter, J. Hoogschagen, *Physica* **11** (1945) 231.
- [14] B.R. Judd, *Phys. Rev. B* **127** (1962) 750.
- [15] G.S. Ofelt, *J. Chem. Phys.* **37** (1962) 511.
- [16] E. Desurvire, *Erbium Doped Fiber Amplifiers* (John Wiley & Sons, Inc., New York, 1994).
- [17] M.J. Weber, *Phys. Rev.* **157** (1967) 262
- [18] J.R. Chamberlain, A.C. Everitt, J.W. Orton, *J. Phys.* **C1** (1968) 157.
- [19] R. Reisfeld, *Struct. Bonding* **22** (1975) 123.
- [20] B. J. Chen, G. C. Righini, M. Bettinelli, A. Speghini, *J. Non-Cryst. Solids* **322** (2003) 319.
- [21] G. Burns, *Solid State Physics* (Academic Press, Boston, 1985).
- [22] J.R. Tessman, A.H. Kahn, W. Schockley, *Phys. Rev.* **92** (1953) 890.
- [23] V. Dimitrov, T. Komatsu, *J. Non-Cryst. Solids* **249** (1999) 160.
- [24] Y. Katagiri, H. Nasu, J. Matsuoka, K. Kamiya, *J. Am. Ceram. Soc.* **77** (1994) 673.
- [25] O. Mazurin, M. Stretsina, T. Shvaiko-Shvaikovskaya (Eds.), *Handbook of Glass data: Single component and Binary Non-Silicate Oxide Glasses*, Physical Science Data **15**, Part B (Elsevier, Amsterdam, 1985).

- [26] S.H. Kim, T. Yoko, S. Sakka, *J. Am. Ceram. Soc.* **78** (1993) 1061.
- [27] W. Vogel, *Chemistry of Glasses*, edited by N. Kreidl (The American Ceramic Society, Columbus, 1985), p.344.
- [28] N.N. Greenwood, A. Earnshaw, *Chemistry of Elements* (Pergamon Press, Oxford, 1990).
- [29] D.R. Lide (Ed.), *Handbook of Chemistry and Physics*, 80<sup>th</sup> edit. (CRC Press, Boca Raton, 1999).
- [30] R. Asokamani, R. Manjula, *Phys. Rev. B* **39** (1989) 4217.
- [31] R.R. Reddy, Y. Nazeer Ahammed, *Cryst. Res. Technol.* **30** (1995) 263.
- [32] J.A. Duffy, M.D. Ingram, *J. Am. Chem. Soc.* **93** (1971) 6448.
- [33] J.A. Duffy, M.D. Ingram, *J. Non-Cryst. Solids* **21** (1976) 373.
- [34] J.A. Duffy, M.D. Ingram, in: N.J. Kreidl, D.R. Uhlmann (Eds.), *Optical Properties of Glass* (American Ceramic Society, New York, 1991).
- [35] J.A. Duffy, *Bonding, Energy Levels and Bands in Inorganic Solids* (Longmann, London, 1990).
- [36] R.R. Reddy, Y. Nazeer Ahammed, P. Abdul Azeem, K. Rama Gopal, T.V.R. Rao, *J. Non-Cryst. Solids* **286** (2001) 169.
- [37] R.R. Reddy, Y. Nazeer Ahammed, K. Rama Gopal, D.V. Raghuram, *Opt. Mater.* **10** (1998) 95.



## Chapter 3

### Techniques and materials

#### 3.1 Samples preparation

The primary tellurite glasses studied were doped with Na and Zn. The main reasons for choosing sodium and zinc were that sodium enhances rare-earth solubility and zinc, optical transparency and chemical durability. In addition, sodium-tellurite and zinc-tellurite glasses offer the widest glass-forming regions: 5 mol% – 38 mol% for  $\text{Na}_2\text{O}:\text{TeO}_2$  and 17 mol% – 38 mol% for  $\text{ZnO}:\text{TeO}_2$  glass. All sodium-zinc-tellurite glasses in this work also contained 0.1 – 0.4 wt%  $\text{Er}_2\text{O}_3$ , which was added in order to characterize the erbium emission, but is not likely to affect any bulk structure discussed here.

Glass	$\text{TeO}_2$ (mol%)	$\text{ZnO}$ (mol%)	$\text{Na}_2\text{O}$ (mol%)
1	80	20	-
2	72.5	27.5	-
3	65	35	-
4	79	15	5
5	75	20	5
6	67.5	27.5	5
7	60	35	5
8	75	15	10
9	67.5	22.5	10
10	60	30	10

Table 3.1 Sodium-zinc-tellurite glass compositions used in experiments.

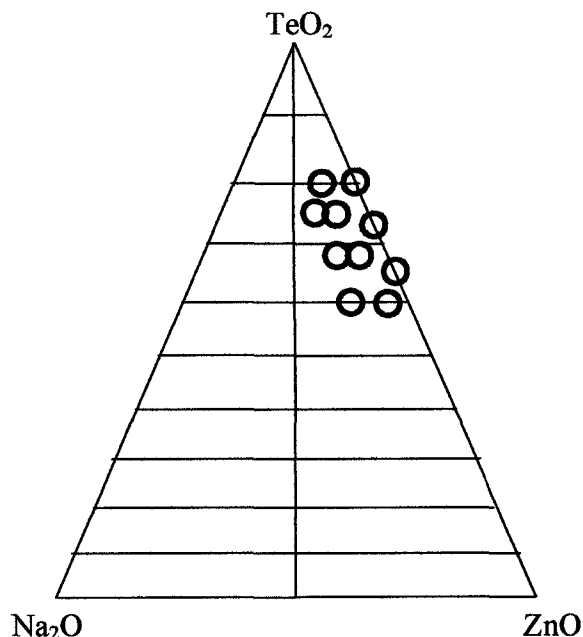


FIG. 3.1 Ternary diagram of  $\text{Na}_2\text{O}$ - $\text{ZnO}$ - $\text{TeO}_2$  glasses used in this study.

Optically transparent tellurite glasses were prepared from starting materials purified using chlorine gas in a controlled atmosphere glove box with various molar base compositions, as given in Table 3.1 and presented on the ternary diagram in FIG. 3.1. Optical fiber preforms were prepared by melting core and clad glasses in separate crucibles simultaneously at 1073K. The molten cladding glass was first cast in a cylindrical gold-coated brass mold. After a waiting period of a few seconds, the liquid partially drained from a bottom opening. This draining occurs from the center region and produces a tube-shaped cladding. The center hole is then filled with the molten core glass and this preform is then annealed at the glass transition temperature. Later, the preform is stretched to a few millimeter diameter size and overladdled with a protective oxide glass tube. This final form is then drawn into a fiber and coated with a UV-cured

polymer. The optical fibers thus fabricated had a numerical aperture (NA) of about 0.2, a core diameter of 3  $\mu\text{m}$  and an erbium concentration of 2000ppm.

Alkali-tungsten-tellurite glasses were used for comparison and their compositions are shown in Table 3.2 and FIG. 3.2. This glass series emphasizes the substitution of tellurite by tungsten oxide with a constant alkali oxide content (I – IV), the substitution of tungsten by alkali oxide with a constant tellurite oxide content (V – VII) and the substitution of lithium by potassium oxide with a constant tellurite oxide content (I, VI and VII). All tungsten-tellurite glasses here also contained 0.1 wt%  $\text{Tm}_2\text{O}_3$ , which was added in order to characterize the laser properties but is not likely to affect any bulk structure discussed in this work. In addition, a tungsten-free  $20\text{Li}_2\text{O} \cdot 80\text{TeO}_2$  sample was used as a reference for X-ray Photoelectron Spectroscopy (XPS) spectra. The tungsten-tellurite samples were provided by Jas Sanghera from the Naval Research Laboratory (NRL).

Glass	$\text{TeO}_2$ (%)	$\text{WO}_3$ (%)	$\text{Li}_2\text{O}$ (%)	$\text{K}_2\text{O}$ (%)
I	65	24.9	10	-
II	70	19.9	10	-
III	75	14.9	10	-
IV	80	10	10	-
IV	70	24.9	5	-
V	65	19.9	15	-
VI	65	24.9	5	5
VII	65	24.9	-	10

Table 3.2 Alkali-tungsten-tellurite glass compositions used in experiments.

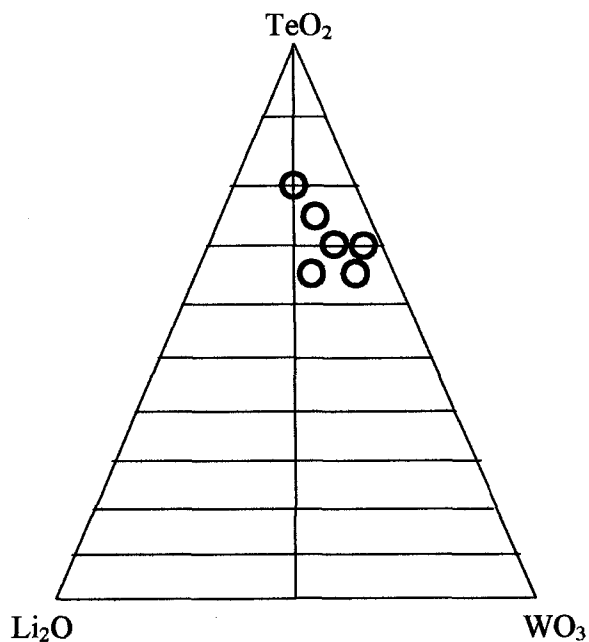


FIG. 3.2 Ternary diagram of  $\text{Li}_2\text{O}$ - $\text{WO}_3$ - $\text{TeO}_2$  glasses used in this study.

The glasses were melted from reagent grade  $\text{Li}_2\text{CO}_3$  (Alfa Aesar, Puratronic Grade, 99.999%),  $\text{K}_2\text{CO}_3$  (Alfa Aesar, Puratronic Grade, 99.999%),  $\text{WO}_3$  (Alfa Aesar, Puratronic Grade, 99.998%),  $\text{TeO}_2$  (Alfa Aesar Puratronic Grade, 99.9995%) and  $\text{Tm}_2\text{O}_3$  (Rhône-Poulenc, 99.90%). These compounds were mixed in the appropriate ratios into 15-gram batches. The mixtures were first calcined and then homogenized by heating to  $850^\circ\text{C}$  in gold crucibles in air for 4 hours. After removal from the furnace, the samples were cooled in air to room temperature. The glasses were then annealed at  $350^\circ\text{C}$  for 2 hours. To make the 20  $\text{Li}_2\text{O}$ \*80  $\text{TeO}_2$ , the melt was quickly quenched in water after removal from the furnace. The reason for this quick quench was that this particular sample was just outside the glass-forming region. Glass transition temperatures are given in Table 3.3 [Lim *et al.*<sup>1</sup>].

Composition (mol %)	Glass Transition Temperature (T <sub>g</sub> )
20Li <sub>2</sub> O*80TeO <sub>2</sub>	259 °C
xK <sub>2</sub> O*(10-x)Li <sub>2</sub> O*25WO <sub>3</sub> *65TeO <sub>2</sub>	
x = 0	335 °C
5	331 °C
10	339 °C
10Li <sub>2</sub> O*xWO <sub>3</sub> *(90-x)TeO <sub>2</sub>	
x = 5	283 °C
10	304 °C
15	321 °C
20	334 °C
25	335 °C

Table 3.3 Glass composition and glass transition temperature.

### 3.2 Raman spectroscopy

Since the Raman spectroscopy was widely used in this study, it is described here in details [Wadsack<sup>2</sup>]. The Raman effect can most easily be visualized as the inelastic scattering of light by a physical system. That may include individual molecules in a gaseous or liquid state, crystalline or amorphous solids, powders, etc. Raman scattering is the process by which an incident photon of energy  $\hbar\omega_i$  interacts with matter to produce a scattered photon of energy  $\hbar\omega_s \neq \hbar\omega_i$ . In the process, the physical system has either gained or lost energy according to whether  $\hbar(\omega_i - \omega_s)$  is positive or negative. For historical reasons, the scattered light in the former case is referred to as Stokes radiation and in the latter as anti-Stokes radiation. Since its discovery in 1928, the Raman effect has served as a valuable probe of the symmetry, structural and vibrational properties of gases, liquids, and solids [Szymanski<sup>3</sup>].

The Raman effect has traditionally been associated with the vibrationally excited states of a substance, although there are separate vibronic and electronic Raman effects. In the electronic Raman effect, light is inelastically scattered with an accompanying change in the electronic states of the ionic constituents. For the vibronic Raman effect, the initial and final electronic states are tacitly assumed to be the same; in the electronic case, they must be different.

The essential features of Raman scattering can be understood by reference to the simple case of the vibronic Raman effect in a crystalline solid. At a point  $R$  in the crystal, let the incident light be represented by an electric field  $E = E_0 \mathbf{e}_i \cos(\mathbf{k}_i \cdot \mathbf{R} - \omega_i t)$ , where  $\mathbf{e}_i$  specifies the polarization and  $\mathbf{k}_i$ , the propagation direction. The electric field induces a polarization in the crystal specified by  $P$ , the instantaneous average dipole moment per unit volume. In a region large compared to lattice dimensions, but small compared to the wavelength of light, a phenomenological relation may be written for  $P$  and  $E$ :  $P = \alpha \cdot E$ , where  $\alpha$  is the instantaneous polarizability of the medium.

Vibrations of the crystal lattice can be described in terms of its fundamental normal modes of oscillation:  $Q_\gamma = Q_\gamma^0 \cos(\mathbf{q} \cdot \mathbf{R} - \omega_\gamma t + \theta_\gamma)$ , where  $\mathbf{q}$  is the propagation vector;  $\omega_\gamma$ , the frequency; and  $\theta_\gamma$ , an arbitrary phase angle. These cooperative excitations of the lattice are called phonons. The lattice vibrations will modulate the instantaneous polarizability, i.e., one may express  $\alpha$  in terms of the  $\theta_\gamma$  by

$$\alpha_{\sigma\rho} = \alpha_{\sigma\rho}^{(0)} + \sum_{\gamma} \alpha_{\sigma\rho\gamma}^{(1)} Q_{\gamma} . \quad (3.1)$$

Here,  $\alpha_{\sigma\rho\gamma}^{(1)}$  is third order rank tensor, defined from Taylor expansion of  $\alpha$  in terms of  $Q$ :

$$\alpha_{\sigma\rho\gamma}^{(1)} \equiv \left. \frac{\partial \alpha_{\sigma\rho}}{\partial Q_\gamma} \right|_{Q=0} . \quad (3.2)$$

The polarization  $P$  then has two parts:  $P^{(0)} = \alpha^{(0)} \cdot E$  and

$$P_\sigma^{(1)} = \sum_{\rho\gamma} \alpha_{\sigma\rho\gamma}^{(1)} E_\rho Q_\gamma . \quad (3.3)$$

The first term  $P^{(0)}$  oscillates at the same frequency as the incident light because  $\alpha^{(0)}$  is the static, unmodulated part of the polarizability. This unshifted light is known as Rayleigh scattering. The second term,  $P^{(1)}$ , mixes the frequencies  $\omega_i$  and  $\omega_s$  to produce Raman scattering. Explicitly,  $P^{(1)}$  is:

$$P_\sigma^{(1)} = \sum_{\rho\gamma} \alpha_{\sigma\rho\gamma}^{(1)} e_{i\rho} Q_\gamma^0 E^0 \cos(\vec{k}_i \cdot \vec{R} - \omega_i t) \cos(\vec{q} \cdot \vec{R} - \omega_\gamma t + \theta_\gamma), \quad (3.4)$$

which can be rewritten in terms of:  $P_\sigma^{(1)}$  (Stokes) and  $P_\sigma^{(1)}$  (anti-Stokes):

$$P_\sigma^{(1)}(Stokes) = \frac{E_0}{2} \sum_{\rho\gamma} \alpha_{\sigma\rho\gamma}^{(1)} e_{i\rho} Q_\gamma^0 \cos[(\vec{k}_i - \vec{q}) \cdot \vec{R} - (\omega_i - \omega_\gamma)t - \theta_\gamma] \quad (3.5)$$

and

$$P_\sigma^{(1)}(anti - Stokes) = \frac{E_0}{2} \sum_{\rho\gamma} \alpha_{\sigma\rho\gamma}^{(1)} e_{i\rho} Q_\gamma^0 \cos[(\vec{k}_i + \vec{q}) \cdot \vec{R} - (\omega_i + \omega_\gamma)t + \theta_\gamma]. \quad (3.6)$$

Two conservation laws are immediately evident, one for “momentum” and the other for “energy.”

	Momentum	Energy
Stokes	$\mathbf{k}_s = \mathbf{k}_i - \mathbf{q}$	$\omega_s = \omega_i - \omega_\gamma$
Anti-Stokes	$\mathbf{k}_s' = \mathbf{k}_i + \mathbf{q}$	$\omega_s' = \omega_i + \omega_\gamma.$

These are illustrated in FIG. 3.3. Furthermore, because of the arbitrary phase angles  $\theta_\gamma$ , (spontaneous) Raman scattering is incoherent.

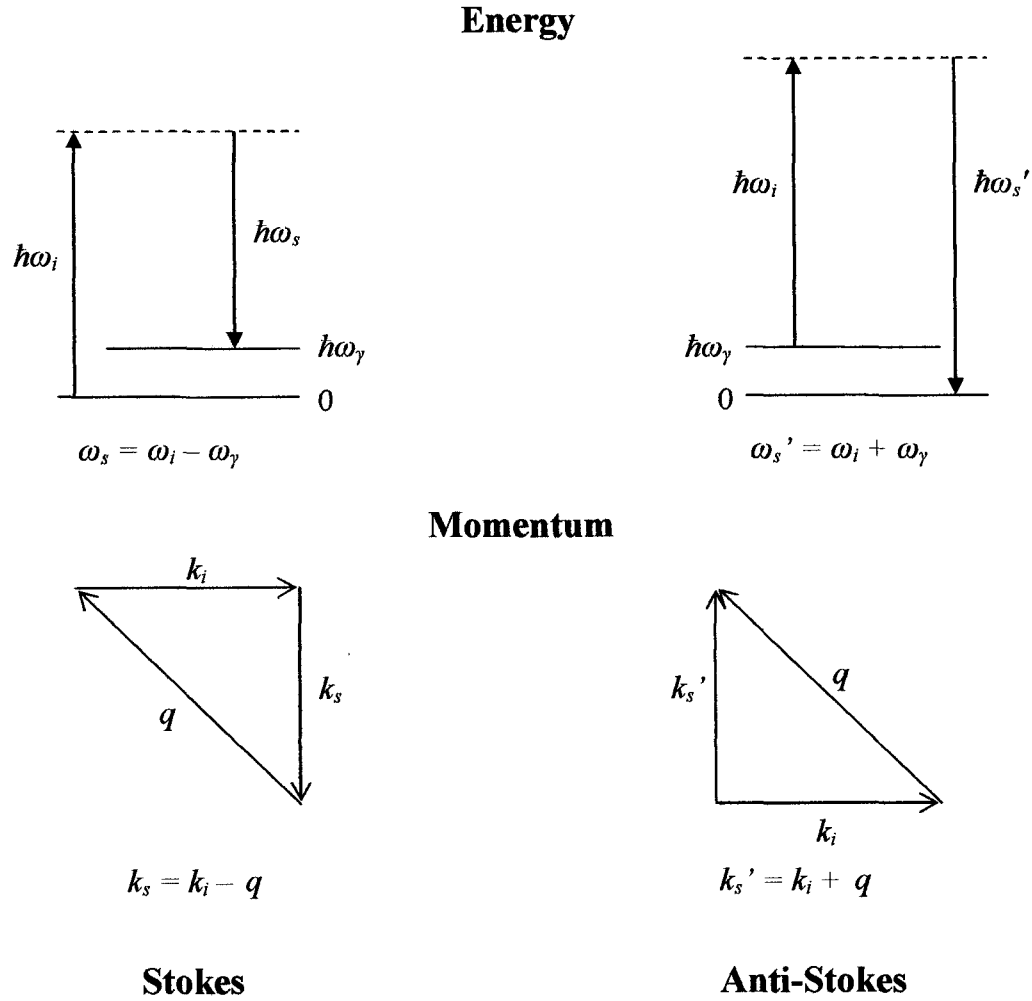


FIG 3.3 Conservation Laws for the Vibrational Raman effect in crystalline solids.

The radiation from the classical oscillating dipole moment  $P_\sigma^{(I)}$  is proportional to  $\omega_s^4$ . The anti-Stokes/Stokes intensity ratio should then be

$$\frac{I_\gamma(\text{anti-Stokes})}{I_\gamma(\text{Stokes})} = \left( \frac{\omega_i + \omega_\gamma}{\omega_i - \omega_\gamma} \right)^4. \quad (3.7)$$



However, it is also necessary to take into account the thermal population difference between the initial and final states. When this is done, the anti-Stokes (excited state) radiation is reduced by the Boltzmann factor:

$$\frac{I_{\gamma}(\text{anti-Stokes})}{I_{\gamma}(\text{Stokes})} = \left( \frac{\omega_i + \omega_{\gamma}}{\omega_i - \omega_{\gamma}} \right)^4 \exp\left( -\frac{\hbar\omega_{\gamma}}{kT} \right). \quad (3.8)$$

Conversely, if the intensities and the frequency shift  $\omega_{\gamma}$  are measured, then the above relation allows one to determine the true temperature of the scatterers.

Symmetry-allowed transitions are determined by the non-zero values of  $\alpha_{\sigma\rho\gamma}^{(1)}$  through the transformation properties of the bilinear expression

$$(P_{\sigma}^{(1)})_{rms} = \frac{E_0}{2\sqrt{2}} \sum_{\rho\gamma} \alpha_{\sigma\rho\gamma}^{(1)} e_{i\rho} Q_{\gamma}^0 \quad (3.9)$$

of the two variables  $e_{i\rho}$  and  $Q_{\gamma}^i$ . The index  $\rho$  runs over  $x, y, z$ ; consequently,  $e_{i\rho}$  transforms like  $x, y, z$  under the symmetry operations of the point group of the crystal. The variables  $Q_{\gamma}^0$  transform according to the irreducible representations of the point group [Heine<sup>4</sup>]. The resultant  $\alpha^{(1)}$  matrices for the Raman-active irreducible representations of a given point group have been tabulated [Loudon<sup>5</sup>] for the case where  $\alpha^{(1)}$  is symmetric.

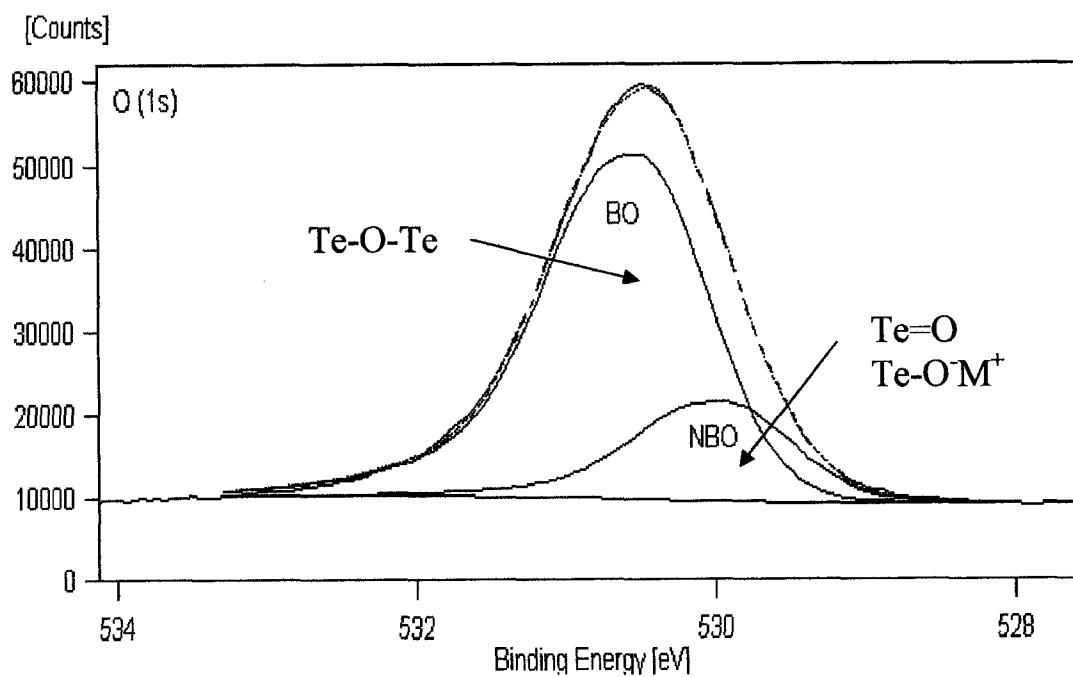
In this study, Vibrational Raman spectroscopy was used to identify the glass structural units. For these measurements, samples were cut to a size approximately  $1 \times 1 \times 0.5 \text{ cm}^3$ . Raman spectra of tellurite glasses were excited by the 514.5nm line of a 300mW Ar-ion laser, focused to a spot of radius  $\approx 50\mu\text{m}$ , from an angle of about  $90^\circ$  with respect to the sample surface. A monochromator (Jobin-Yvon U 1000) and standard photon-counting system were used as detector. Raman modes, both single and multi bond, provide information on the glass network and its connectivity. In addition, the

strength of the electron-phonon coupling can be obtained directly from the scattering intensity [Moawad *et al.*<sup>6</sup>].

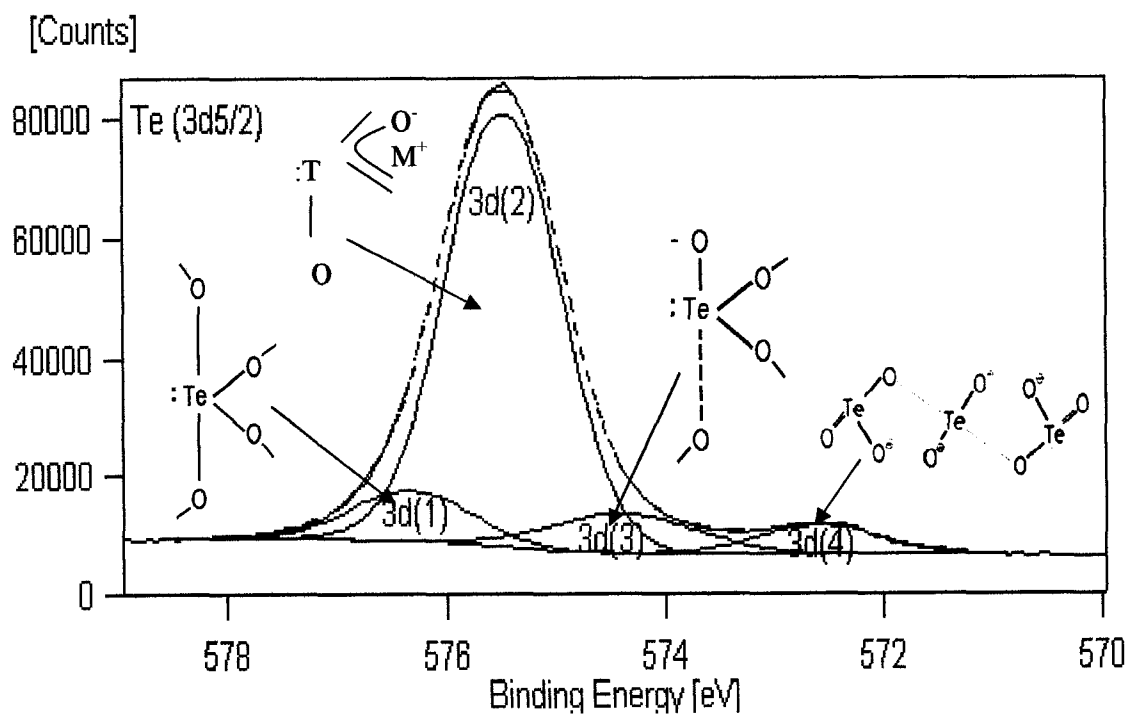
### 3.3 X-ray photoelectron spectroscopy (XPS)

The experimental XPS data were obtained by graduate students Hassan Moawad and Austin Lim in the group of Professor Himanshu Jain from the Materials Science Department at Lehigh University. Based on valence electron binding energies, XPS was used to determine the molecular units and their local environment [Moawad *et al.*<sup>6</sup>]. This species-selective technique measures the flux of electrons emitted from the sample as a function of their binding energy and more importantly on their environment. The binding energy of emitted electrons depends upon the particular atom from which they are emitted. In our experiments, the O-1s and the Te-3d<sub>5/2</sub> electrons were used as a probe of the chemical structure of the glass, shown in FIG. 3.4 a) and b).

FIG. 3.4.a) shows a typical O-1s XPS spectrum made up of two peaks representing bridging (BO) and non-bridging oxygen (NBO) atoms. FIG. 3.4.b) shows the Te-3d<sub>5/2</sub> XPS spectrum. The first one indicates two types of oxygen species. By comparison, the tellurium spectrum reveals a greater variety of environment, including molecular units TeO<sub>4</sub>, TeO<sub>3</sub>, TeO<sub>3+1</sub> and Te<sub>3</sub>O<sub>8</sub>. Larger peak widths than in the oxygen spectra may indicate a broad distribution of the local network environments, although they are not easy to compare directly. The integrated intensities of the corresponding peaks provide estimates of the fractions of each type of unit.



a)



b)

FIG 3.4 Binding energy of: a) The O-1s and b) the Te-3d<sub>5/2</sub> electrons.

For the XPS experiment, a high-resolution ESCA Scienta 300 spectrometer was used with monochromatic Al-K $\alpha$  X-rays of energy 1486.6 eV as the probe radiation. The glass samples were ground to 1mm thickness to give a flat surface for proper clamping in the sample holder. The samples were then fractured *in situ* in the ultra high vacuum (UHV) preparation chamber where the base pressure was approximately  $10^{-9}$  Torr. This procedure avoided any contamination of the fractured glass surface. After fracturing of the samples, XPS data were obtained immediately from the newly created surface. The photoelectrons were generated over an area about  $3 \times 1 \text{ mm}^2$ . The X-ray spot size was about  $1.6 \times 0.3 \text{ mm}^2$ .

The ESCA instrument was operated for survey scans over the entire binding energy range as well as for the regional scans over the photoelectron peaks of interest. The regions of interest were tungsten 4f (45~30eV), oxygen 1s (540~525eV), tellurium 3d<sub>5/2</sub> (585~565eV), carbon 1s (300~275eV), and valence band (25~0eV). A 0.1eV energy step was used for the regional scans. The instrumental contribution to the line width was extremely small (<4%). Therefore, the experimental widths were primarily a combination of charging and natural line widths. Six to eight scans were performed for each sample, to give a high signal to noise ratio. Since the samples are insulating, the glass surface exposed to the X-rays becomes positively charged due to emission of photoelectrons. In order to compensate for this charging effect, the sample surface was flooded with low energy electrons of about 4-8 eV, which gives a better resolution and reproducibility than the surface at neutral potential.

The spectra were analyzed using the Scienta software. A Shirley background was subtracted and a Voigt line shape, which is a mixture of Gaussian and Lorentzian, was

used to analyze the peaks for each specific element. Measured binding energies of the peaks were corrected, using the calibration factor calculated from the difference between the measured binding energy of the C-1s peak and its reference value of 284.6 eV.

### 3.4 Fiber characterization

FIG 3.5 shows the schematic diagram of a typical experimental setup with laser diode pumping for measurements of rare earth emission in fibers. Amplification of an optical signal in a fiber relies on the stimulated emission of optically excited rare earth ions in the fiber core. The operational principle of a fiber amplifier is the same as that of a laser, except that an amplifier does not require a cavity whereas a laser needs one for oscillations. Because of a high numerical aperture and single-mode operation, tellurite fibers make strongly waveguiding structures.

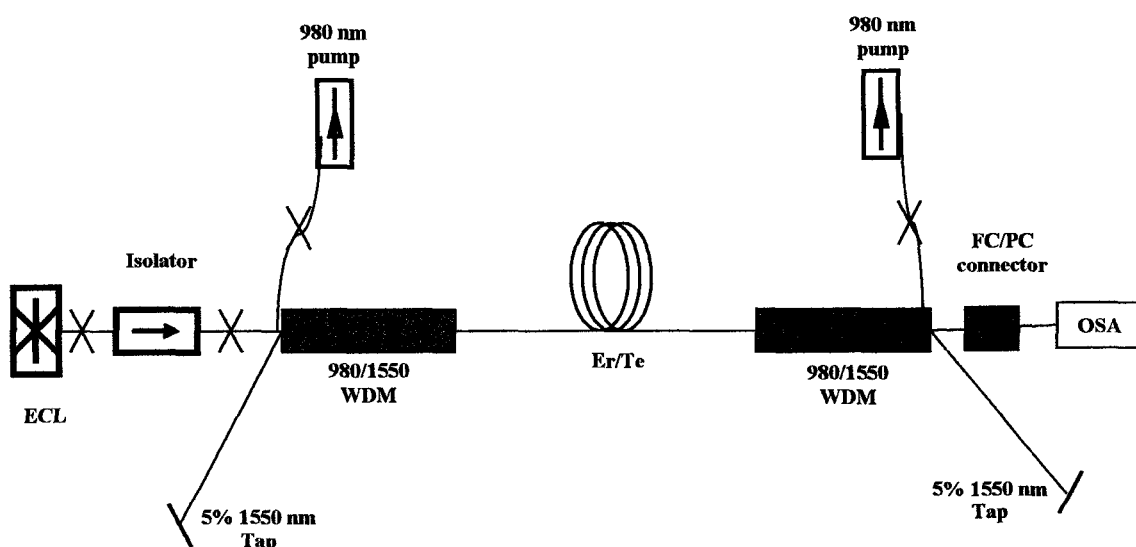


FIG. 3.5 A typical experimental setup used for fiber measurements.

In the present study, we measured the transmission spectra of light through erbium-doped  $\text{TeO}_2$  fibers and compared them with corresponding spectra in other glasses. For optical characterization, the tellurite fibers were mechanically spliced to silica fibers at both ends. 980nm and 1480nm diode lasers were used as co- and counter-pumps and the signal was generated by an external cavity laser (ECL) covering the wavelength range 1460-1660nm. Pump light and source signal were combined through a commercial silica-based 980/1550nm Wavelength Division Multiplexer (WDM), and the output signal was measured with an optical spectrum analyzer.

The most difficult part of the experiment was splicing the silica and tellurite fibers, schematically shown in FIG. 3.6. Tellurite fibers are very fragile, so we could not use standard tools such as cleavers and strippers. Instead, we used capillary tubes as protectors to glue and polish the ends of the  $\text{TeO}_2$  fiber. The Er doped tellurite fiber was butt-coupled with an Ultra High Numerical Aperture (UHNA) silica fiber, which was further spliced to the WDM output fiber (SM 28). We used standard micropositioners and standard microscope objectives for fiber alignment. Standard two-component epoxy like the one used here usually need some time to harden, and during that period, the previously aligned erbium doped tellurite and silica fibers could move. Because of these difficulties, typical time needed to make one good sample was a couple of days.

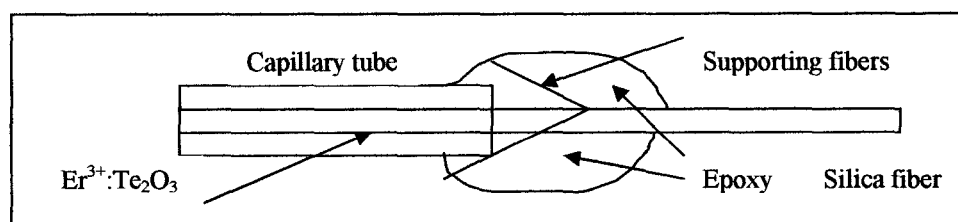


FIG. 3.6 Mechanical splice.

The polishing process was as follows: we started with 12  $\mu\text{m}$  polishing paper, then followed by 8  $\mu\text{m}$  paper, 5  $\mu\text{m}$ , and 1  $\mu\text{m}$  polishing paper. For finishing, we used 0.3  $\mu\text{m}$  polishing paper. It is very important to have very good polished ends, as good as one can make them, because the final loss of the signal depends on how flat the surface of the fiber is. We prepared several samples with different length: from a few cm to 2.6 meters. We observed the fibers during the polishing process with the microscope with magnification of 5x, 20x, 50x, and 150x. FIG. 3.7 shows the cross-section of a sample with capillary tube and Er doped tellurite fiber inside. The core of the fiber, as we can barely see on the right lower figure, is approximately 3  $\mu\text{m}$ .

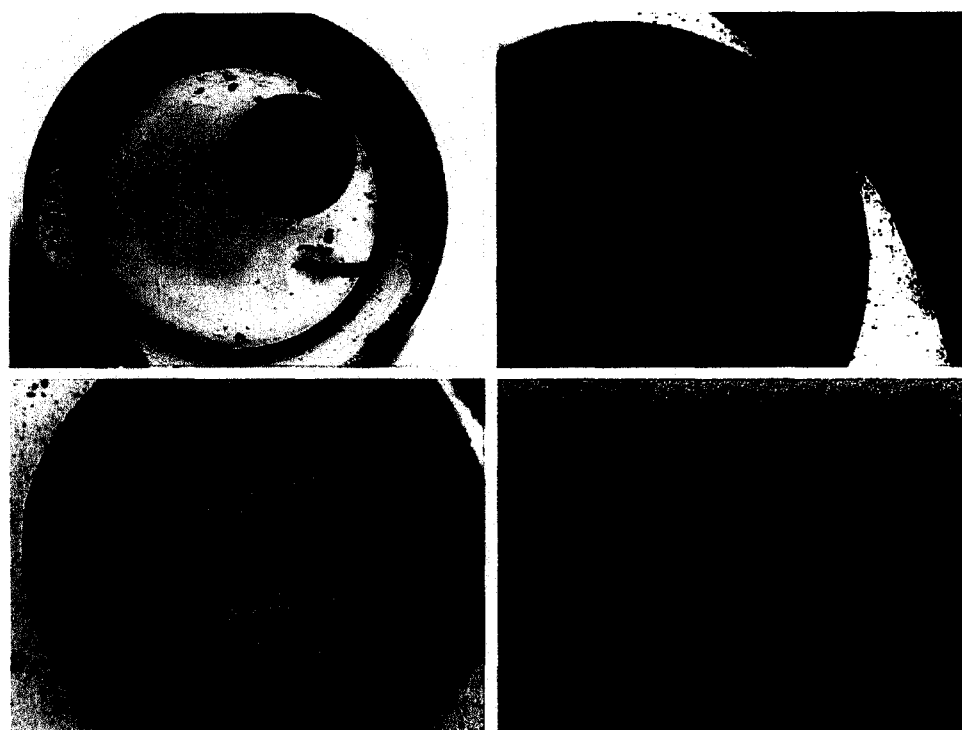


FIG. 3.7 The cross-section of the sample with capillary tube and Er-doped tellurite fiber inside.

Magnification (from upper left to bottom right): 5x, 20x, 50x, and 150x.

### 3.5 High-resolution combined excitation-emission spectroscopy (CEES)

CEES is a site selective technique to study fibers and waveguides at low temperature and its purpose is to identify possible erbium sites in these glasses. We performed temperature dependent measurements on high-resolution CEES, exciting the erbium with a tunable 980 nm laser and detecting the emission in the green, red and 1.5  $\mu\text{m}$  spectral ranges. The temperature was varied from 4K to the room temperature in 20 K steps. The length of the sample was 1 cm.

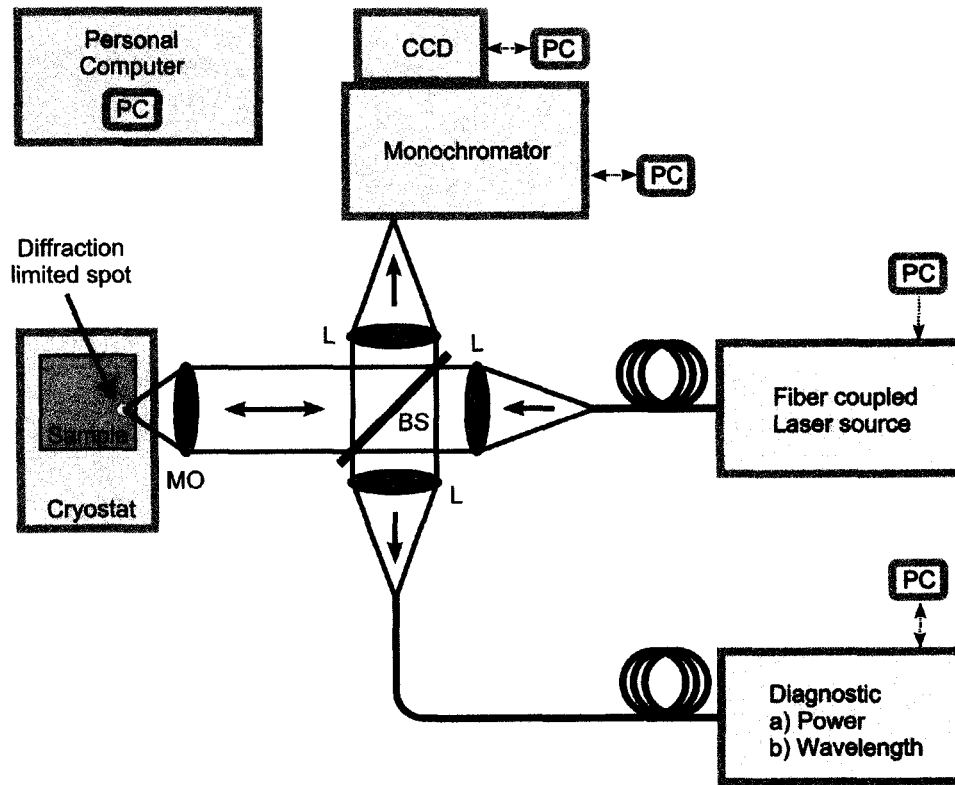


FIG. 3.8 Schematic diagram of high-resolution CEES (courtesy of C. Sandmann).

A schematic diagram of the high-resolution CEES setup is presented in FIG. 3.8. The excitation source was an external cavity laser (ECL) operating at 980 nm. The laser



light was delivered via an optical fiber. The light was out-coupled, collimated and then focused onto the sample using a 20x Mitutoyo near-IR objective. The sample was mounted in a cryostat, which could be cooled down to 4.2 K using liquid helium. The emission follows the same path back as the excitation light until a beamsplitter cube redirects it into a 1.5  $\mu\text{m}$  monochromator. The emission spectra are recorded using a liquid nitrogen cooled CCD array.

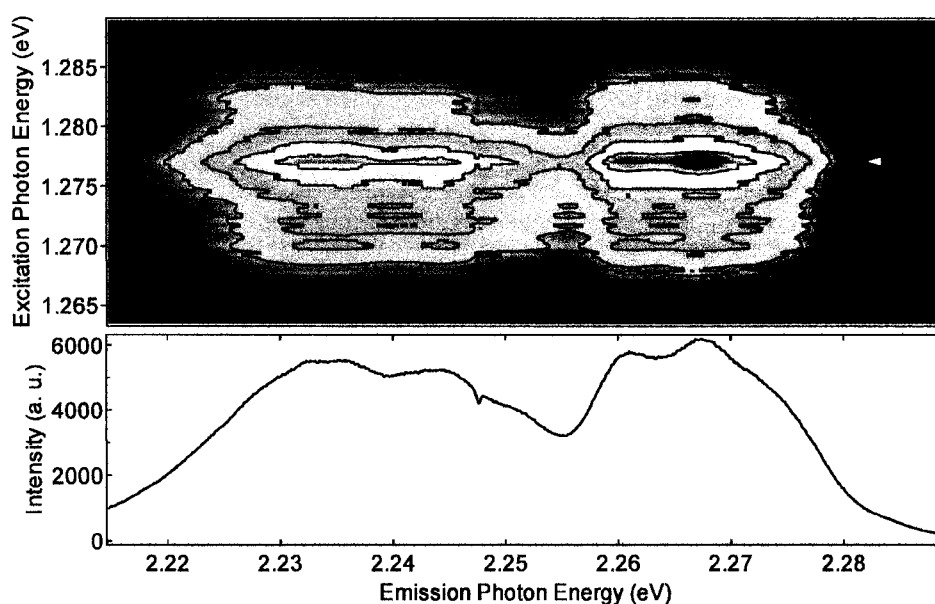


FIG. 3.9 A typical CEES contour spectra (courtesy of C. Sandmann).

Using a 980 nm laser, tunable over 30nm range, we measured many (~400) emission spectra, for different excitation energies. The tunable excitation makes it possible to select erbium ions in different environments. The lower plot shown in FIG. 3.9 is the emission spectrum, for 1.277 eV excitation showing four or five peaks in the contour plot. These peaks correspond to the transitions of erbium in a single site. For a particular excitation around 980 nm (white arrow), we get discrete emission energies

around 1.5  $\mu\text{m}$ , or in the green. Here we present an emission spectrum around 550 nm because it is better resolved than the 1.5  $\mu\text{m}$  one.

### 3.6 Electron-phonon interaction

The interaction between an electron, conceived to be in a particular state described by a wave wavefunction, and a phonon or lattice vibration, described by a phonon eigenstate, can be thoroughly described using Born-Oppenheimer method [Born & Oppenheimer<sup>7</sup>]. Here, we will present just the basic idea. The phonon disturbs the lattice, moving some of the atoms away from their primary symmetry positions. An electron is affected by the change of position, and it is thus liable to be deflected, or scattered, out of its accustomed course. However, the electron can only be scattered if a phonon is emitted or absorbed and the total wave vector not changed except by a reciprocal lattice vector. Thorough description and the solution to the Schrodinger equation of the whole Hamiltonian representing the system of ions and electrons with their interactions could be obtained in the adiabatic approximation is given by Ziman<sup>8</sup>.

## Bibliography

[1] J. W. Lim, H. Jain, J. Toulouse, S. Marjanovic, J. S. Sanghera, R. Miklos and I. D. Aggarwal, *Proceedings of the 16<sup>th</sup> University Conference on Glass Science*, (RPI, Troy, NY, 2003).

- [2] R.L. Wadsack, *An experimental study of the vibronic and electronic resonance Raman effect in semiconductor and garnet crystals*, (PhD dissertation, Yale University, 1971).
- [3] H.A. Szymanski, (ed.), *Raman Spectroscopy, Theory and Practice* (Plenum Press, New York, 1967).
- [4] V. Heine, *Group theory in Quantum Mechanics* (Pergamon Press, New York, 1964), p. 229.
- [5] R. Loudon, *Adv. Phys.* **13** (1964) 423.
- [6] H.M. Moawad, J. Toulouse, H. Jain, A.R. Kortan, Conference preceding, *Proceedings of 103rd Annual Meeting & Exposition of the American Ceramic Society, Symposium on Optoelectronic and Technology in the Information Age* (American Ceramic Society, 2001), p. 45.
- [7] M. Born and J.R. Oppenheimer, *Ann. Phys.* **84** (1927) 457.
- [8] J.M. Ziman, *Electrons and Phonons* (Oxford University Press, Oxford, 1979)

## Chapter 4

### Results

A tellurite glass network is formed with different “molecular units” or building blocks:  $\text{TeO}_4$ ,  $\text{TeO}_3$ ,  $\text{Te}_2\text{O}_5$ , and  $\text{Te}_3\text{O}_8$ , possibly because of the multivalent character of tellurium ions [Sekiya *et al.*<sup>1-3</sup>, Moawad *et al.*<sup>4</sup>, Marjanovic *et al.*<sup>5</sup>]. These different units contribute differently to the properties of the glass, and in particular affect the emission of rare earth dopants. Hence, identifying the units present and their relative fractions as a function of the composition of the glass is essential in order to understand the structure-property relationship in tellurite glasses.

It is well known that alkalis in  $\text{TeO}_2$  glass break Te-O bonds, resulting in the formation of NBO ions. In the process, new molecular units are formed: from  $\text{TeO}_4$  to  $\text{TeO}_{3+1}$  and  $(\text{TeO}_3)^-$ . For very high alkali concentrations, greater than 50%, isolated  $(\text{TeO}_3)^-$  and  $(\text{Te}_2\text{O}_5)^{2-}$  units are also formed and the glass network becomes very weak (very low  $T_g$ ). However, the addition of a second component can promote the appearance of several new units ( $\text{Te}_3\text{O}_8$ ), giving rise to a reconstructed network with a different topology. The results presented below indicate that such a reconstruction is enabled by the introduction of ZnO in  $\text{TeO}_2$  glass, but is facilitated or made possible by the additional structural degrees of freedom resulting from the breaking of Te-O bonds by Na.

Several excellent studies of tellurite glasses have already been published. Most notably, Sekiya and coworkers [Sekiya *et al.*<sup>1-3</sup>, Moawad *et al.*<sup>4</sup>, Marjanovic *et al.*<sup>5</sup>] have investigated a number of binary tellurite glasses, primarily using Raman spectroscopy.

Based on their Raman spectra, more specifically in the higher frequency region, they have identified the different molecular units present in these glasses. However, it is rare that strictly binary glasses be used in practical applications. Indeed, it has been known for some time that tellurite glasses, modified by the addition of ZnO and alkali, possess better optical properties than if either component is added separately [Sekiya *et al.*<sup>1-3</sup>, Moawad *et al.*<sup>4</sup>, Marjanovic *et al.*<sup>5</sup>]. For this reason, we have performed a combined X-ray photoelectron spectroscopy (XPS) and Raman study [Moawad *et al.*<sup>4</sup>] of tellurite glasses with general composition,  $(1-x-y)\text{TeO}_2-x\text{ZnO}-y\text{M}_2\text{O}$ , ( $\text{M} = \text{Li}, \text{Na}, \text{K}$ ). The goal of the study was to understand the combined effect of two additional components in the glass. Recently, we reported the preliminary results of this study [Marjanovic *et al.*<sup>5</sup>]. These suggest that, while the alkali ions break bonds and introduce a certain degree of discontinuity in the  $\text{TeO}_2$  network, Zn by contrast tends to promote the formation of chain-like  $\text{Te}_3\text{O}_8$  units and helps reconstruct the network. Here, we first report the full results of the Raman study, with a quantitative analysis of the spectra and discussion.

## 4.1 Raman spectra

### 4.1.1 Raman effect in zinc-tellurite glasses

The Raman spectra of tellurite glasses are particularly interesting because they exhibit groups of peaks that are characteristic of the various modes of molecular vibrations, which are well separated and easily identifiable. A comparison of the Raman spectra of glasses with different compositions gives information on the influence of substitute ions in tellurite glasses either as modifier or glass formers.

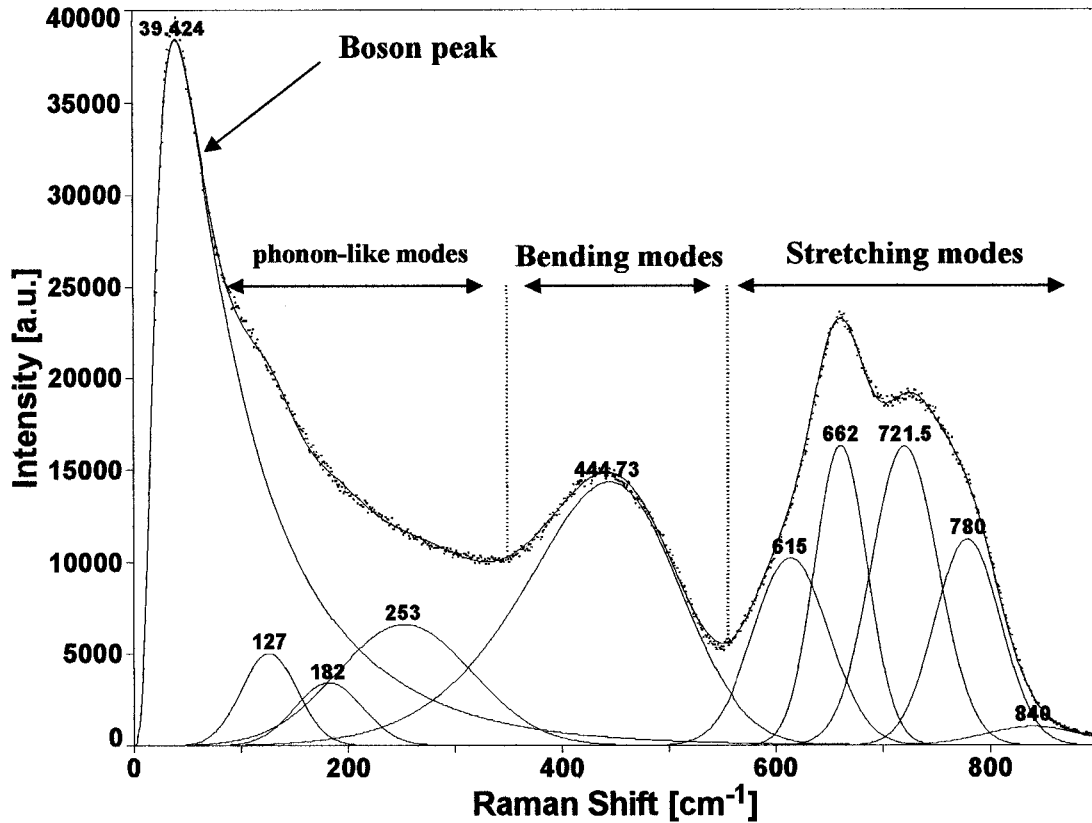


FIG. 4.1. Peak deconvolution of unpolarized Raman spectra of ternary tellurite glasses containing 5% Na<sub>2</sub>O and 15% ZnO, with fitting results, at the room temperature.

A peak deconvolution of the typical unpolarized Raman spectrum of tellurite glasses with 5% Na, 15% Zn and 80%TeO<sub>2</sub>, at room temperature, is presented in FIG. 4.1. Four spectral regions can be identified in TeO<sub>2</sub> glasses. The stretching modes appear at the highest frequencies, here 550-900 cm<sup>-1</sup>. This frequency group can be deconvoluted into four peaks, A at ~780 cm<sup>-1</sup>, B at ~720 cm<sup>-1</sup>, C at ~665 cm<sup>-1</sup> and D at ~615 cm<sup>-1</sup> [Sekiya *et al.*<sup>2,3</sup>, Moawad *et al.*<sup>4</sup>]. The assignment of these peaks has been made based on the normal analysis of  $\alpha$ -form of crystalline paratellurite. High frequency peaks are usually due to simple bond stretching modes. Here, peaks A and B come from the

stretching of a  $\text{Te}_{\text{eq}}\text{O}_{\text{ax}}$  bond. They are assigned to  $\nu_{\text{s2}}\text{TeO}_4$ , symmetric vibrations involving equatorial Te-O bonds (and  $\nu_{\text{s2+as}}\text{TeO}_4$ , simultaneous symmetric vibrations of the same bonds and asymmetric vibrations of axial Te-O bonds) and  $\nu_{\text{s2+as}}\text{TeO}_4$ , respectively. There was some uncertainty about the origin of the B peak (see Chapter 5), but it most likely corresponds to the stretching mode of a distorted Te-O bond, as in  $\text{TeO}_{3+1}$ . These peaks grow when bonds are broken by the addition of dopants. The lower frequency peaks, C and D, come from the stretching vibrations of normal Te-O bonds, with Te and O being bonded as in pure  $\text{TeO}_2$  glass. Both C and D peaks arise from different vibrational modes of the same molecular unit, most likely a  $\text{TeO}_4$  unit since they are both intense in pure  $\text{TeO}_2$  glass. They have been assigned to  $\nu_{\text{s1}}\text{TeO}_4$  and  $\nu_{\text{as}}\text{TeO}_4$ , respectively, as symmetric and asymmetric stretching modes of  $\text{Te}_{\text{eq}}\text{O}_{\text{ax}}\text{-Te}$  bridges, made up of two unequivalent Te-O bonds, one involving equatorial and the other an axial oxygen atom [Moawad *et al.*<sup>4</sup>].

At intermediate frequencies, the E peak ( $\sim 440\text{ cm}^{-1}$ ) is due to bending modes involving  $\text{Te}_{\text{eq}}\text{O}_{\text{ax}}\text{-Te}$  bridges, assign to  $\delta_{\text{s}}\text{TeO}_4$  (and  $\delta_{\text{as}}\text{TeO}_4$ ), and is found to be very strong in glasses with a high concentration of  $\text{TeO}_2$ . Even though the silica and tellurite glasses both  $\text{XO}_4$  units are structurally different, which makes comparison difficult, it is interesting to note that a similar peak in silica glasses at  $440\text{ cm}^{-1}$  has been convincingly attributed to the Si-O-Si bending mode [Sommer *et al.*<sup>6</sup>]. It is also worth noting that this peak is asymmetric (see Chapter 5). In the same way as peak C, peak E disappears upon introduction of glass network modifiers, indicating a loss of Te-O-Te linkages and network connectivity. Similar peaks in paratellurite have also been assigned to the bending of identical axial and equatorial O-Te-O bonds [Sekiya *et al.*<sup>1</sup>, Moawad *et al.*<sup>4</sup>].

The Raman spectra of tellurite glasses also reveal the existence of other modes in the intermediate spectral region, 100-300  $\text{cm}^{-1}$ , like peak F at  $\sim 253 \text{ cm}^{-1}$ , peak G at  $\sim 182 \text{ cm}^{-1}$  and the peak H at  $\sim 127 \text{ cm}^{-1}$ . The peaks at these frequencies change significantly with dopant concentration and have not yet been assigned. However, the intensity of the whole low frequency region (100 – 400  $\text{cm}^{-1}$ ) increases in binary glasses with increasing zinc oxide concentration (see further FIG. 4.3). As it would be explained in detail in Chapter 5, chain-like  $\text{Te}_3\text{O}_8$  units are expected in crystalline zinc-tellurite compounds ( $\text{Zn}_2\text{Te}_3\text{O}_8$ ). Assuming the presence of chains in zinc-tellurite glasses, collective torsional mode would appear at lower frequencies, as opposed to stretching and bending molecular modes at higher frequencies. Torsional peaks would be expected in the low frequency spectral region (and would reveal the number of  $\text{Te}_3\text{O}_8$  units). Alternatively, these peaks could be phonon-like modes or precursors of phonons. The Raman spectrum of zinc oxide [Damen *et al.*<sup>7</sup>] contains a peak at 101  $\text{cm}^{-1}$ . According to our data, in zinc-tellurite glasses, this peak is significantly overtoned by very strong the Boson peak.

The ubiquitous Boson peak appears at the lowest frequencies, where it has been attributed either to molecular rotations or to a combination of acoustic waves and rotations. All the spectra have been normalized to the height of the Boson peak. This procedure is justified by the fact that this peak shows the least changes for different glass compositions and glasses, and by the fact that it is particularly intense in tellurite glasses.

Symmetrical Gaussian functions were used to fit the measured Raman peaks, except for the Boson and the  $E_{440}$  peaks. Both latter peaks have asymmetrical shape and this effect is more pronounced for higher concentrations of Zn. The asymmetry and the



origin in the Boson peak in silica were discussed in more detail by Sommer *et al.*<sup>6</sup>. It was concluded that it is more likely that the Boson peak is due to localized oscillators, with frequency being determined primarily by their force constant and their mass. An expression proposed by Manilovsky & Sokolov<sup>8</sup> was used to describe its asymmetry:

$$I_s(\omega, T) = A \frac{\omega^3}{(\omega^2 + 4\omega_0^2)^2} (n(\omega, T) + 1) \quad (4.1)$$

Here,  $A$  is a constant,  $\omega_0$  is the position of the Boson peak and  $n(\omega, T)$  is the boson occupation number. This proposed theoretical expression is based on the continuum theory of Martin & Brenig<sup>9</sup>.

The asymmetric shape of the E<sub>440</sub> peak can be explained by a distribution of the intermolecular Te-O-Te bond angles. A similar shape of the corresponding peak in silica was conclusively attributed to the distribution of the inter-tetrahedral angles,  $120^\circ \leq \theta \leq 180^\circ$  [McIntosh *et al.*<sup>10</sup>, Sen & Thorpe<sup>11</sup>, Galeener<sup>12</sup>, Mozzi & Warren<sup>13</sup>]. Due to a weaker restoring force for the motion of oxygen in the Te-O-Te linkage, bending vibrations at larger angles can be shown to correspond to lower frequencies.

For comparison of spectra of doped tellurite glasses studied in this thesis with the spectra of pure tellurite glass, we present the evolution of the Raman spectra during the crystallization of TeO<sub>2</sub> glass into the  $\alpha$ -phase (labeled by crosses) and then into the  $\gamma$ -phase (labeled by black circles), shown in FIG. 4.2 [Noguera *et al.*<sup>14</sup>]. At heating pure TeO<sub>2</sub> glass, the  $\gamma$ -TeO<sub>2</sub> lattice begins to develop at about 200 °C so that at 240 °C a spectrum of a bulky crystallized  $\gamma$ -TeO<sub>2</sub> sample is observed (peaks near 421, 682 and 818 cm<sup>-1</sup>). At further heating, the  $\alpha$ -phase appears at about 250 °C (peaks near 392 and 644 cm<sup>-1</sup>). It completely replaces the  $\gamma$ -phase and remains stable up to melting. Note that

the crystallization of  $\text{TeO}_2$  glass necessarily involves the  $\gamma$ -phase as the first step of this process, whereas this is not the case for the crystallization of  $\text{TeO}_2$  liquid: being slowly cooled it transforms directly into the  $\alpha$ - $\text{TeO}_2$  lattice.

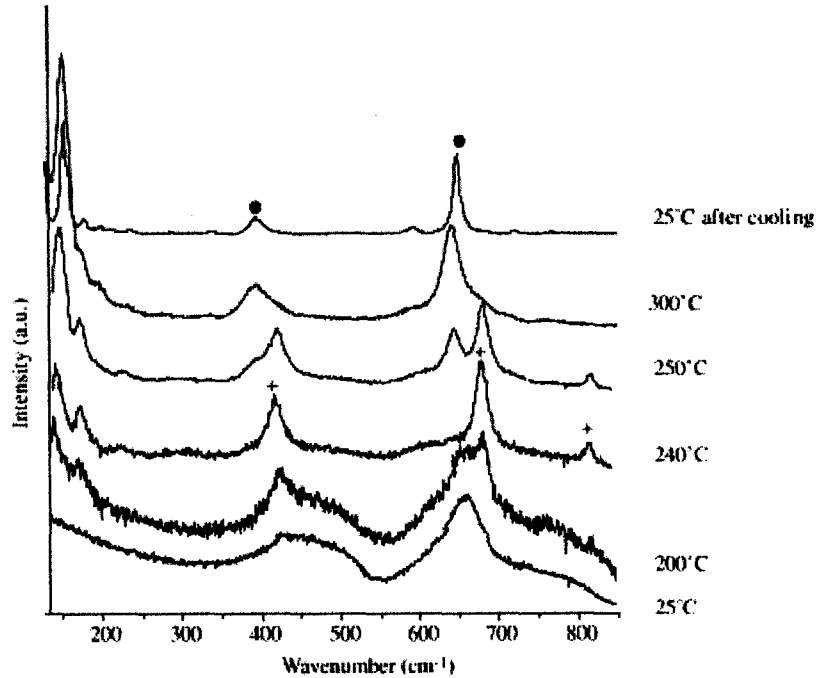


FIG. 4.2 Evolution of the Raman spectra during the crystallization of  $\text{TeO}_2$  glass into the  $\gamma$ -phase (labeled by crosses) and then into the  $\alpha$ -phase (labeled by black circles) [Noguera *et al.*<sup>14</sup>].

To study the combined effect of Na and Zn in tellurite glasses, we monitored changes in the spectra for different compositions. Pure tellurite glass has more intense C and D peaks, while alkali dopants introduce NBO atoms, giving rise to a stronger A peak. We also expect an increase in absolute intensity of intermediate frequency peaks in glasses with better network connectivity.

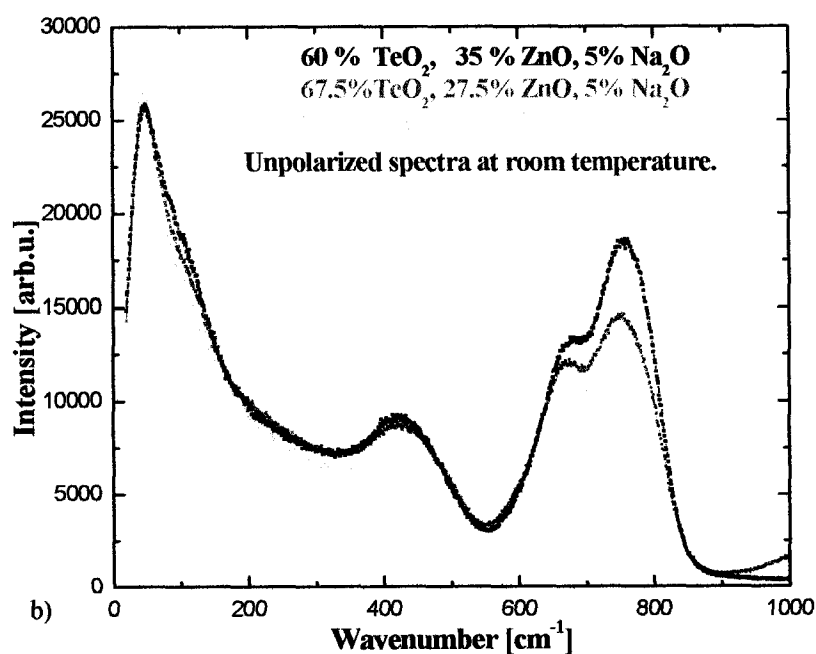
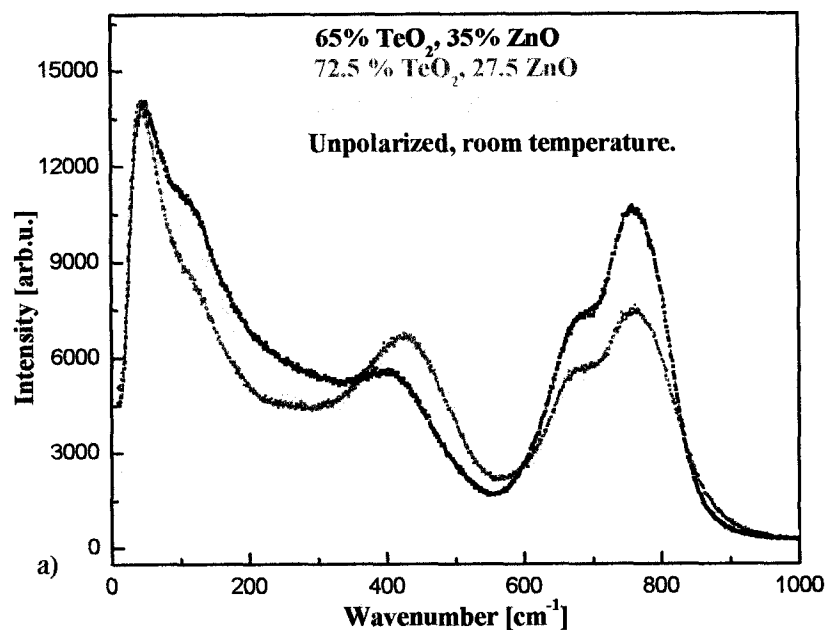


FIG. 4.3 Raman spectra of zinc-tellurite glasses: a) binary, b) with 5% Na<sub>2</sub>O; unpolarized, at room temperature.

Several general trends can be observed, which are detailed later in this section.

From a global examination of the spectra of tellurite glasses from Table 3.1 and partially

shown at FIG. 4.3, it is immediately apparent that, with increasing substitution of Zn for Te, the Raman intensity around  $750\text{ cm}^{-1}$  grows relative to the intensity around  $650\text{ cm}^{-1}$ . Looking at the details of the fit one sees that this growth is primarily due to an increase in the height of peak A relative to that of peak B and to a concurrent decrease in the height of both peaks C and D. Peak B can be seen to remain almost constant with composition and the same can be said of the ratio C/D. This observation indicates that the vibrational mode giving rise to the B peak is not significantly affected by the Zn/Te substitution, at least within the composition range studied and that the C and D peaks both arise from the same molecular unit.

Structural trends can now be identified by studying ratios of the intensities of the individual peaks. In FIGS. 4.4 and 4.5, we present the peak ratios that reflect the relative fractions of the different molecular units present in the glass, as a function of Na concentration, 0%, 5% and 10%. The peak ratio A/C in FIG. 4.4 represents the fraction of  $\text{TeO}_3$  and  $\text{TeO}_{3+1}$  units relative to  $\text{TeO}_4$  units and reflects an increase in the number of NBO atoms in Te-O bonds with increasing concentration of dopants, as expected. FIG. 4.5 shows the peak ratio  $E_{253}/A$  dependence on dopants concentration and represent the relationship between new linkages and appearance of NBO atoms. All figures can be read horizontally and vertically, providing two distinct kinds of information.

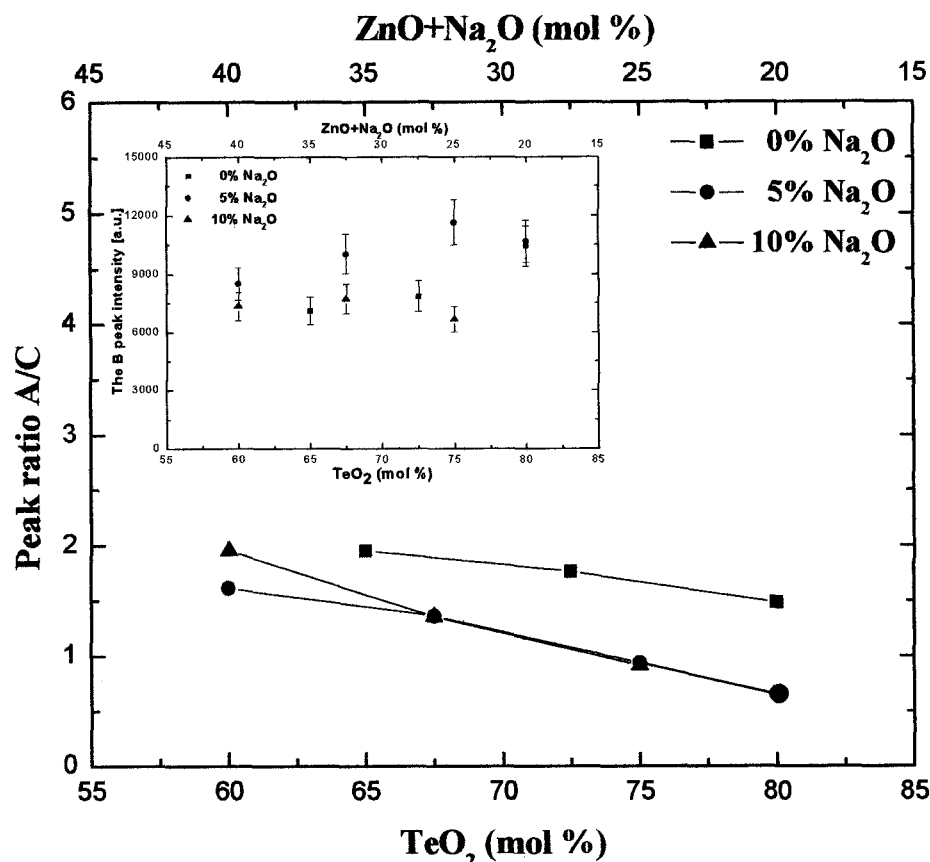


FIG. 4.4 Peak ratio A/C dependence on dopants concentration (lines are drawn through data symbols).

Insert shows the B peak intensity dependence on concentration.

Looking first at FIG. 4.4 from right to left for a constant Na concentration, we see that, for all three Na concentrations, the Zn/Te substitution results in an increase of the A/C ratio. As indicated above, this reflects an increase in the number of NBO atoms suggesting that Zn is responsible for their creation. However, now reading FIG. 4.4 vertically from top to bottom suggests that, for 60% TeO<sub>2</sub>, there are fewer NBO atoms for the 5% Na<sub>2</sub>O – 35% ZnO concentration than for 10% Na<sub>2</sub>O – 30% ZnO. A similar effect is observed for the 80% TeO<sub>2</sub> – 5% Na<sub>2</sub>O – 15% ZnO composition. It appears that, for a particular composition, there are fewer NBO atoms in ternary tellurite glass matrix

than in binary one. The high number of NBO atoms in glasses indicates weakly connected glass network, not suitable for photonics applications; thus, we choose particular ternary glasses as better candidates.

Peak B does not change much for different concentrations, as could be seen in the insert in the same figure. The possible reason for such behavior of the B peak is discussed later. Note, that the 5% Na and 10% Na curves are almost superposed, which suggests that the main difference in the effects of Zn and Na occurs at low levels of substitution. For higher Na content, Na and Zn are equally effective in creating NBO atoms.

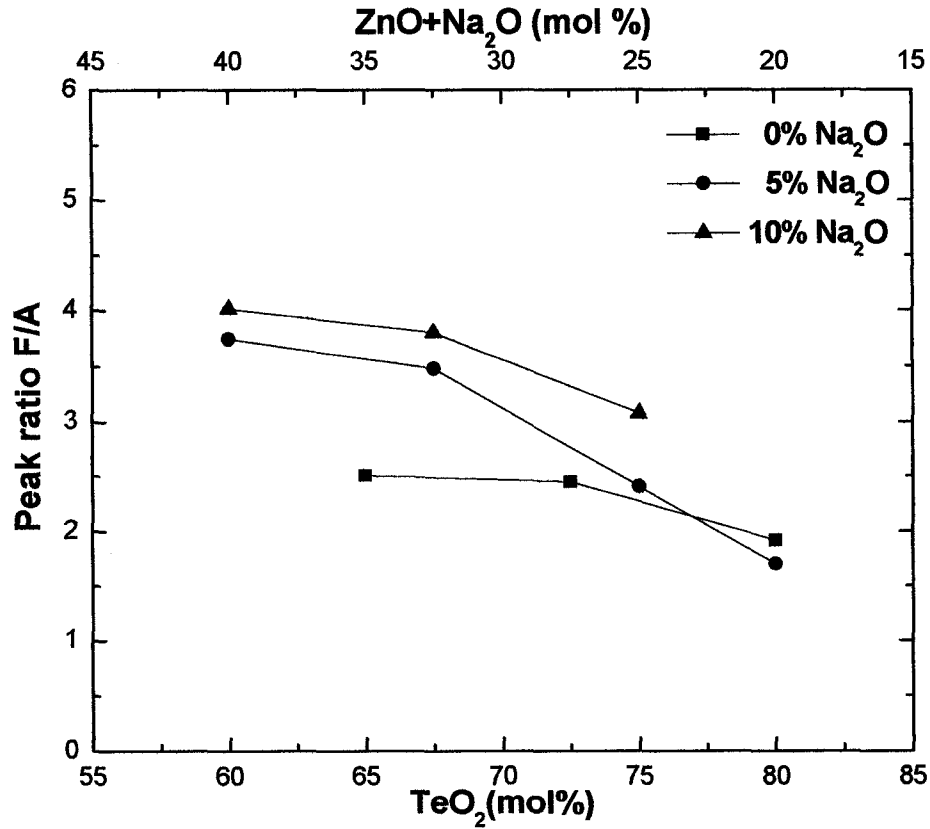


FIG. 4.5 Peak ratio F/A dependence on dopants concentration  
(lines are drawn through data symbols).

From FIG. 4.5, one can immediately notice that the appearance of new linkages in these glasses is related to disappearance of NBO atoms and vice versa. For a constant  $\text{TeO}_2$  concentration, the peak ratio  $F/A$  is higher for higher Zn/Te concentration. Still, sodium is necessary to open up the network, otherwise the ratio of new linkages over NBO atoms is significantly lower (compare again the superposed 5% and 10%  $\text{Na}_2\text{O}$  curves with no sodium).

Such superposed curves as in FIG. 4.4 suggest that an additional increase of  $\text{Na}_2\text{O}$  concentration beyond 5% does not result in significant changes in these ratios. Therefore, the first few mole percents of alkalis appear to make all the difference in the observed spectra and to be decisive in determining the connectivity of the glass. In addition, the introduction of Zn leads to a substantial increase in intensity in the  $100 - 400 \text{ cm}^{-1}$  frequency range. Precursors of phonons or phonon-like modes in this frequency range are desirable for improved erbium emission properties in tellurite glasses, as will be explained in Chapter 5.

#### *4.1.2 Raman spectra of tungsten-tellurite glasses*

Interestingly enough, the first reported Raman study of tellurite glasses seems to have been for a tungsten-tellurite glass,  $85\text{TeO}_2 \cdot 15\text{WO}_3$  [Bobovich & Yakhind<sup>15</sup>]. The basic structural units of these glasses are mainly  $\text{TeO}_4$  trigonal bipyramids and clusters composed of corner-shared  $\text{WO}_6$  octahedra and  $\text{WO}_4$  tetrahedra [Sekiya *et al.*<sup>16</sup>, Kozhukharov *et al.*<sup>17</sup>]. Presented on FIG. 4.6 is a model for  $\text{WO}_3$ - $\text{TeO}_2$  glasses proposed by Kozhukharov *et al.*<sup>17</sup>. Both  $\text{WO}_3$  and  $\text{TeO}_2$  are intermediate glass formers, but since

they are not isostructural, their combination produces a more complex glass network than in conventional tellurite glasses [Sekiya *et al.*<sup>1,16</sup>]. Here we show how additional alkali dopants modify the  $\text{WO}_3\text{-TeO}_2$  glass structure, and offer even greater advantages for optical applications.

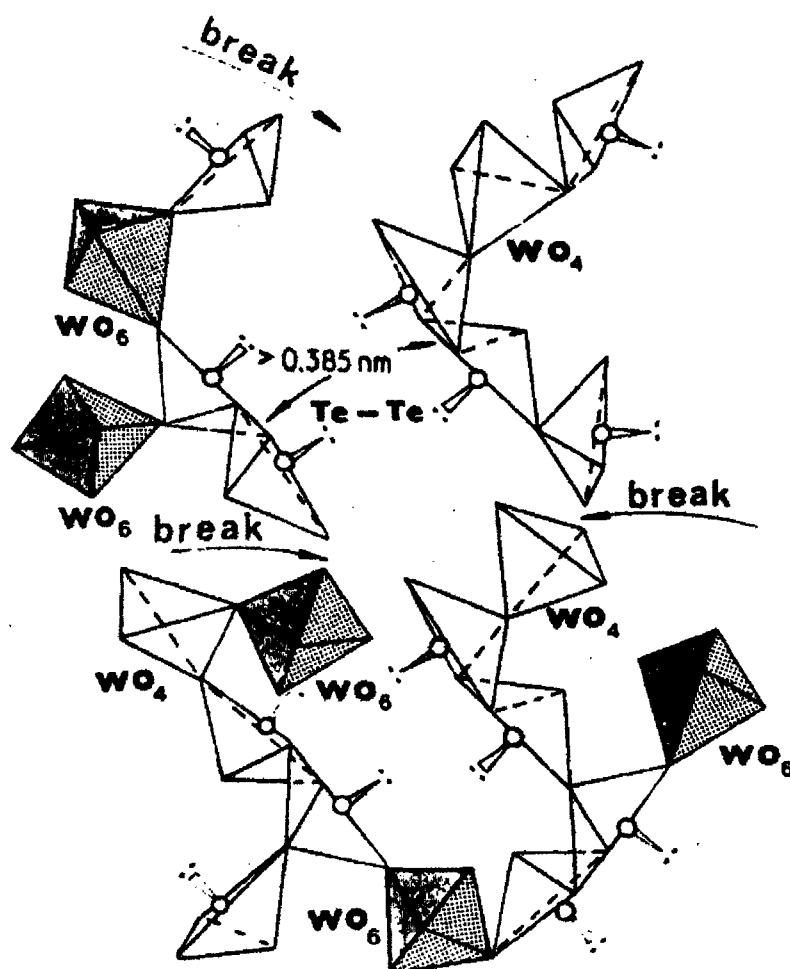


FIG. 4.6 A model for  $\text{WO}_3\text{-TeO}_2$  glasses proposed by Kozhukharov *et al.*<sup>17</sup>.

FIG. 4.7 shows the comparison of the unpolarized Raman spectrum of zinc-tellurite glasses with also unpolarized Raman spectrum of tungsten-tellurite glasses, with



the same percentage of  $\text{TeO}_2$ . As mentioned above, the high frequency region exhibits the stretching modes, the intermediate one the bending modes and the low frequency region mainly the phonon-like modes or precursors of phonons. All spectra were measured at room temperature and were again normalized to the height of the Boson peak.

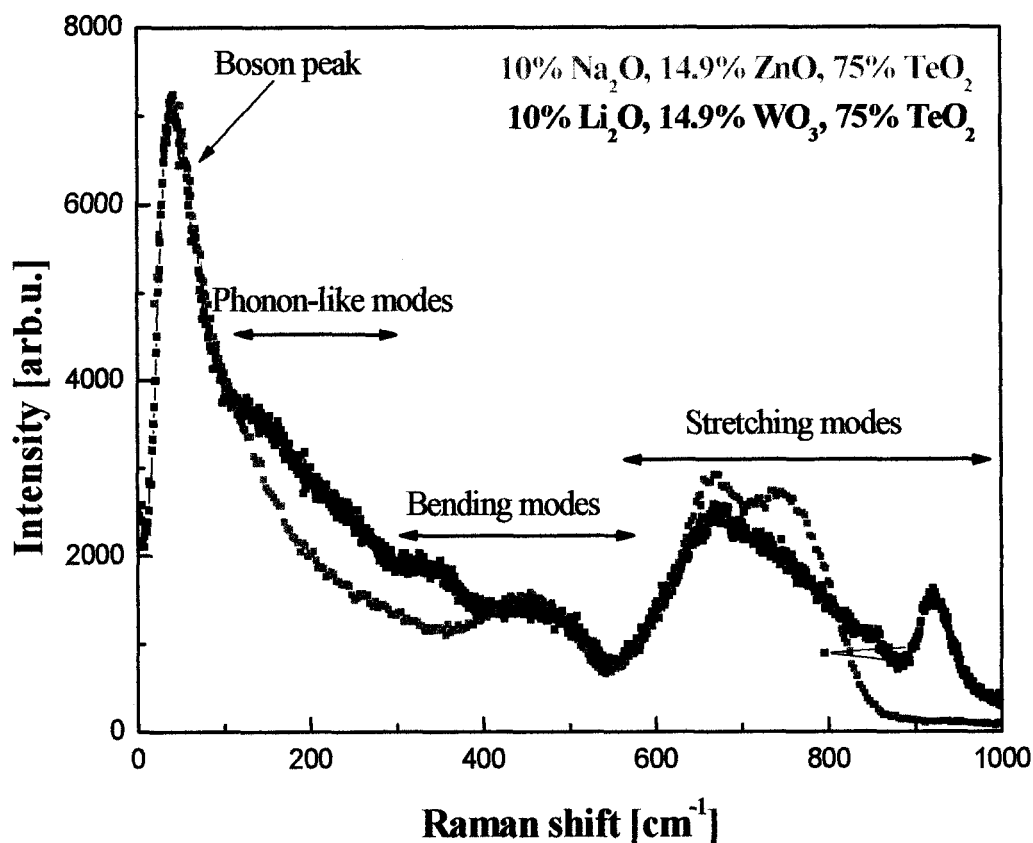


FIG. 4.7 The comparison of the unpolarized Raman spectra of sodium-zinc-tellurite with tungsten-tellurite glasses.

The results of the peak deconvolution of a Raman spectra of  $5.0\text{Li}_2\text{O} \cdot 24.9\text{WO}_3 \cdot 70\text{TeO}_2$  glass, at room temperature, are shown as an example in FIG 4.8. The dependence of the frequency shifts of the deconvoluted peaks on the glass composition was small and the maximal shift was about  $20 \text{ cm}^{-1}$  for the peak at about

475  $\text{cm}^{-1}$ . Symmetrical Gaussian functions were used to fit the measured Raman peaks; however, not all of the peaks have a symmetrical shape. The E peak at  $\sim 475 \text{ cm}^{-1}$  and the Boson peak have asymmetrical shape, as described previously in the case of zinc-tellurite glass. This asymmetry shows a peak tail at lower frequencies, which comes from inhomogeneous broadening due to angular spread of the Te-O-Te bond. Naturally, this peak is very strong in glasses with a high concentration of  $\text{TeO}_2$ . This effect is more pronounced for higher concentration of Li suggesting a broader distribution of bending angles in  $\text{Li}_2\text{O} - \text{WO}_3 - \text{TeO}_2$  glasses.

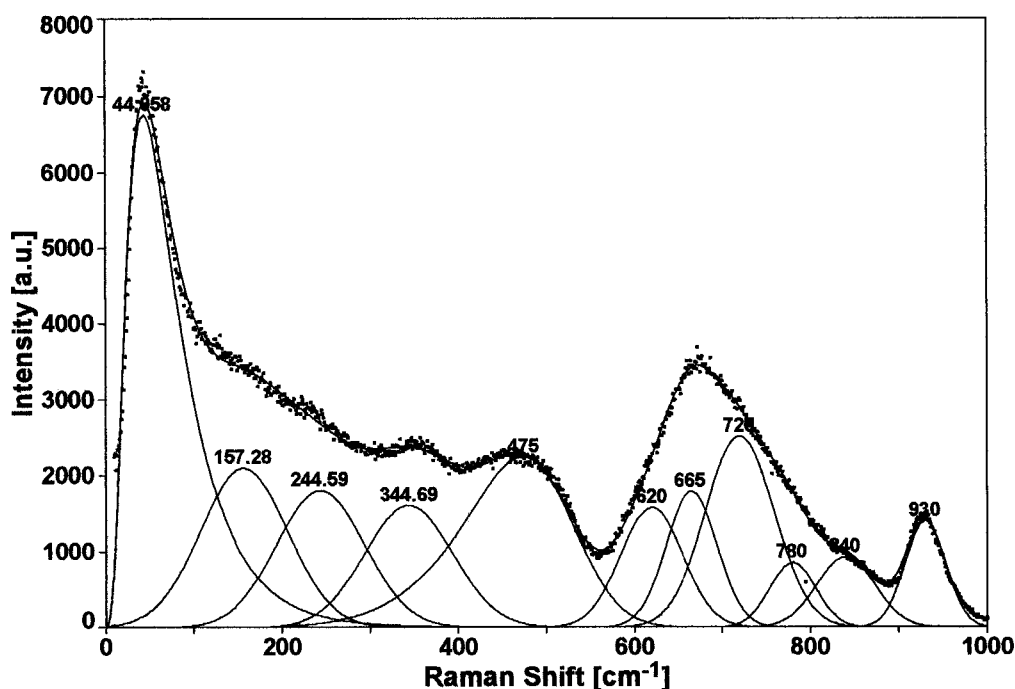


FIG. 4.8 Peak deconvolution of unpolarized Raman spectra of  
 $5.0\text{Li}_2\text{O} \cdot 24.9\text{WO}_3 \cdot 70\text{TeO}_2$ , at room temperature.

New peaks appear in tungsten-tellurite glasses compared with zinc-tellurite ones. A sharp peak is observed at about  $925 \text{ cm}^{-1}$  and another peak at  $840 \text{ cm}^{-1}$ , usually

assigned as peak Z and Y in the literature. Their intensity increases with  $\text{WO}_3$  content and they apparently arise from coordination polyhedra of  $\text{W}^{6+}$ . On the basis of investigation of Raman spectra of crystals containing this ion, the wave number position of peak Z at  $925\text{ cm}^{-1}$ , which represents the maximal phonon energy of tungsten-tellurite glass, corresponds to stretching vibrations of  $\text{W}=\text{O}$  and  $\text{W}-\text{O}^-$  in  $\text{WO}_4$  tetrahedra. Sekiya and coworkers [Sekiya *et al.*<sup>16</sup>] assigned peak Z to the stretching vibrations of  $\text{W}=\text{O}$  bonds, because no  $\text{W}-\text{O}^-$  bonds can be formed in these glasses. They suggested that the radius ratio of  $\text{W}^{6+}$  to  $\text{O}^{2-}$  indicates that  $\text{W}^{6+}$  prefers six-coordination with a stable framework composed of corner-shared  $\text{WO}_6$  octahedra. Based on crystal chemistry, they also concluded that, in  $\text{WO}_3\text{-TeO}_2$  glasses,  $\text{W}^{6+}$  having  $\text{W}=\text{O}$  bonds is not four- but six-coordinated. In order to increase the local electrostatic stability of the tungsten ion having a double-covalent bond, some of the remaining vertices of the  $\text{WO}_6$  octahedra having a  $\text{W}=\text{O}$  bond are assumed to be shared with  $\text{TeO}_{3+1}$  polyhedra forming  $\text{Te}_{\text{-short(ax)}}\text{O}-\text{W}$  linkages.

There are two possible assignments for the  $840\text{ cm}^{-1}$  peak. One is to stretching vibrations of  $\text{W}-\text{O}$  bonds associated with  $\text{WO}_6$  octahedra having  $\text{W}=\text{O}$  bonds, because peak Y has a frequency similar to that of the peak at  $857\text{ cm}^{-1}$  observed in the spectrum of the  $\text{W}_2\text{O}_3(\text{PO}_4)_2$  crystal. The other is to antisymmetric stretching vibrations of  $\text{WO}_4$  tetrahedra having  $\text{W}=\text{O}$  bonds, because the same vibrational mode is observed in the spectra of  $\text{K}_2\text{WO}_4$  crystals [Sekiya *et al.*<sup>16</sup>, Caillet & Saumagne<sup>18</sup>].

Other peaks are present at about 620, 665, 720, and  $780\text{ cm}^{-1}$ . The assignment of these peaks has been made based on corresponding peaks observed in the spectrum of conventional tellurite glass. Five peaks were observed in the same wave number region of

the spectrum of pure tellurite glasses at about 450, 611, 659, 716, and 773  $\text{cm}^{-1}$  [Sekiya *et al.*<sup>1-3</sup>, Moawad *et al.*<sup>4</sup>, Marjanovic *et al.*<sup>5</sup>]. A peak at about 345  $\text{cm}^{-1}$  is also present in all the  $\text{WO}_3$ - $\text{TeO}_2$  glasses used in this study. It is interesting to note that peak at about 620  $\text{cm}^{-1}$  can serve as a reference, since its intensity is not strongly affected by a change of dopants concentration.

The most interesting part of the spectrum and the major difference between zinc-tellurite and tungsten-tellurite spectra is observed in the low frequency region, from 100 to 400  $\text{cm}^{-1}$ . Peaks in this region have not yet been assigned; they may belong to torsional or phonon-like modes of the glass network. As we explain later in Chapter 5, these phonons may play a decisive role in explaining the broad erbium emission in these glasses. For a constant lithium concentration, significant changes are only observed at low frequency and that is happening when the concentration of tungsten oxide increases at the expense of tellurite oxide, suggesting that this spectral region corresponds directly to tungsten.

FIG. 4.9 shows unpolarized Raman spectra of tungsten-tellurite glasses, with constant concentration of lithium, at the room temperature. The peak deconvolution of the Raman spectra of binary  $\text{WO}_3$ - $\text{TeO}_2$  glasses was reported previously [Sekiya *et al.*<sup>16</sup>]. From the spectra of the glasses in Table 3.2 and FIG. 4.9, we see that with increasing the  $\text{WO}_3$  content, the intensity of the peak at about 345  $\text{cm}^{-1}$  increase. The increase of the 345  $\text{cm}^{-1}$  peak indicates the appearance of W-O-W linkages, as reported in several  $\text{WO}_3$  crystal spectra [Daniel *et al.*<sup>19</sup>, Becher<sup>20</sup>]. Simultaneously, the same figure shows a reduction in the number of Te-O-Te linkages with decreasing tellurite concentration. The  $\text{TeO}_2 \rightarrow \text{WO}_3$  substitution actually represents a substitution of  $\text{TeO}_4$  tetrahedra by  $\text{WO}_4$

[Shaltout *et al.*<sup>21</sup>]. Tungsten forms sub-network within the existing tellurite network, making the glass network better connected and more compact (glass molar volume increases with  $\text{TeO}_2 \rightarrow \text{WO}_3$  substitution – see Table 2.2). This is confirmed by the unpolarized Raman spectra of tungsten-tellurite glasses, with constant concentration of tungsten, at room temperature. FIG. 4.10 shows that the spectra are unchanged in the low frequency region up to  $345 \text{ cm}^{-1}$ , when lithium changes from 5% to 10%  $\text{Li}_2\text{O}$ . The main differences there are in the bending and the stretching modes.

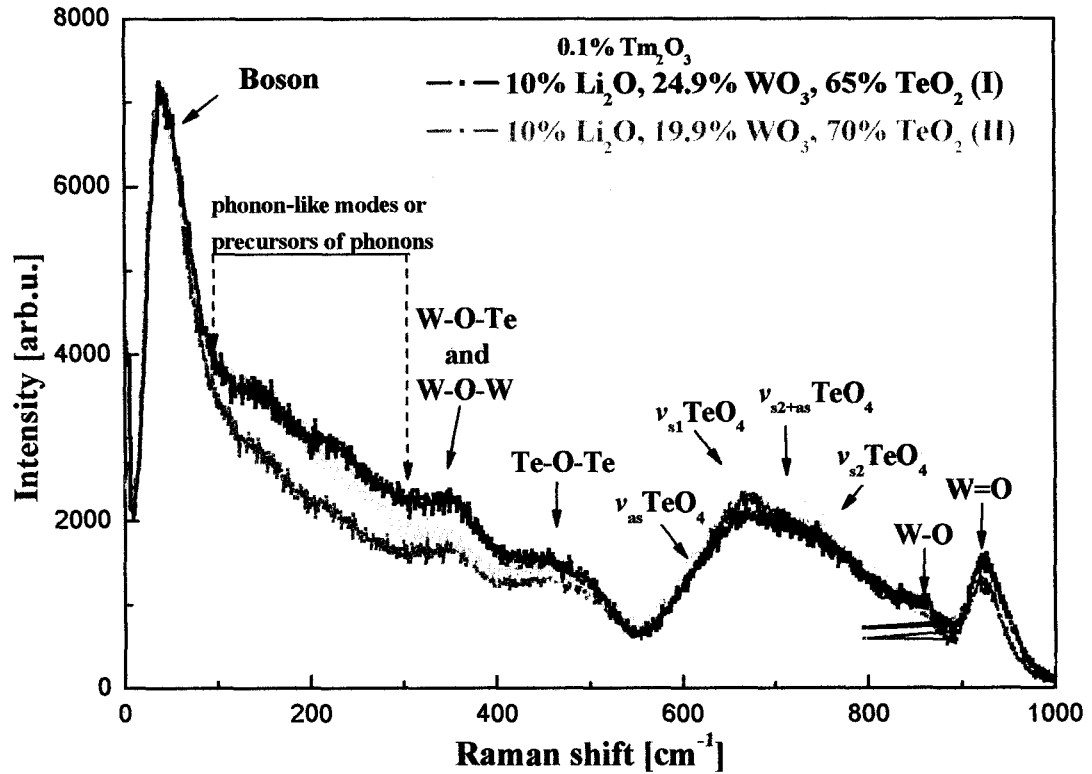


FIG. 4.9 Unpolarized Raman spectra of tungsten-tellurite glasses with constant concentration of lithium, at the room temperature.

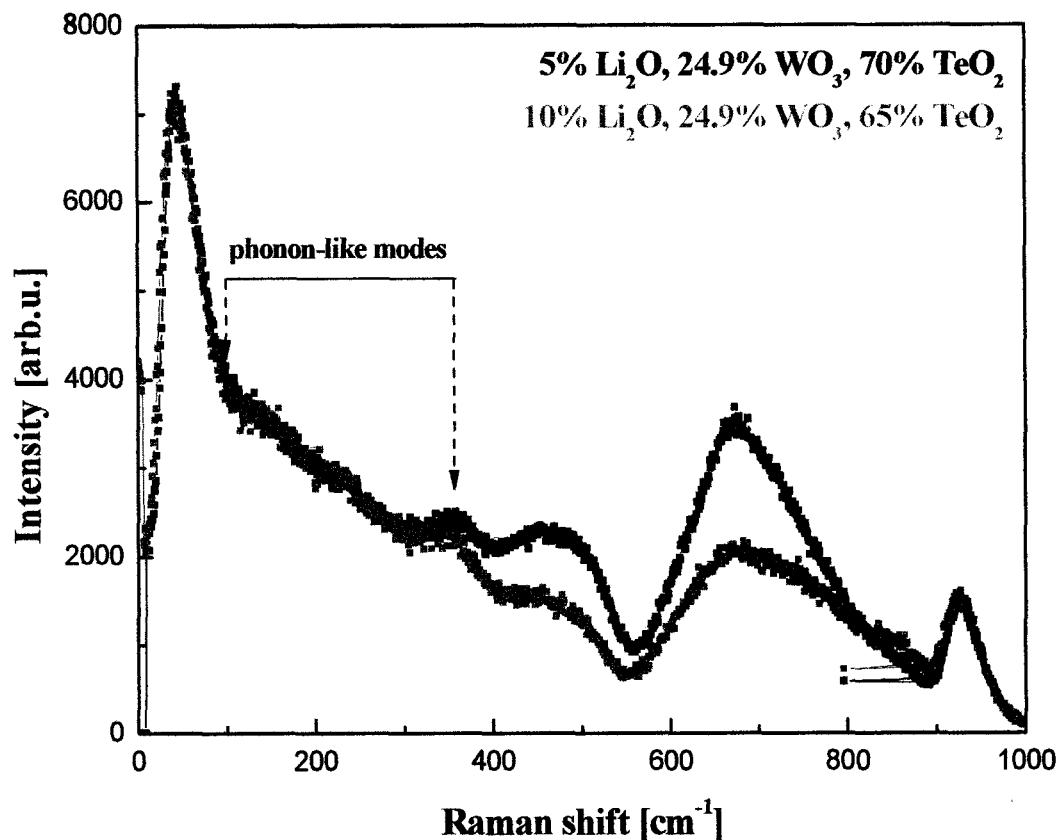


FIG. 4.10 Unpolarized Raman spectra of tungsten-tellurite glasses with constant concentration of tungsten, at the room temperature.

Accordingly, for 25%  $\text{WO}_3$ ,  $\text{Li}^+$  as a modifier affects mainly the Te-O-Te network. For 10%  $\text{Li}_2\text{O}$ , the peak at  $\sim 475 \text{ cm}^{-1}$  decreases and the relative intensity between 660 and  $780 \text{ cm}^{-1}$  peaks decreases. According to this, the lithium ions clearly break the tellurite network bonds. This is expected since the introduction of alkali dopants showed similar effect toward Te-O-Te bridges in zinc-tellurite glass. For 5%  $\text{Li}_2\text{O}$ , the intensity of the peaks related to Te-O-Te, W-O-W, and W-O-Te linkages are not affected and glass network does not appear to be modified significantly when compared to compositions without lithium.

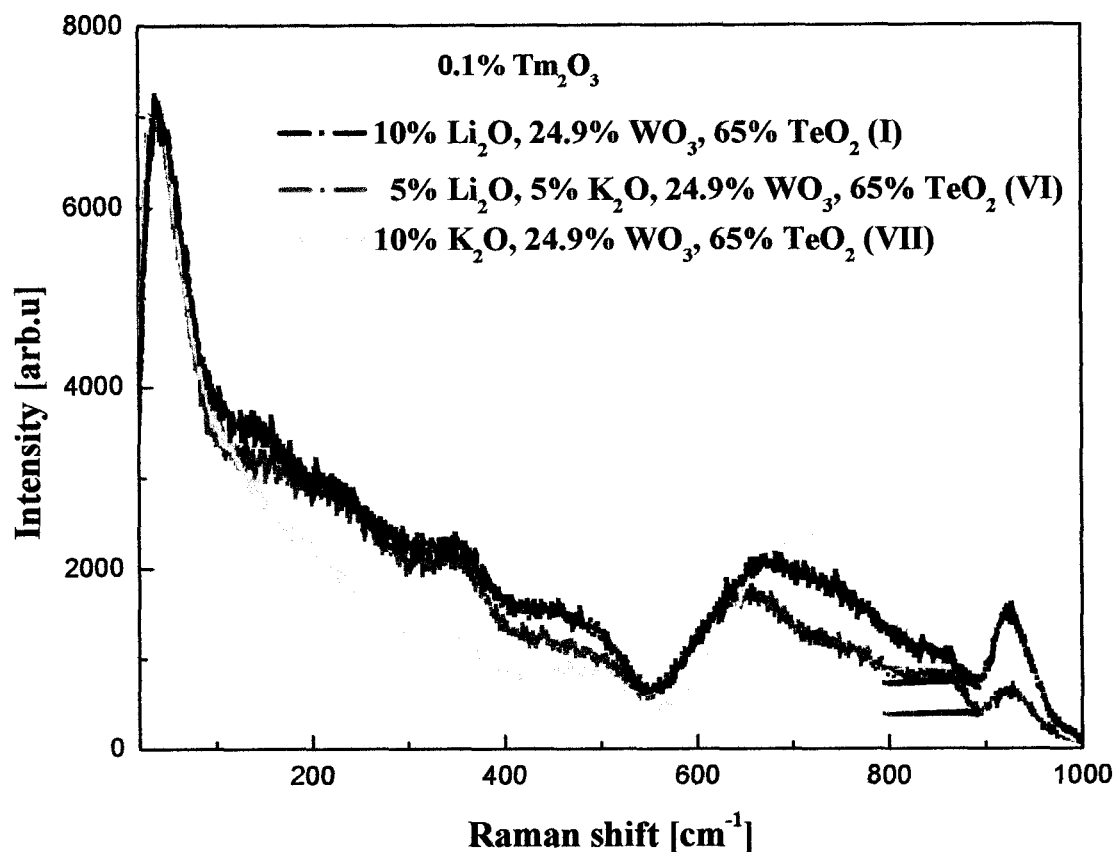


FIG. 4.11 Unpolarized Raman spectra of tungsten-tellurite glasses with Li → K substitution, at the room temperature.

FIG. 4.11 shows unpolarized Raman spectra of tungsten-tellurite glasses with Li → K substitution, at room temperature. As do other alkalis, potassium reduces the number of Te-O-Te and W-O-W linkages. Since K<sup>+</sup> has a much bigger ionic radius than Li<sup>+</sup>, this effect is much stronger in case of potassium. For 5% K<sub>2</sub>O – 5% Li<sub>2</sub>O, the numbers of linkages also decrease, but the tellurite network appears to be more affected since intensity of the peak at 475 cm<sup>-1</sup>, representing Te-O-Te linkages, significantly decreases. This is probably due to different volume affect (and some charge effect), when both alkalis are present in the glass. It is interesting that the 925 cm<sup>-1</sup> peak is stronger in

glasses with 10%  $K_2O$  or 10%  $Li_2O$  than in a glass containing 5% of each, which is probably due to a greater number of  $W=O$  bonds in the former. Alkali-tungsten crystals with high alkali concentration, such as  $K_2WO_4$  and  $Li_2W_2O_7$  (with dominant  $WO_4$  tetrahedral structure), have bigger number of  $W=O$  bonds than crystals like  $K_2W_4O_{13}$  and  $Li_2W_4O_{13}$  (with dominant  $WO_6$  octahedral structure), where the number of  $W-O$  bonds prevails, giving rise to the peak at  $840\text{ cm}^{-1}$ . Analogically, tungsten-tellurite glass with higher potassium and lithium concentration, with more  $WO_4$  tetrahedra, will favor double covalent  $W=O$  over single covalent  $W-O$  bonds.

#### 4.2 An increase of glass transition temperature with $WO_3$

The differential thermal analysis of (a)  $10Li_2O \cdot xWO_3 \cdot (90-x)TeO_2$  and (b)  $xK_2O \cdot (10-x)Li_2O \cdot 25WO_3 \cdot 65TeO_2$  glasses was conducted to determine the glass transition temperature ( $T_g$ ). The results for  $10Li_2O \cdot xWO_3 \cdot (90-x)TeO_2$  show that  $T_g$  increases monotonically with increasing  $WO_3$  concentration (FIG. 4.12) [Lim *et al.*<sup>22</sup>]. It increases from  $283\text{ }^\circ\text{C}$  for a glass containing 5 mol%  $WO_3$  up to  $335\text{ }^\circ\text{C}$  when the concentration of  $WO_3$  is 25 mol%. The glass structure consists of continuous network mainly of  $TeO_4$  trigonal bipyramids (tbp) at low percentages (%) of  $WO_3$ . The increase of  $T_g$  is due to the formation of  $W-O-Te$  linkages with increasing in  $WO_3$  content [Sekiya *et al.*<sup>16</sup>].



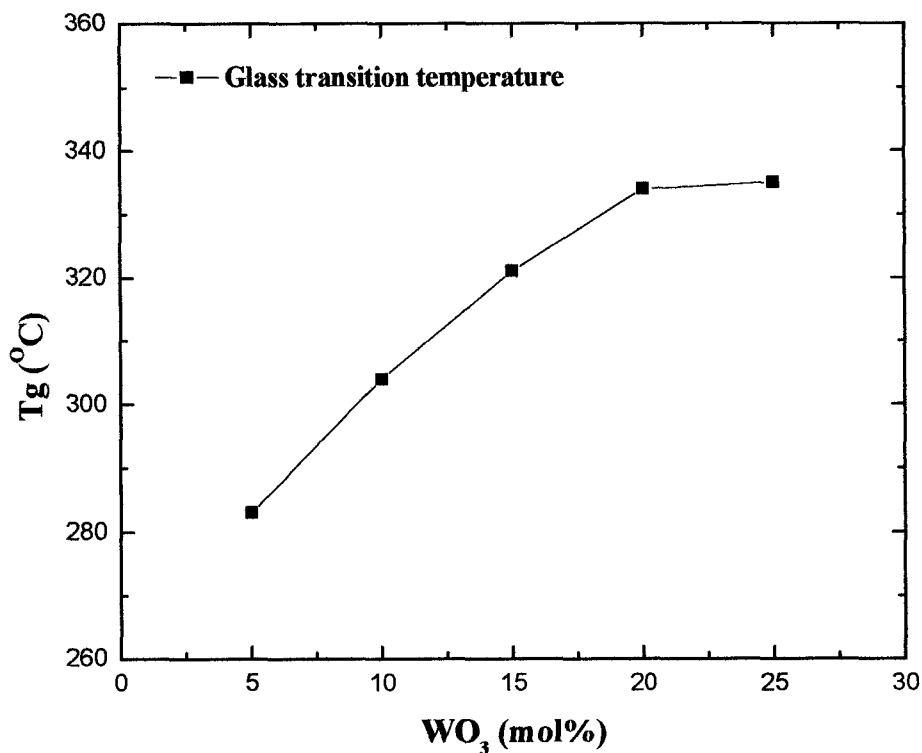
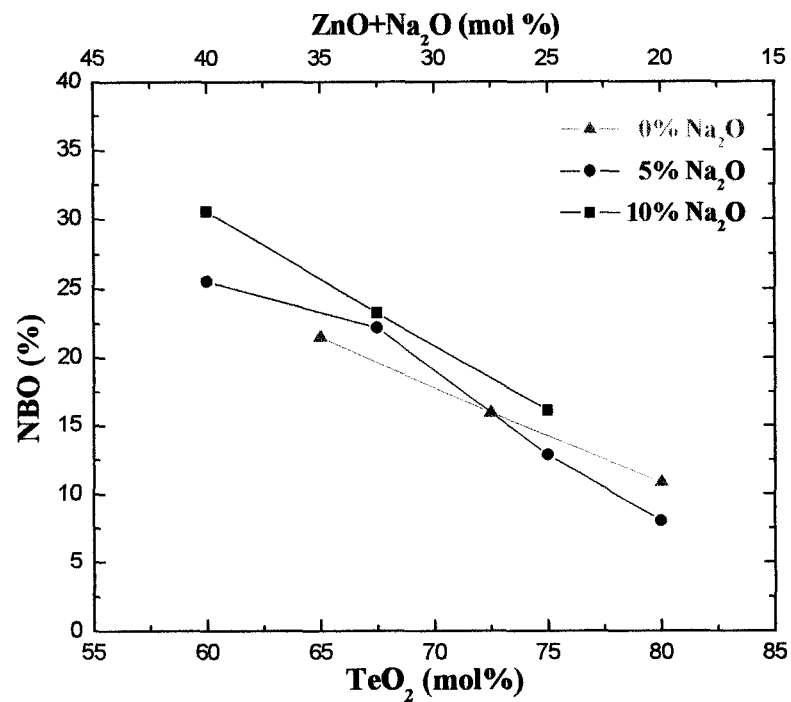


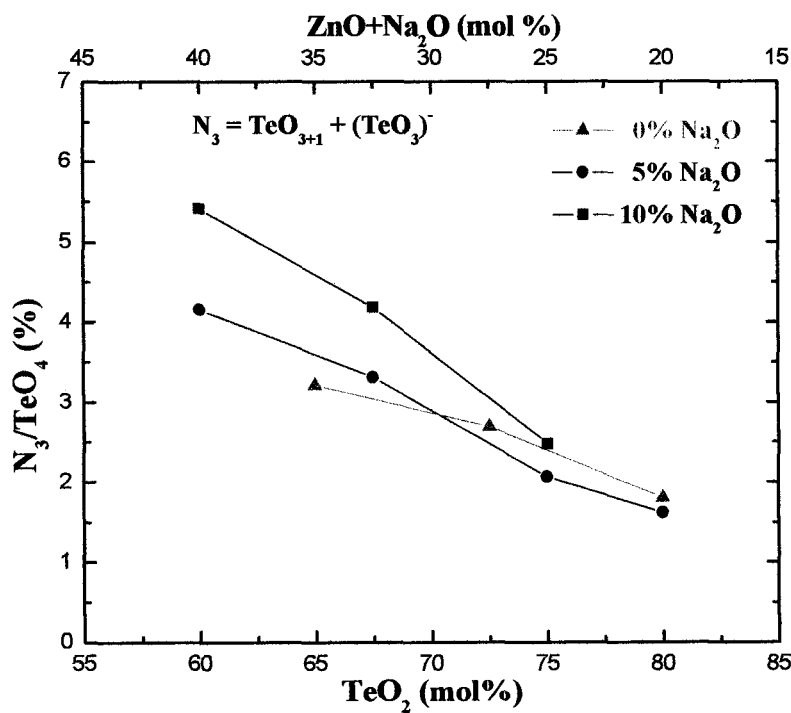
FIG. 4.12 Glass transition temperature of  $10\text{Li}_2\text{O} \cdot x\text{WO}_3 \cdot (90-x)\text{TeO}_2$  glasses  
(with 0.1 wt%  $\text{Tm}_2\text{O}_3$ ) [Lim *et al.*<sup>22</sup>].

### 4.3 XPS data

As mentioned in the previous chapter, XPS results are used in the present study only as supporting evidence. FIG. 4.13 (a) and (b) show the fractions of NBO atoms and of the different Te units as a function of the  $\text{TeO}_2$  concentration [Marjanovic *et al.*<sup>5</sup>]. Increasing  $\text{ZnO}$  and  $\text{Na}_2\text{O}$  results in a corresponding increase of NBO atoms and  $\text{TeO}_{3+1}$  and  $\text{TeO}_3$  units ( $\text{N}_3$ ), especially for smaller concentrations of  $\text{TeO}_2$ . The most interesting observation is the decrease in the number of NBO atoms and  $\text{N}_3$  in ternary glasses below their fractions in binary glasses, as confirmed by Raman data (see in particular the curve for 5%  $\text{Na}_2\text{O}$ ).



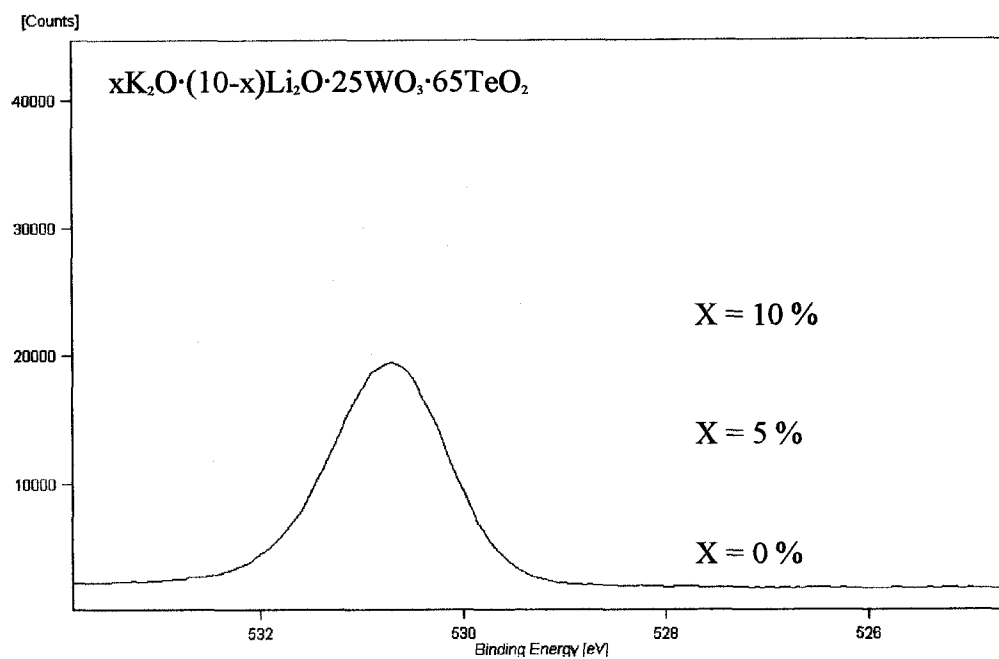
a)



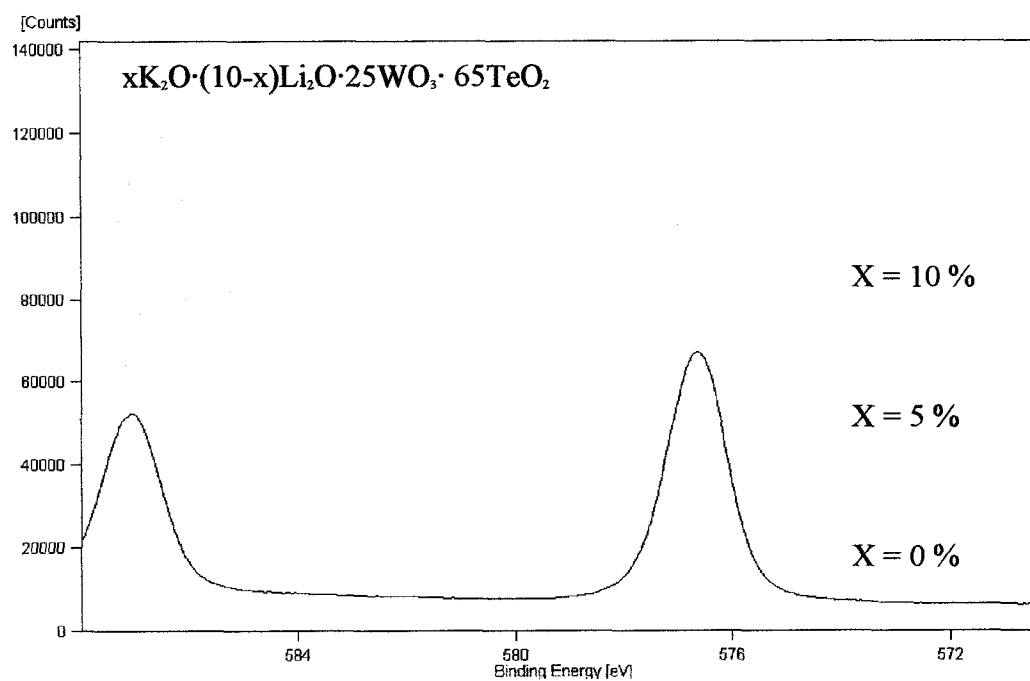
b)

FIG. 4.13 Dependence on  $\text{TeO}_2$  concentration of: a) NBO and b)  $N_3$

(lines are drawn through data symbols).



(a)



(b)

FIG. 4.14 a) O-1s XPS spectra, b) Te-3d XPS spectra of  $x\text{K}_2\text{O} \cdot (10-x)\text{Li}_2\text{O} \cdot 25\text{WO}_3 \cdot 65\text{TeO}_2$  glass system [Lim *et al.*<sup>22</sup>].

The mixed alkali glass  $x\text{K}_2\text{O} \cdot (10-x)\text{Li}_2\text{O} \cdot 25\text{WO}_3 \cdot 65\text{TeO}_2$ , was also measured. Its O-1s and Te-3d XPS spectra are shown in FIG. 4.14 (a) and (b), respectively [Lim *et al.*<sup>22</sup>]. The O-1s and Te-3d<sub>5/2</sub> peaks shift toward smaller binding energy with increasing ionic radius of the alkali ions. Each peak is symmetrical and there is no shoulder on the binding energy side of the main peak. However, there is no shape difference when alkali is mixed. The chemical shift is due to the change in the electronic density of the atoms. It is interesting that this shift is stronger in the glass with 5% of each alkali oxides than in glasses containing 10% K<sub>2</sub>O or 10 % Li<sub>2</sub>O. Similarly, we discussed earlier that Raman peak at 925 cm<sup>-1</sup> is weaker when both alkalis are present.

#### 4.4 Er<sup>3+</sup> emission

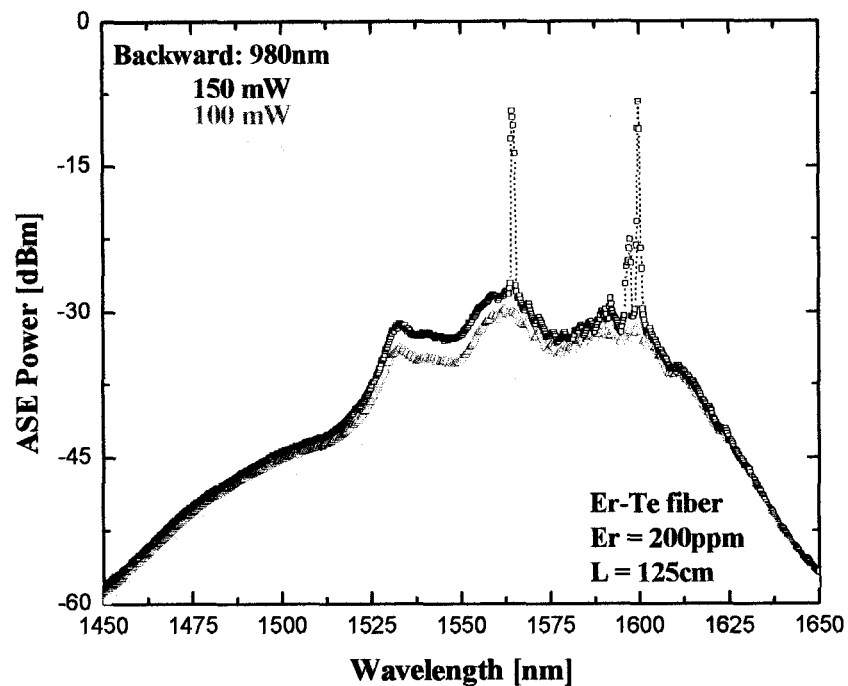
The 980 and 1480 nm pumping band are mainly used for practical EDFA, because they offer good pump efficiency and high-output power characteristics. With 1480 nm pumping, which uses the upper portion of the <sup>4</sup>I<sub>13/2</sub> band, the Er<sup>3+</sup> ions are decayed by intraband nonradiative transitions and used for 1.5 μm-band amplification, where they operate as a quasi-three-level system. The 980 nm pump wavelength yields higher gains than the 1480 nm pump at high powers, because 980 nm achieves a higher inversion than 1480 nm [Becker *et al.*<sup>23</sup>]. Even at high powers, there is incomplete inversion for 1480 nm pumping due to the nonzero spontaneous emission cross section at 1480 nm that drains population out of the upper state.

In our experiments, we used bidirectional-pumping scheme, where the pump power is launched into both ends of the erbium doped fiber. The gain is bigger for a

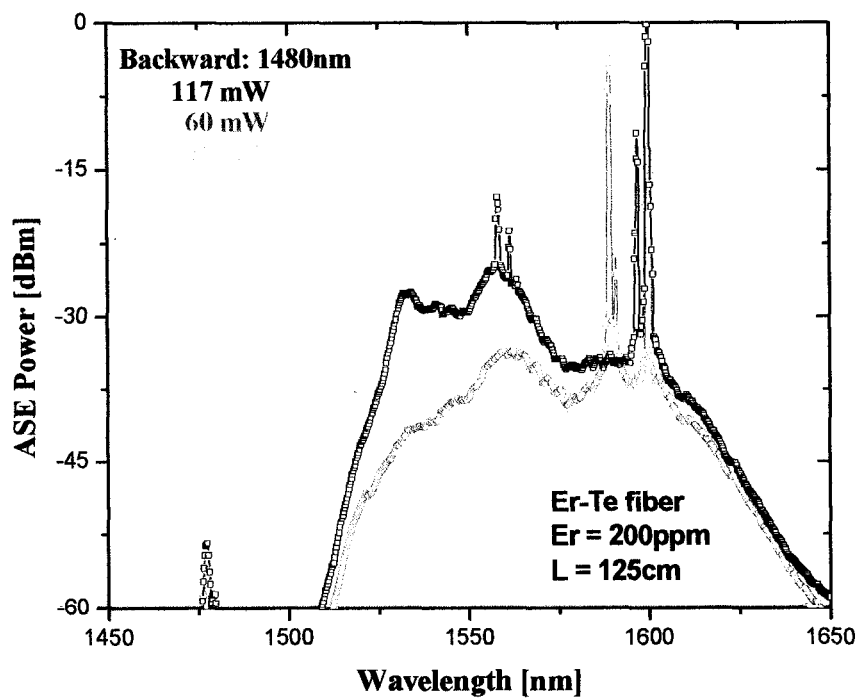
bidirectionally pumped fiber than for a forward-pumped one because of a higher slope efficiency (more than double), but also because bidirectional pumping can suppress the degradation of the metastable level population caused by pump erbium spontaneous emission (ESA) and cooperative upconversion.

Spontaneous emission is an important factor present in all optical amplifiers. All excited ions can spontaneously relax from the upper state to the ground state by emitting a photon that is uncorrelated with the signal photons and it can be amplified along the fiber by stimulating the emission of more photons. This process can occur at any frequency within the fluorescence spectrum of the amplifier transition and it reduces the gain of the amplifier since it takes photons that could be part of stimulated emission by the signal photons. Additional problem is that amplified spontaneous emission (ASE) can propagate in both directions along the fiber.

FIG. 4.15 (a) shows ASE spectra in an Er-Te fiber, with 980 nm laser used as a counter-pump. In this case, the pump power was increased from 50 to 150 mW. As we can see, in the range between 1480 and 1560 nm, the ASE power increases with increasing pump power, and the intensities of the resonance lines at 1566, 1591 and 1600 nm also increase. A similar behavior is observed when a 1480 nm pump was used as a counter-pump, presented on FIG 4.15 (b). The ASE spectra in this case are narrower, since the spectral range around 1480 nm overlaps with the pump laser line at that frequency. The presented measurements were conducted with an erbium-doped 1.25 m long tellurite fiber, at room temperature.



a)



b)

FIG. 4.15 ASE spectra in an Er-Te fiber, a counter-pumping with: a) 980 nm and b) 1480 nm laser.

At high pump powers, high inversion is achieved in these samples. With high inversion, the most of the population is in the upper state and the gain factor is proportional to the cross section. For low pump powers, the gain factor becomes strongly dependent on the ratio between the emission and absorption cross sections and to the exact distribution of the population between the upper and lower states. The length of the fiber here plays an important role since the fiber needs to be long enough to allow the ASE to build up. We can calculate the cross sections and the level population for our fiber as well, but it looks like for a bidirectional pumping scheme the inversion is lower in the beginning section of the fiber, because the backward propagating ASE has reached its highest power there and is significantly depleting the inversion. Later, we present emission results achieved with 980 nm bidirectional pumping for complete population inversion along the fiber.

Typical ASE spectra excited in bidirectional pumping scheme are presented in FIG. 4.16. The fiber spectra reveal a broad erbium amplified spontaneous emission and several lasing or resonance lines. The ASE band, approximately 180 nm wide (at 30 dB from max), is one of the broadest reported to date. The resonance lines appear on the top of the ASE band. The most interesting observation here is that those resonance lines correspond to transitions to those observed in the CEES emission spectra (atomic transitions) (see section 4.5, FIG. 4.21). Samples of different lengths, from 0.05 to 2.4 m were tested and all found to present similar spectral features and lasing lines. However, these lines were observed to shift to longer wavelengths with increasing fiber length.

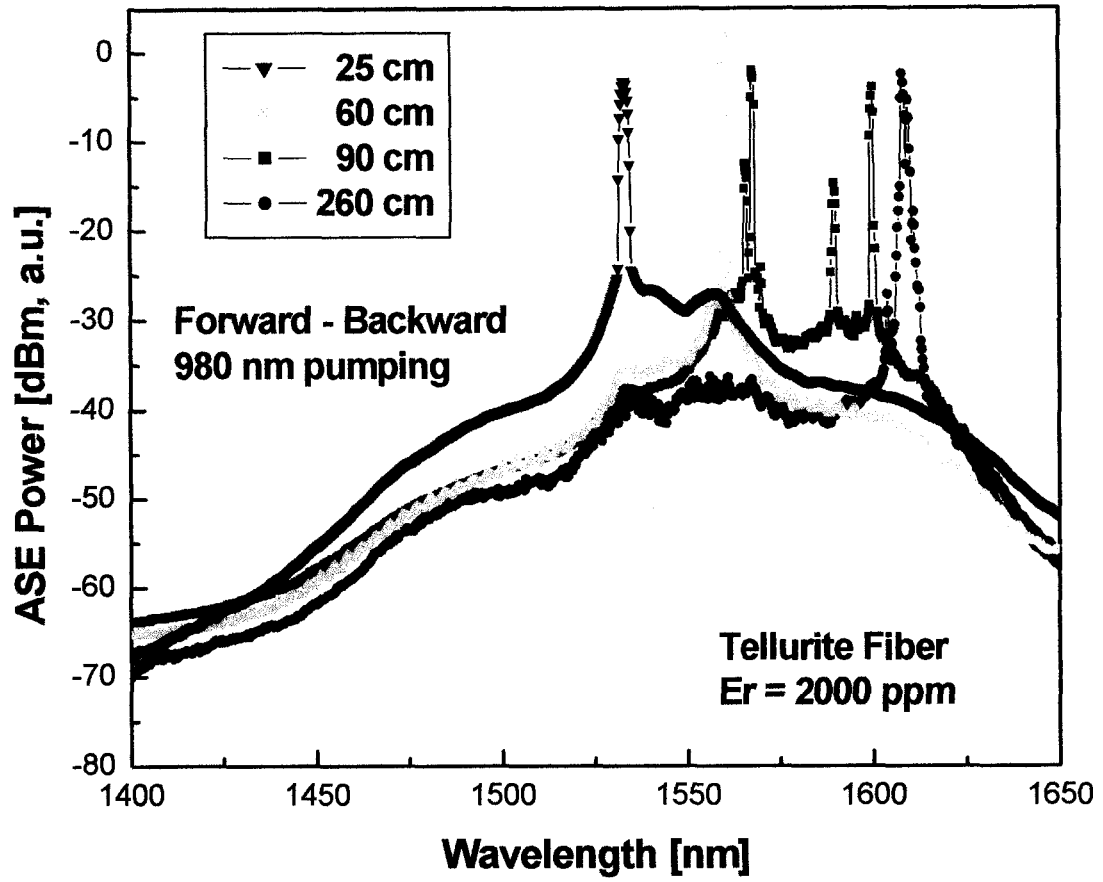


FIG. 4.16 ASE spectra of Er-doped tellurite fiber for different fiber lengths.

Lasing occurs because these fibers were cleaved and polished at the ends, thereby forming a cavity: successive back reflection from the ends of the tellurite fiber sample and the large refractive index difference between the tellurite fiber and the spliced silica fibers enhance Fresnel reflection. For signal gain measurements, lasing lines were avoided by cutting and polishing the fiber ends at an angle of  $\sim 8^\circ$ . FIG. 4.17 presents some of the results on small signal gain amplification in erbium-doped tellurite glasses. From the data in the same figure, a signal net gain of 20 – 30 dB is estimated in a 1 m long fiber ( $\sim 30$  dB at 1550 nm) [Marjanovic *et al.*<sup>5,24</sup>].



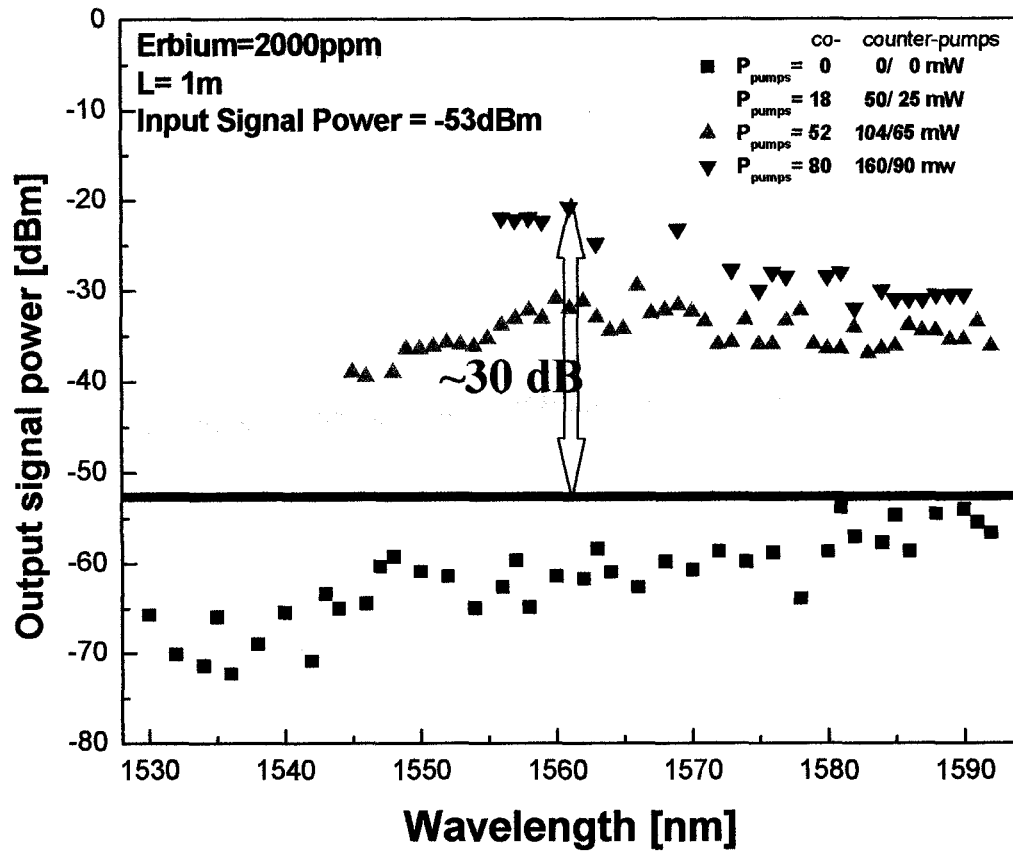


FIG. 4.17 Output signal power vs. wavelength.

A comparison of tellurite and alumina-silica ASE spectra is presented in FIG. 4.18 (a) and (b). The tellurite fiber spectra reveal a broader erbium ASE. The major difference between spectra occurs between 1575-1610 nm. The erbium emission spectra in tellurite are broader than in silica fiber. In addition, the resonance lines appear on the top of ASE curves of tellurite fiber, while such lines are not observed in the corresponding spectra of silica fibers. This suggests that the lower energy transitions are stronger in  $\text{Er}^{3+}$ -doped  $\text{TeO}_2$  than in  $\text{Al}_2\text{O}_3$ - $\text{SiO}_2$  fibers. It appears that alumina-silica fiber is more efficient at low pump power, which might be due to a higher erbium concentration and lower intrinsic losses of this fiber.

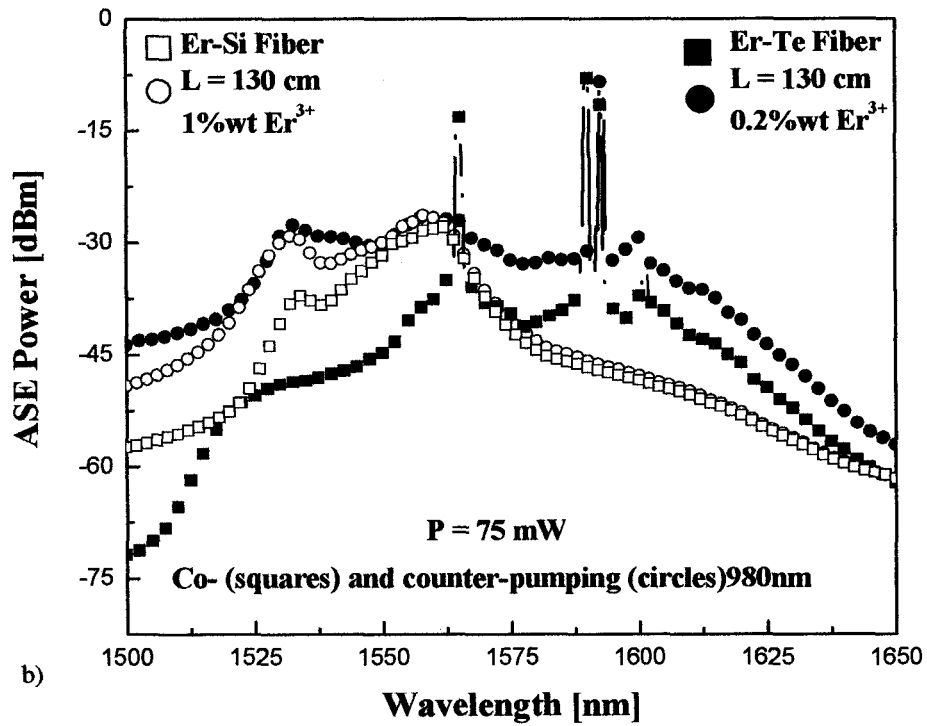
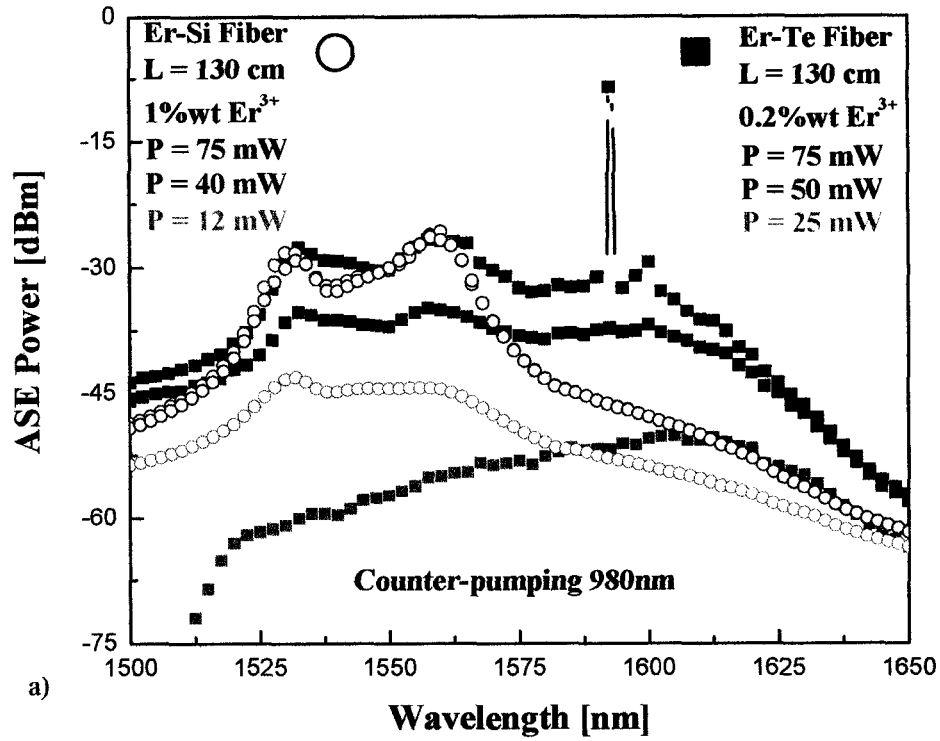


FIG. 4.18 a) The Er<sup>3+</sup> emission spectra for 1.3 m long tellurite and alumina-silica fibers, counter-pumped with 980 nm light; b) the Er<sup>3+</sup> emission spectra for 1.3 m long tellurite and alumina-silica fibers, co- and counter-pumped with 980 nm light, for a pump power of 75 mW.

As can be seen at FIG 4.18 (a), the ASE in the alumina-silica fiber saturates at lower power and no lasing has been observed so far, even without cutting the fiber at a non-90° angle. The saturation occurs for relatively low pump powers starting at ~50 mW and depends on the fiber length. By contrast, no saturation was observed in the tellurite fiber, even for pump powers in excess of 500 mW. This represents an additional advantage of the tellurite fiber for erbium doped fiber amplifier (EDFA) applications.

The threshold pump power for stimulated emission for fixed fiber lengths is found to be lower for the alumina-silica fiber, 2 mW, than for the tellurite fiber, 22 mW. Because of the coupling losses, these values correspond to the launched power but not to the exact input power into the fibers under test. The estimated coupling losses for the mechanically spliced tellurite fiber were  $\leq 0.5$  dB and for the fusion spliced alumina-silica fiber to conventional SM-28 fiber were 0.01 dB. The  $\text{Al}_2\text{O}_3$ - $\text{SiO}_2$  fiber had an attenuation of 12.5 dB/km in the wavelength range 1100-1200 nm; 80dB/m absorption at 980 nm and 60 dB/m emission at 1526 nm. Background losses in the tellurite fiber were about 0.2 dB/m. From an estimate of the coupling losses, the slope efficiency for lasing in the  $\text{TeO}_2$  fiber at 1533 nm was calculated to be approximately 1.2%. Assuming equal emission from both ends of the fiber, the slope efficiency above the threshold was 2.4%. The maximum output power obtained with 300 mW of pump power was about 4 mW.

As suggested by Sudo<sup>25</sup> and measured by Zemon *et al.*<sup>26</sup> in silicate, fluorphosphate and fluoride glasses at low temperature, erbium has the broader Stark splitting in silica host. Authors concluded that wider inhomogeneous broadening and almost identical homogeneous broadening then in the silica glass are the reasons for broader fluorescence spectra at room temperature. According to our low temperature

measurements published in Marjanovic *et al.*<sup>5</sup>, it appears that  $\text{Er}^{3+}$  ions in tellurite-based glasses also have a narrower Stark split than silica glass. Still, room temperature measurements reveal broader erbium ASE spectra in case of tellurite, just as in case of fluoride host. Thus, either wider inhomogeneous or homogeneous broadening (or both) in tellurite than in silica must be the reasons for that. These factors could lead to denser and flatter spectra in the tellurite glass than in the alumina-silica one. The origin of this effect may also lie in higher transition efficiencies between  $\text{Er}^{3+}$  energy levels at longer wavelength part of the spectra. Its detailed nature will be explained further in Chapter 5.

The alumina-silica fiber had significantly lower losses than the tellurite one. Not unexpectedly at this stage of development, the physical properties of the  $\text{Al}_2\text{O}_3$ - $\text{SiO}_2$  fiber are also much better than those of the tellurite fiber. However, the tellurite fiber offer higher and flatter signal gain over shorter lengths and the alumina-silica fiber lower losses and better physical properties.

#### 4.5 CEES results

One of the possible explanations for broad erbium ASE spectra in the tellurite glass is site-to-site difference in glass host. High-resolution CEES technique is an excellent tool to check this hypothesis since it allows selective excitation of erbium in different environments. CEES measurements were performed in the laboratory of Professor Volkmar Dierolf, with significant help of Christian Sandmann and Zackery D. Fleischman. FIG. 4.19 presents a CEES spectrum of  $\text{Er}^{3+}$  in the alumina-silica glass, near

1.5  $\mu\text{m}$ , at room temperature. It reveals only one strong emission maximum. The CEES spectra in tellurite glass are very similar.

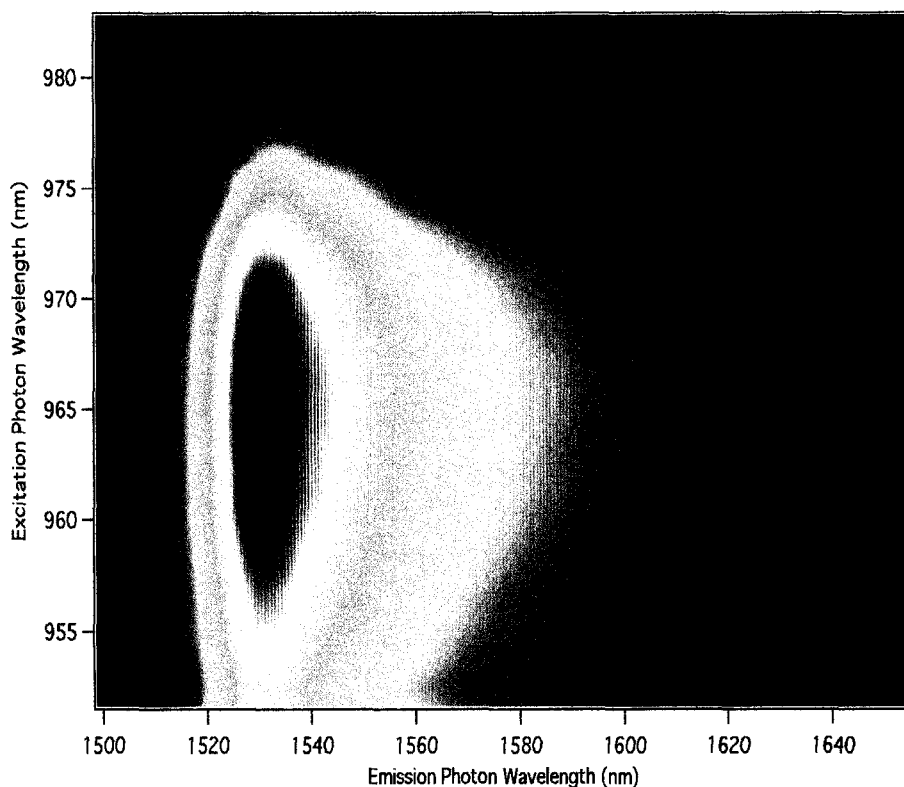


FIG. 4.19 CEES spectra of  $\text{Er}^{3+}$  in alumina-silica glass, near 1.5  $\mu\text{m}$ , at room T.

To check the possibility of additional sites in tellurite glass we concentrate on emission around 550 nm, shown in FIG. 4.20, since it is better resolved than the 1.5  $\mu\text{m}$  one. For a particular excitation around 980 nm (1.277 eV), marked by horizontal lines, we get discrete emission energies (vertical lines) around 550 nm (2.25 eV). Strong maxima regions correspond to the major erbium site. The other not so strong maxima regions suggest other possible sites, but they are not significantly populated. Thus, their contribution should not greatly influence the width of the emission spectra.

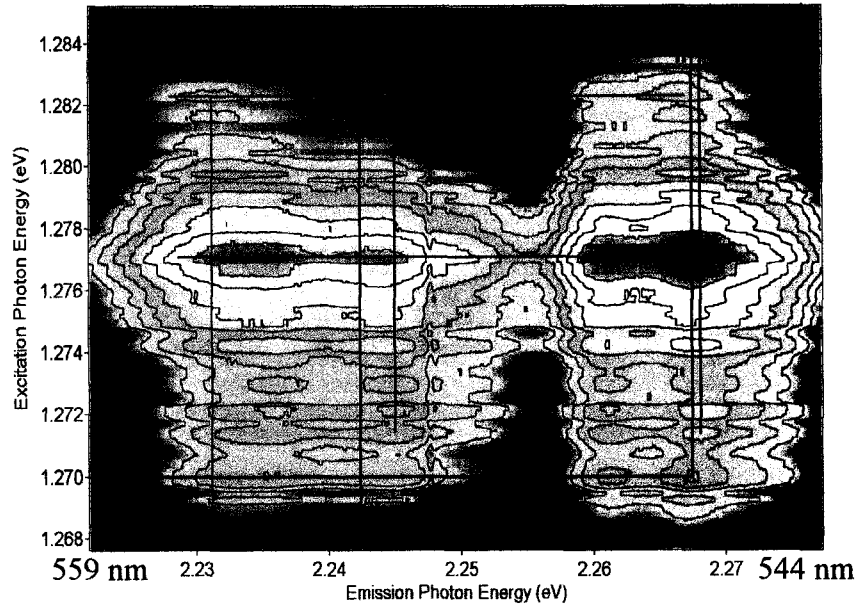


FIG. 4.20 CEES spectra of  $\text{Er}^{3+}$  in zinc-tellurite glass, near 550 nm, at room T.

Presented in FIG. 4.21 (a) are erbium emission spectra at different temperatures, for the  $5\text{Na}_2\text{O} \cdot 15\text{ZnO} \cdot 79\text{TeO}_2$  sample. It was prepared from the preform glass rod with a core of approximately 10  $\mu\text{m}$ : it had a cylindrical shape with a radius of 0.001 m and a height of 0.01 m. Measurements were done for different temperatures from 4.2 to 260 K. FIG. 4.21 (b) reveals the same spectra from FIG. 4.21 (a), but this time normalized to the intensity of 1535 nm peak. Normalization is justified with this peak showing the smallest dependence on temperature. The erbium emission broadens with increasing temperature strongly suggesting phonon influence (homogeneous broadening). As the temperature increases, peaks appear at both sides of main 1530 nm peak and the linewidth increases due to increase of the number of phonons and non-radiative transitions. The peak at 1530 nm remains visible even at high temperatures. This suggests that this peak comes from direct radiative transition from  $^4\text{I}_{13/2}$  first excited to  $^4\text{I}_{15/2}$  ground state. Features at both sides of main 1530 nm peak appear as phonon sidebands.

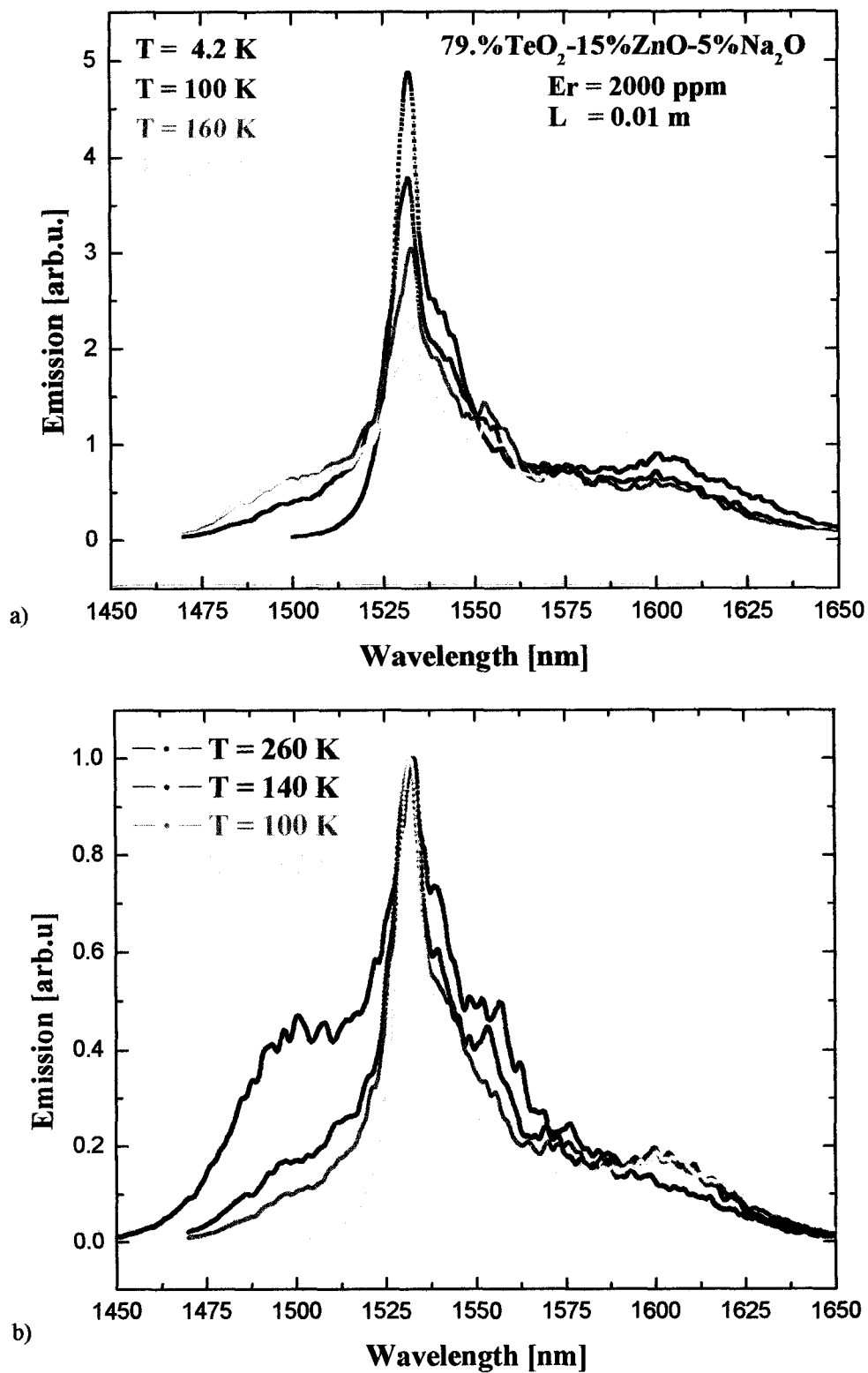
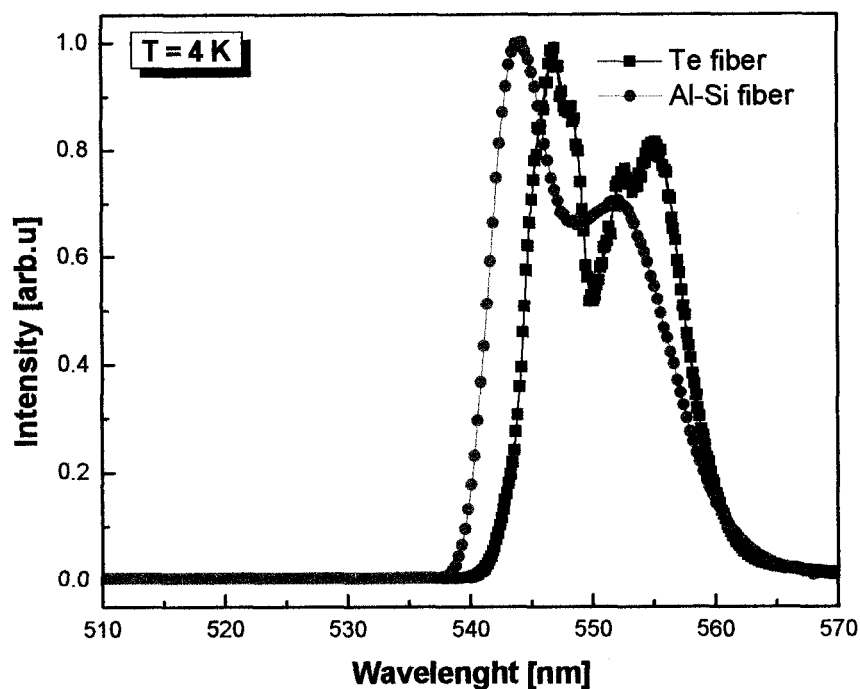


FIG 4.21 The 5Na<sub>2</sub>O·15ZnO·79TeO<sub>2</sub> sample, at different T: a) Er<sup>3+</sup> emission spectra, b) normalized spectra.

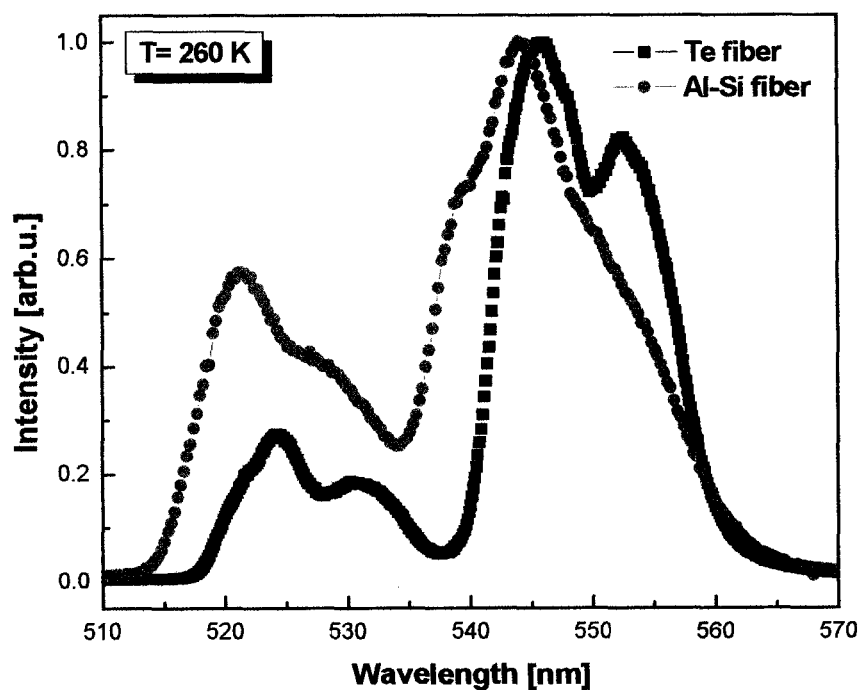
FIG. 4.22 reveals the  $\text{Er}^{3+}$  emission spectra, at (a)  $T = 4 \text{ K}$ , and (b)  $T = 260 \text{ K}$ , in  $\text{Al}_2\text{O}_3\text{-SiO}_2$  and tellurite fibers around 550 nm, excited through a two-photon absorption up-conversion process. The splitting of the emission peaks reflects the Stark splitting of the  $^4\text{I}_{15/2}$  ground state. The relative shift of the peaks reflects the differences in the crystal field of the two hosts. At  $T = 260 \text{ K}$ , there are two sets of peaks, each revealing the Stark splitting of the ground state. The group of peaks in the 535-560 nm wavelength range corresponds to green emission from  $^4\text{S}_{3/2}$  to the ground  $^4\text{I}_{15/2}$  state and the other to the left, in the 515-535 nm range, to emission from the first excited  $^2\text{H}_{11/2}$  to the ground  $^4\text{I}_{15/2}$  state. Both graphs show a higher emission at longer wavelengths in the  $\text{TeO}_2$  than in the alumina-silica fiber (see e.g. differences between the black and grey curves between 550-575 nm). Since transition probabilities are a function of the overlap of the wavefunctions of different energy states, this suggests that relative transition probabilities might be different for different fiber glass hosts.

The present results suggest that the relative transition probability of the lower energy transitions, both from  $^4\text{S}_{3/2}$  and  $^4\text{I}_{13/2}$  (excited states) to the ground  $^4\text{I}_{15/2}$  state, is higher in tellurite than in alumina-silica fibers. This, we propose, is the explanation for the broader gain curve reported in  $\text{TeO}_2$  fibers.





a)



b)

FIG. 4.22 The Er<sup>3+</sup> emission in ZnO-TeO<sub>2</sub> and Al<sub>2</sub>O<sub>3</sub>-SiO<sub>2</sub> fibers, near 550 nm:

a) at T = 4 K and b) at T = 260 K.

The  $\text{Er}^{3+}$  emission spectra in  $\text{Al}_2\text{O}_3\text{-SiO}_2$  ( $\text{Er}^{3+} = 10,000$  ppm),  $\text{ZnO-TeO}_2$  ( $\text{Er}^{3+} = 2,000$  ppm) and  $\text{WO}_3\text{-TeO}_2$  ( $\text{Er}^{3+} = 2,000$  ppm), near 1550 nm, at  $T = 4.2$  K, are shown in FIG. 4.23 (a). We also measured the  $\text{Er}^{3+}$  emission in these three host materials at room temperature, presented in FIG. 4.23 (b). The W-Te and Al-Si curves are smoother, because they were taken with a newer model of detector with higher signal to noise ratio than the one used to detect Zn-Te spectra. The spectra were scaled to the same erbium concentration. Low temperature measurements are necessary in order to resolve individual peaks and to obtain estimates for their linewidth. It appears that the transition probabilities at longer wavelengths and higher temperatures are higher in tellurite than they are in alumina-silica. Furthermore, emission in tungsten-tellurite at low temperature is even stronger than in zinc-tellurite. A better-resolved peak around 1600 nm might be the cause of this effect.

In room temperature spectra, it is even more obvious that erbium emission is significantly broader in tellurite than in alumina-silica. Again, the erbium emission in tungsten-tellurite is also broader than in zinc-tellurite host. The differences in these emission spectra will be discussed in details in Chapter 5. At this point, however, it is worth mentioning the influence of phonons since phonon population increases with temperature, as explained in Chapter 3 (see Eq. (3.7)).

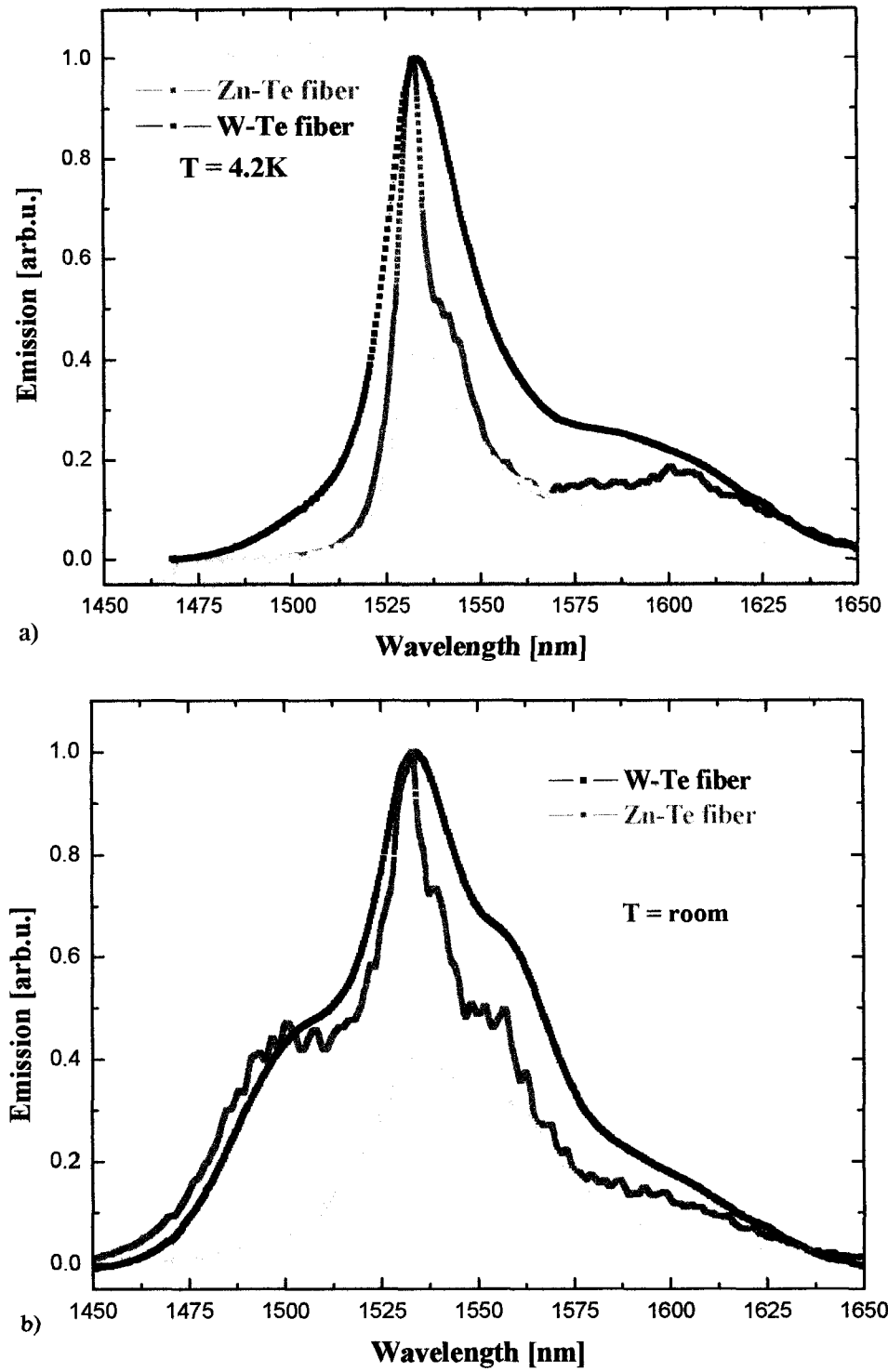


FIG. 4.23 The  $\text{Er}^{3+}$  emission spectra in  $\text{Al}_2\text{O}_3\text{-SiO}_2$ ,  $\text{ZnO-TeO}_2$  and  $\text{WO}_3\text{-TeO}_2$ , near 1.5  $\mu\text{m}$ , at: a)  $T = 4.2 \text{ K}$ ; b) room  $T$ .

FIG. 4.24 shows the wavelength assignment of  $\text{Er}^{3+}$  ion fluorescence (radiation transitions) from the  $^4\text{I}_{13/2}$  to the  $^4\text{I}_{15/2}$  level for an  $\text{Al}_2\text{O}_3\text{-SiO}_2$  glass host: (a) shows the Stark levels and related fluorescence transition, and (b) shows the spectral composition of the room-temperature fluorescence for the alumina-silica host [Desurvire & Simpson<sup>27</sup>].

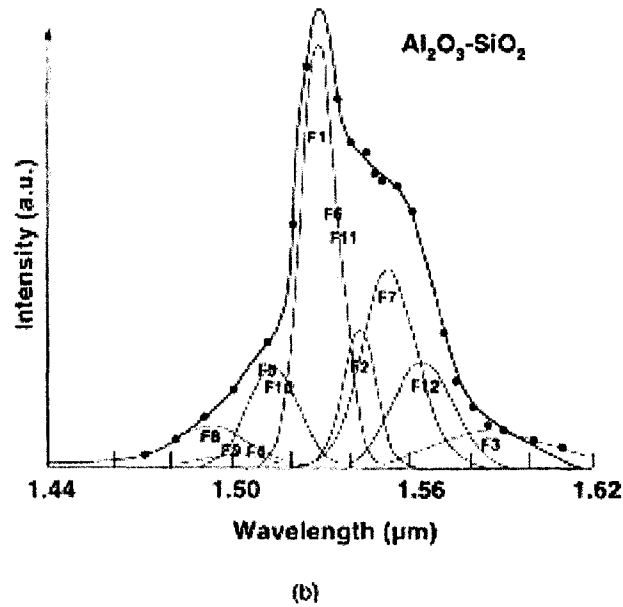
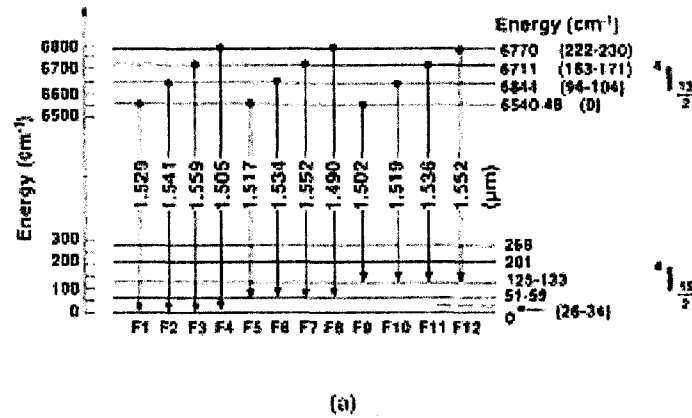


FIG. 4.24 Wavelength assignment of  $\text{Er}^{3+}$  ion fluorescence from the  $^4\text{I}_{13/2}$  to the  $^4\text{I}_{15/2}$  for an  $\text{Al}_2\text{O}_3\text{-SiO}_2$  glass host: (a) the Stark levels and related fluorescence transition, and (b) the spectral composition of the room-temperature fluorescence for the alumina-silica host [Desurvire & Simpson<sup>27</sup>].

Absorption and fluorescence spectra have been reported at three temperatures, 4.2 K (liquid helium), 77 K (liquid nitrogen) and 300 K (room temperature). A comparative analysis between spectra at different temperatures has allowed to infer the number of Stark levels, although the lack of resolution did not allow authors to obtain all such levels. Zemon *et al.*<sup>26</sup> have made more accurate fluorescence line narrowing (FLN) measurements and have shown that up to eight Stark levels can be identified in the  $^4I_{15/2}$  state in silicate and fluoride glasses. This number of Stark levels represents the maximum allowed by Kramers' Rule and indicates that the symmetry of the  $Er^{3+}$  site in those glasses is of a type lower than cubic. Assuming the same symmetry, a comparison of Stark energies for different types of glass hosts shows that the total Stark splitting for  $^4I_{13/2}$  and  $^4I_{15/2}$  varies between  $400\text{ cm}^{-1}$  and  $500\text{ cm}^{-1}$ , corresponding to an average Stark level separation of  $50\text{-}70\text{ cm}^{-1}$  [Desurvire & Simpson<sup>27</sup>].

More interesting is the observation of the relative strength of the radiative transitions within the same manifold in different glass hosts. One could consider the influence of local symmetry for the different relative strengths. FIGS. 4.25 and 4.26 show the deconvolution of the  $Er^{3+}$  emission spectrum in three different host materials, at temperature  $T = 4.2\text{ K}$  and at room temperature, respectively: (a) alumina-silica, (b) zinc-tellurite, and (c) tungsten-tellurite. At the lowest temperature ( $T = 4.2\text{ K}$ ), only the lowest energy levels of each manifold are populated, which reduces the number of observed transitions and accidental degeneracies. A strong overlap exists between many Stark components of the  $^4I_{13/2} \rightarrow ^4I_{15/2}$  transition of erbium in glass, which is the reason why we assigned fewer number of emission bands to peak deconvolution than the total number of peaks. However, the position of bands should hardly change with temperature.

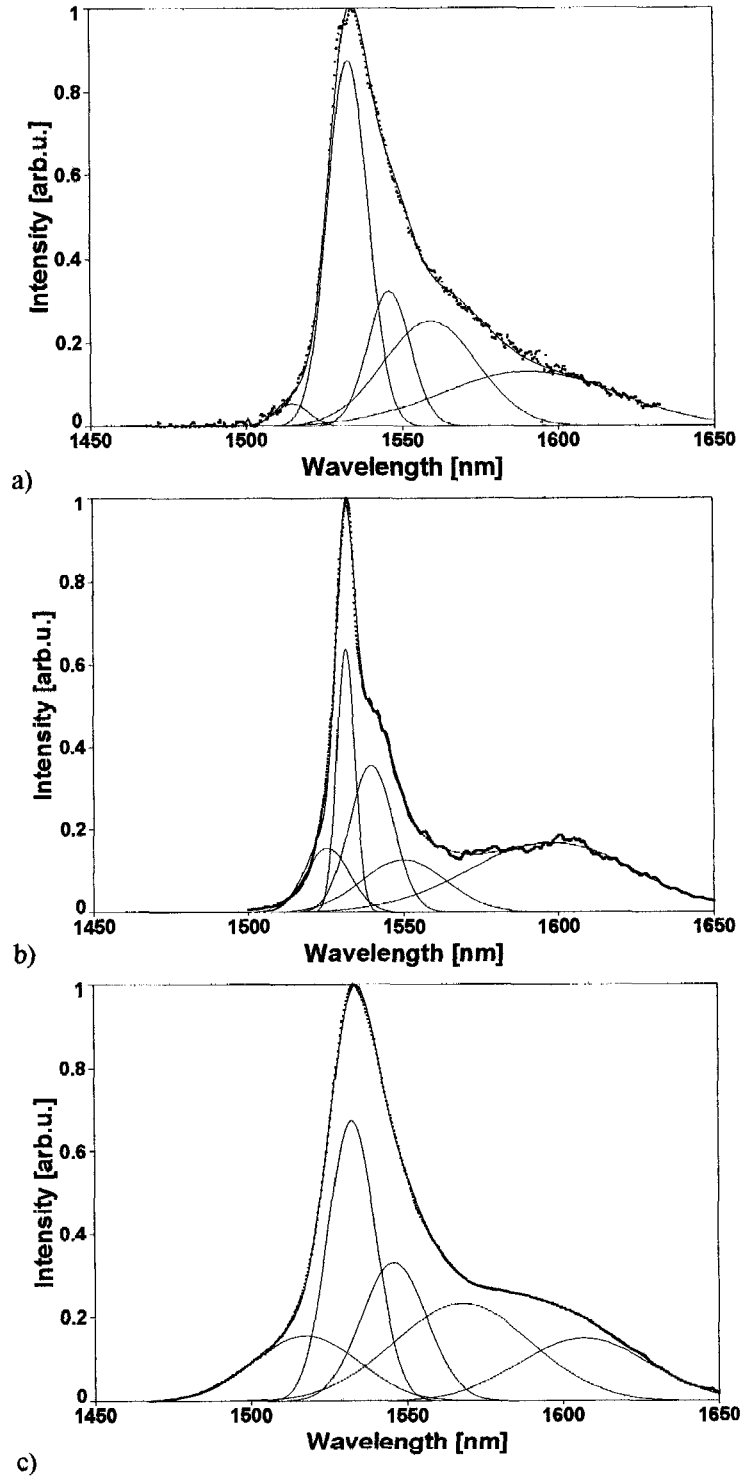


FIG. 4.25 Deconvolution of  $\text{Er}^{3+}$  emission spectrum in three different host materials, at  $T = 4.2 \text{ K}$ : (a) alumina-silica, (b) zinc-tellurite, and (c) tungsten-tellurite.

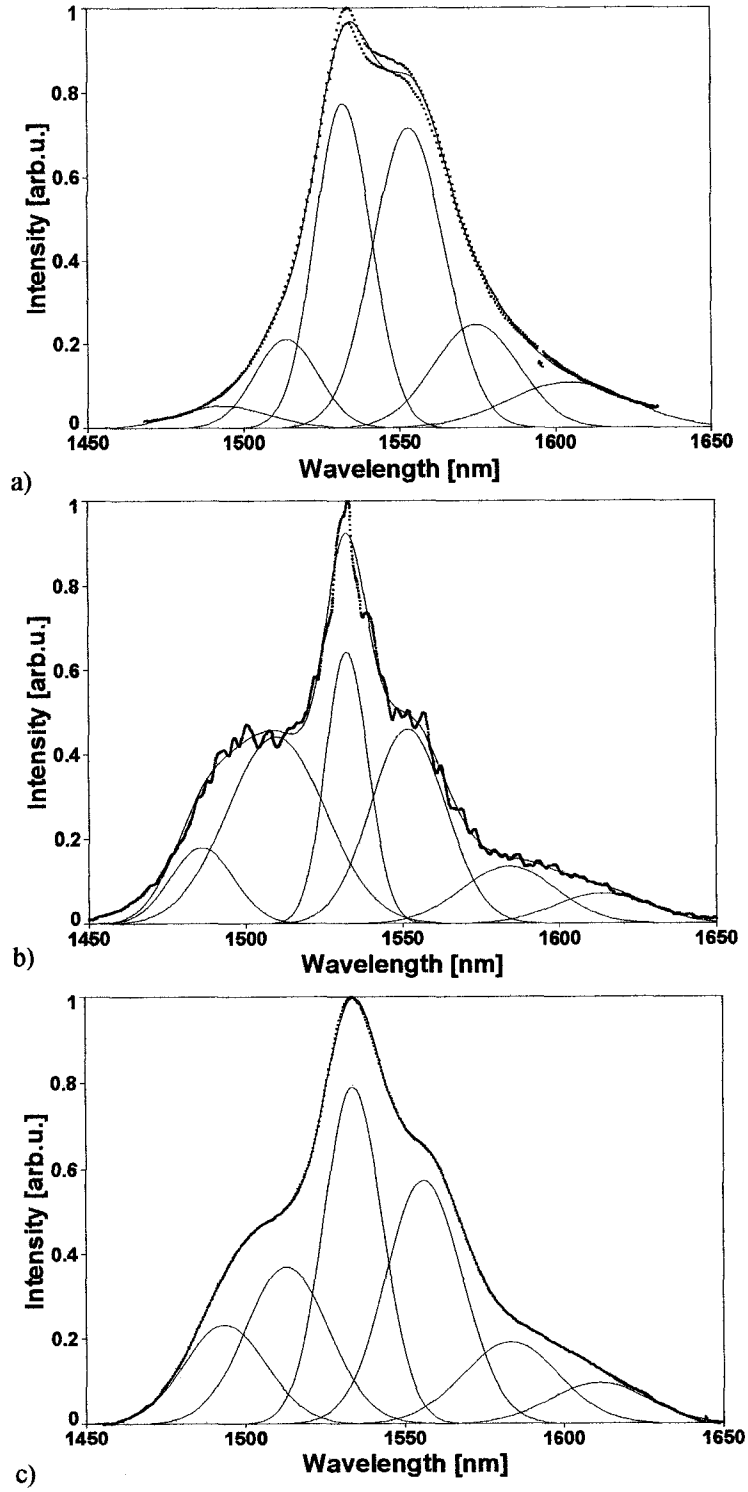


FIG. 4.26 Deconvolution of  $\text{Er}^{3+}$  emission spectrum in three different host materials, at room temperature: (a) alumina-silica, (b) zinc-tellurite, and (c) tungsten-tellurite.

In spite of smearing effects of inhomogeneous broadening, the spectral structure changes with temperature. A broadening and appearance of additional peaks occur due to transitions from thermally excited states. The strongest spectral band at  $\sim 1.53 \mu\text{m}$  is present in all three glasses. Both measurements at 4.2 K and at room temperature reveal that all three host materials have another strong spectral band at  $\sim 1.56 \mu\text{m}$ . At room temperature, only zinc- and tungsten-tellurite present strong bands at  $\sim 1.51 \mu\text{m}$ . Bands at  $\sim 1.51 \mu\text{m}$  and at  $\sim 1.56 \mu\text{m}$  appear in these two hosts at room temperature as side bands to the main spectral band at  $\sim 1.53 \mu\text{m}$ . It appears that spectral bands at longer wavelengths for all three hosts do not change significantly with temperature. On the other side of the spectra, the spectral bands between  $1.47 \mu\text{m}$  and  $1.53 \mu\text{m}$  in zinc- and tungsten-tellurite are significantly stronger at room temperature than at  $T = 4.2 \text{ K}$ . Spectral intensity at this wavelengths range in alumina-silica is very weak.

One interesting result was observed in erbium emission spectra of zinc-tellurite glass at 100 – 120 K temperature range. These spectra are shown in FIG. 4.27 (2.20 eV = 564 nm; 2.40 eV = 517 nm). As temperature increases (in steps of 20 K), we note a continuous line broadening. Additional transitions show up, which is expected because of thermally excited states and are just the replica of the first profile. They are determined by Boltzmann statistics for population of states. A change in transition occurred between 100 and 120 K. At this point, we do not have an explanation for this effect; however, this “phase transition” could be a locking of the erbium ion in one type of structural environment or a change in the erbium environment.



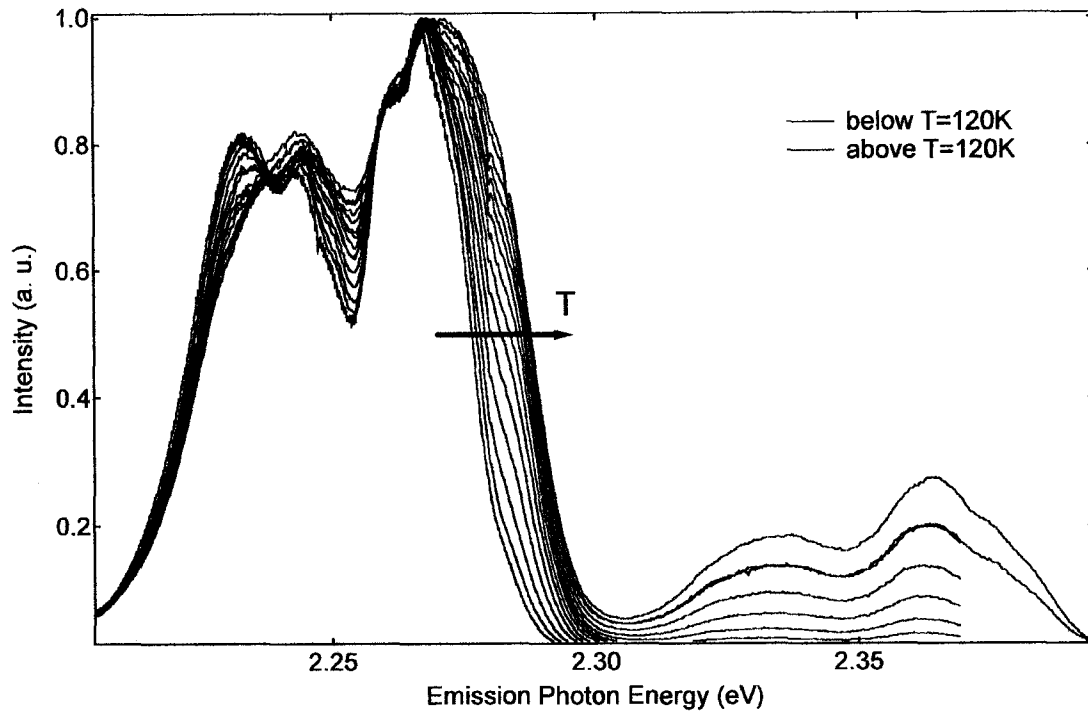


FIG. 4.27 Erbium emission spectra of zinc-tellurite glass, near 550 nm, for different temperatures.

#### 4.6 Absorption results

Absorption measurements were performed on fiber samples of different lengths, as shown in FIG. 4.28, from a few cm to 2.5 m, for several reasons. First, measuring the absorption in the shortest samples avoided the effects of re-absorption and re-emission that can occur along the fiber and have the strong peaks still in scale. Second, absorption results for such short samples are similar to those in bulk material. Third, some

absorption lines are too weak for short samples and the best way to measure them is to increase the effective length of the measured fiber (increase the absorption cross-section).

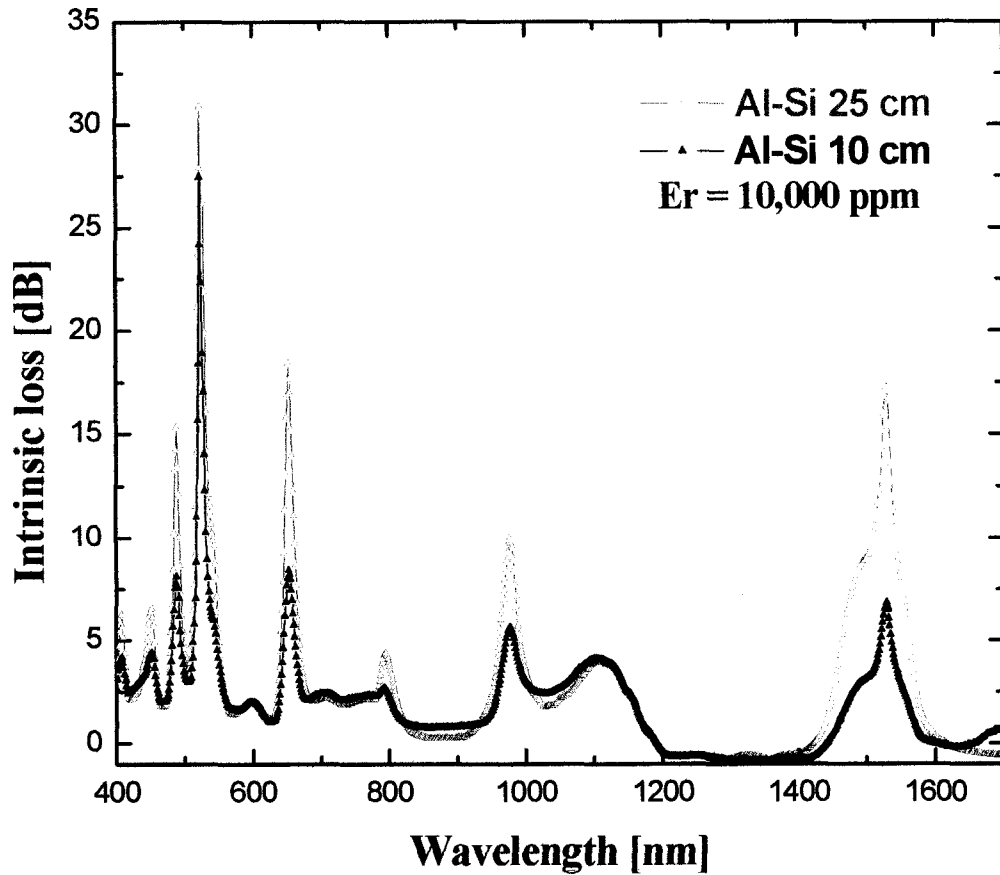


FIG. 4.28 Absorption spectra of  $\text{Er}^{3+}$  doped  $\text{Al}_2\text{O}_3$ - $\text{SiO}_2$  fibers of different lengths.

Although most optical studies were performed in bulk materials, we also investigated glass fiber samples. Measured ground state absorption spectra of  $\text{Er}^{3+}$ -doped (2,000ppm) zinc-tellurite and  $\text{Er}^{3+}$ -doped (10,000ppm) alumina-silica fibers are presented in FIG. 4.29.

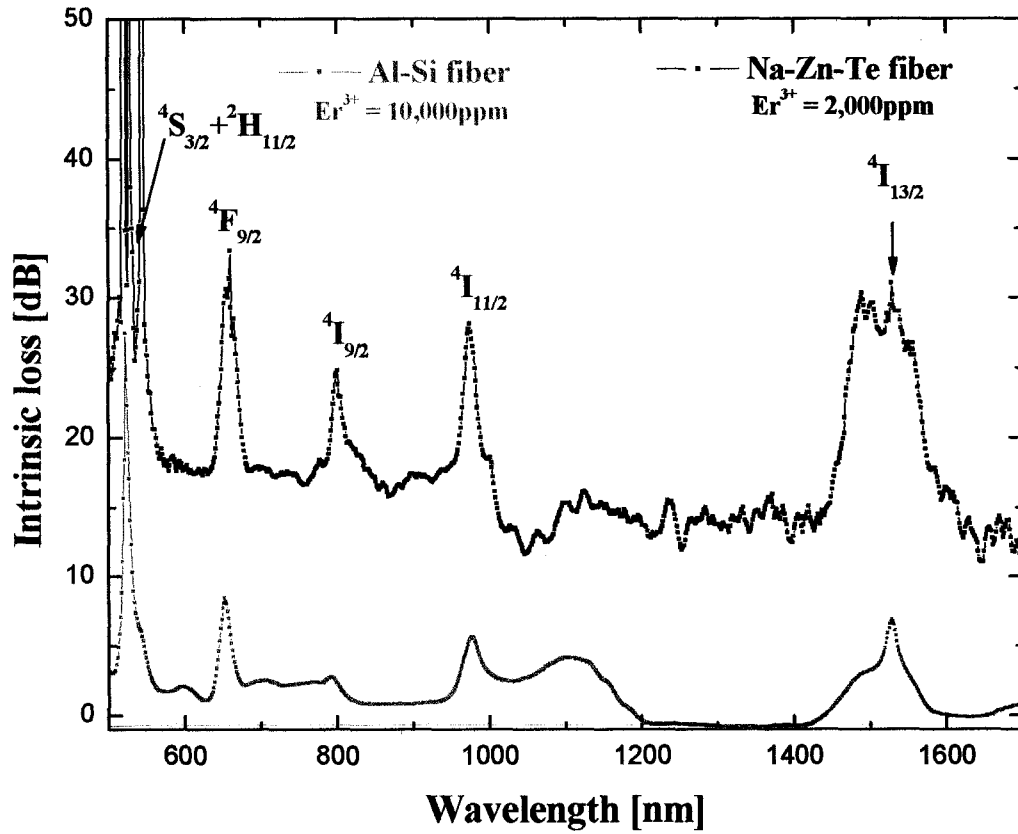


FIG. 4.29 Ground state absorption spectra of  $\text{Er}^{3+}$ -doped zinc-tellurite and alumina-silica fibers.

The several ground state absorption bands are labeled according to the final states of the respective transitions. FIG. 4.29 clearly shows five absorption bands from  $^4\text{I}_{15/2}$  ground state to  $^4\text{S}_{3/2} + ^2\text{H}_{11/2}$ ,  $^4\text{F}_{9/2}$ ,  $^4\text{I}_{9/2}$ ,  $^4\text{I}_{11/2}$ , and  $^4\text{I}_{13/2}$  at 0.53-0.55, 0.66, 0.8, 0.98, and 1.55 microns, respectively. The observed and calculated oscillator strengths of  $\text{Er}^{3+}$  in sodium-zinc-tellurite and alumina-silica glass fibers are given in Table 4.1. All the manifolds lying above  $^2\text{H}_{11/2}$  level were excluded from the calculation since we could not derive a correct estimate of their integrated absorption  $\int k(\lambda)d\lambda$  because of the presence of some unidentified sources of strong optical absorption and instrumentation limits. Theoretical  $f$  values were determined using the Eq. (2.6). The root mean square (RMS)

deviation of the  $f$ -calculated from the  $f$ -measured was calculated from the residuals. It was found to be approximately 20% of the average oscillator strengths, which is a relatively good accuracy according to literature. The  $U^{(\lambda)}$  matrix elements given in Table 4.1 do not differ significantly for different hosts and they are available in many papers, see ex. Sudo<sup>25</sup>, Kaminskii *et al.*<sup>28</sup>.

$J$ manifold	$\lambda$ ( $\mu\text{m}$ )	$(U^{(2)})^2$	$(U^{(4)})^2$	$(U^{(6)})^2$	Tellurite			Alumina-silica		
					Exp.	Calculated		Exp.	Calculated	
					$f_{ed} \times 10^8$	$f_{ed} \times 10^8$	$f_{md} \times 10^8$	$f_{ed} \times 10^8$	$f_{ed} \times 10^8$	$f_{md} \times 10^8$
$^4I_{13/2}$	1.535	0.0195	0.1173	1.4316	279	204	71	175	108	62
$^4I_{11/2}$	0.98	0.0282	0.0003	0.3953	71	69	0	51	44	0
$^4I_{9/2}$	0.80	0	0.1732	0.0099	66	62	0	27	37	0
$^4F_{9/2}$	0.66	0	0.5354	0.4619	396	408	0	181	169	0
$^4S_{3/2} + ^2H_{11/2}$	0.53	0	0	0.2211	1498	1414	0	562	552	0
	0.55	0.7125	0.4123	0.0925						

Table 4.1 The oscillator strengths of  $\text{Er}^{3+}$  in sodium-zinc-tellurite and alumina-silica glass fibers.

Refractive indices, estimated Judd-Ofelt parameters and measured and calculated radiative lifetime of the glass fibers used here are given in Table 4.2. The lifetime of the  $^4I_{13/2}$  level was measured after excitation at 980 nm, for both sodium-zinc-tellurite and alumina-silica glass fibers. Since the variation of index of refraction  $n$  over the spectral region of interest is less than 5% in either tellurite or silica samples [Mazurin *et al.*<sup>29</sup>], we assume a constant correction factor for fibers of the same glass composition.

Type of glasses		<i>Tellurite</i>	<i>Alumina-silica</i>
Refractive index		2.08	1.468
J-O parameters ( $10^{-20} \text{ cm}^2$ )	$\Omega_2$	$7.7 \pm 0.5$	$4.5 \pm 0.5$
	$\Omega_4$	$2.1 \pm 0.3$	$1.4 \pm 0.2$
	$\Omega_6$	$1.4 \pm 0.2$	$1.0 \pm 0.2$
Lifetime (ms) (calculated)		$2.5 \pm 0.5$	$11.5 \pm 2.5$
Lifetime (ms) (measured)		$1.67 \pm 0.03$	$4.09 \pm 0.03$

Table 4.2 Refractive indexes, Judd-Ofelt parameters and luminescence lifetime of glass fibers used here.

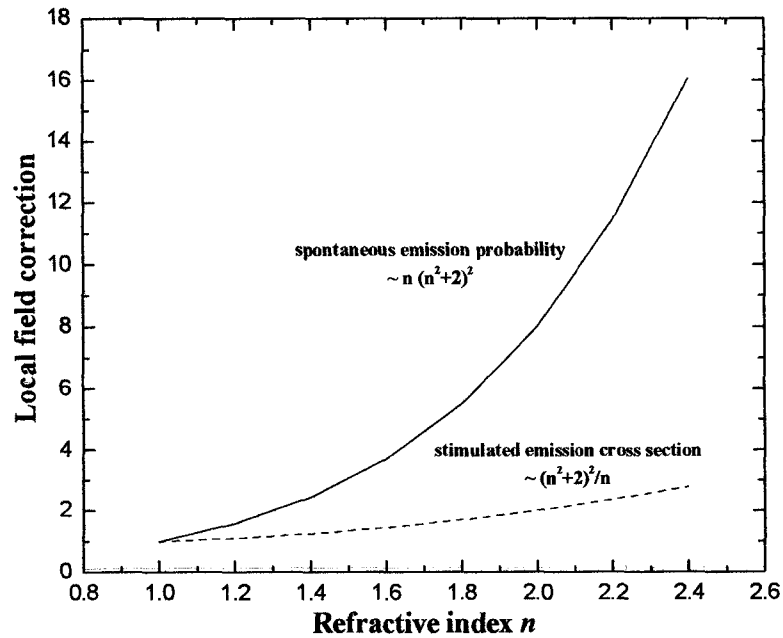


FIG. 4.30 Local field correction factors for electric dipole transitions: spontaneous emission probability (solid line) and emission cross section (dashed line).

The large radiative transition probabilities in tellurite glasses arise from their large index of refraction, in addition from the Judd-Ofelt parameters. The ratio of the effective field at the ion site in the glass to the applied field  $E_0$  in the simple tight binding approximation is given by Dexter<sup>30</sup>:

$$\frac{E_{eff}}{E_0} \approx 1 + \frac{1}{3}(n^2 - 1) + \dots \quad (4.2)$$

This introduces a factor of  $\frac{1}{9}n(n^2 + 2)^2$  in the spontaneous emission probability in Eq. (2.8) and a factor  $(n^2 + 2)^2 / 9n$  in the stimulated emission cross-section in Eq. (2.12). These factors are plotted as a function of refractive index  $n$  in FIG. 4.30. Comparing the index of refraction in alumina-silica glass of 1.468 with  $n$  of tellurite glass of  $\approx 2.1$  for the same values of Judd-Ofelt parameters  $\Omega_k$  and wavelength  $\lambda$ , the radiative lifetime will decrease by more than a factor of three and the stimulated emission cross section will increase by approximately 50%. This can be used to improve spectroscopic properties by compositional changes that would increase the refractive index  $n$ . Our measurements of the radiative lifetime and amplified spontaneous emission in these two materials confirm such predictions. Those results are given in FIG. 4.31 and, previously, in FIG. 4.18. Here, a modulated 980 nm signal was used as a pump for erbium ESA. Such emission was filtered and detected with a 1.5  $\mu\text{m}$  photo detector. The radiative lifetime was calculated from the exponential fit of the decay curve recorded on an oscilloscope.

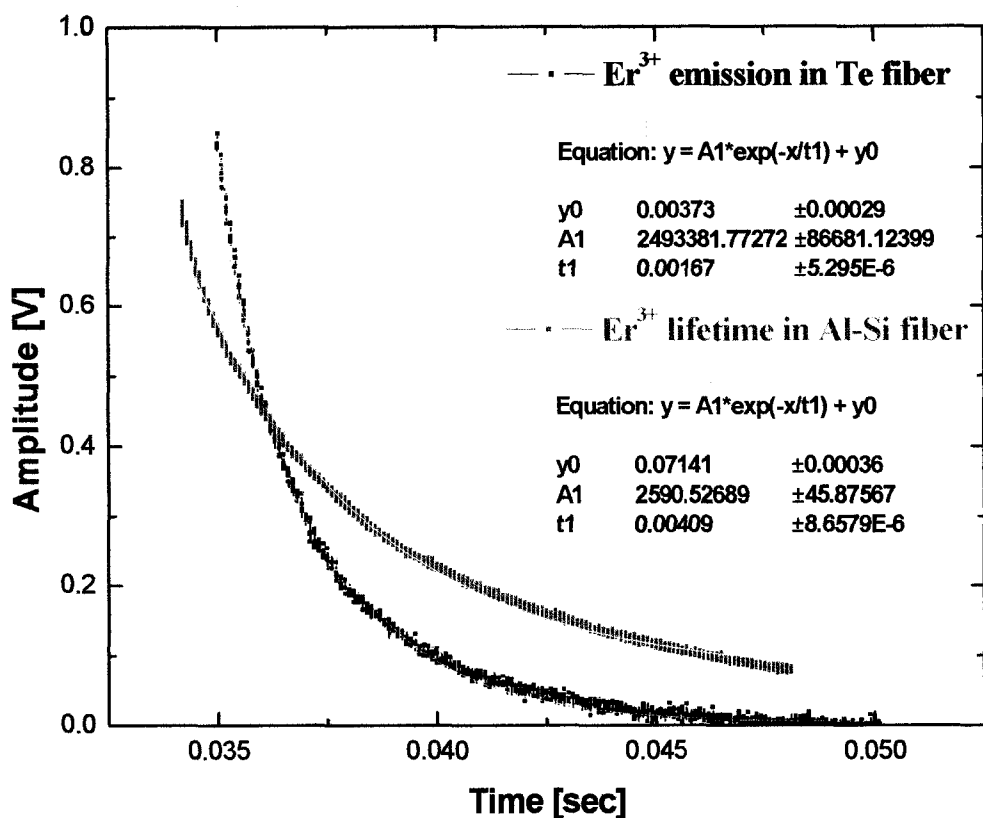


FIG. 4.31 The radiative lifetime measurements in alumina-silica and sodium-zinc-tellurite fiber.

Finally, we present a comparison of erbium absorption around 1.5  $\mu\text{m}$ , in all three host materials: alumina-silica, zinc-tellurite and tungsten-tellurite. The intrinsic losses in silica and Zn-Te were measured in 0.04 m long fibers, at room temperature. A broadband White Light Source (WLS) Ando AQ4303C was used as the probe, and the transmitted light was detected with an optical spectrum analyzer.

Absorbance in W-Te was measured with help of Prof. Michael Stavola and Gang Shi. IR absorption spectra with a resolution of 0.5  $\text{cm}^{-1}$  were measured with a Bomen DA 3.16 Fourier-transform spectrometer equipped with a glow bar source, a KBr beamsplitter

and an InSb detector. The sample was held in a cryostat (Air Products) and the measurements were carried out at room temperature.

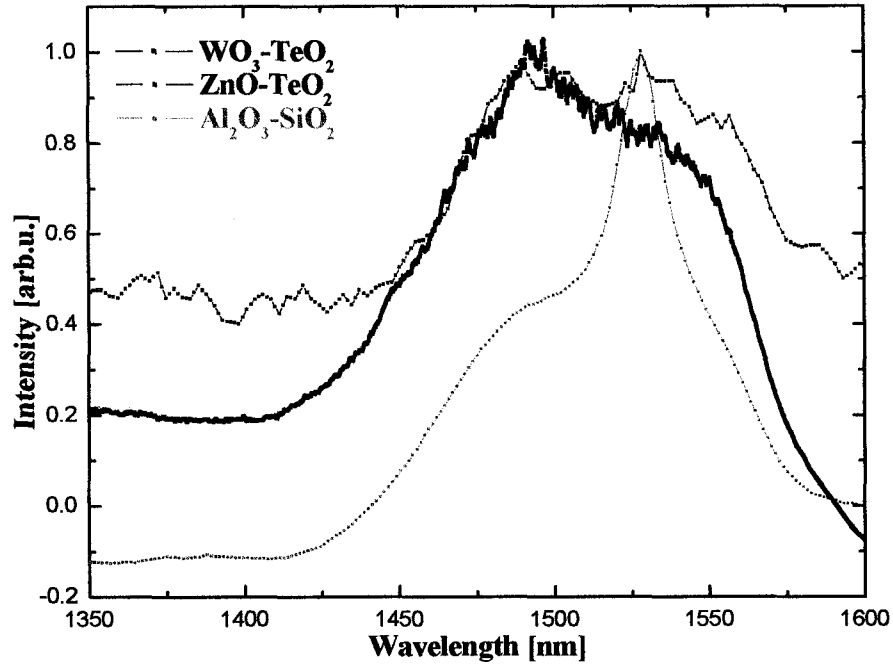


FIG. 4.32 Comparison of erbium absorption in  $\text{Al}_2\text{O}_3\text{-SiO}_2$ ,  $\text{ZnO-TeO}_2$  and  $\text{WO}_3\text{-TeO}_2$  hosts.

As can be seen from FIG. 4.32, absorption in both zinc- and tungsten tellurite is much broader than in alumina-silica, which will have significant impact on re-absorption and re-emission along the fiber (see FIG. 4.18). This will be discussed in details in Chapter 5.



## Bibliography

- [1] T. Sekiya, N. Mochida, A. Ohtsuka, M. Tonokawa, *J. Ceram. Soc. Jpn.* **97** (1989) 1435.
- [2] T. Sekiya, N. Mochida, A. Ohtsuka, M. Tonokawa, *J. Non-Cryst. Solids* **144** (1992) 128.
- [3] T. Sekiya, N. Mochida, A. Ohtsuka, *J. Non-Cryst. Solids* **168** (1994) 106.
- [4] H.M. Moawad, J. Toulouse, H. Jain, A.R. Kortan, Conference preceding, *Proceedings of 103rd Annual Meeting & Exposition of the ACerS Symposium on Optoelectronic and Technology in the Information Age*, **126** (American Ceramic Society, 2001), p. 45.
- [5] S. Marjanovic, J. Toulouse, H. Jain, C. Sandmann, V. Dierolf, A.R. Kortan, N. Kopylov, R.G. Ahrens, *J. Non-Cryst. Solids* **322** (2003) 311.
- [6] R. Sommer, J. Toulouse, and H. Jain, *Proceedings of the Materials Research Society Symposium 407, 1996* (Materials Research Society, 1996), p. 215.
- [7] T.C. Damen, S.P.S. Porto, B. Tell, *Phys. Rev.* **142** (1966) 570.
- [8] V.K. Manilovsky, A.P. Sokolov, *Solid State Commun.* **57** (1986) 757.
- [9] A.J. Martin, W. Brenig, *Phys. Stat. Sol. (b)* **64** (1974) 163.
- [10] C.M. McIntosh, J. Toulouse, P. Tick, *J. Non-Cryst. Solids* **222** (1997) 335.
- [11] P.N. Sen, M.F. Thorpe, *Phys. Rev. B* **15** (1977) 8.
- [12] F.L. Galeener, *Phys. Rev. B* **19** (1979) 8.
- [13] R.L. Mozzi, B.E. Warren, *J. Appl. Cryst.* **2** (1969).

- [14] O. Noguera, T. Merle-Méjean, A.P. Mirgorodsky, M.B. Smirnov, P. Thomas, J.C. Champarnaud-Mesjard, *J. Non-Cryst. Solids* **330** (2003) 50.
- [15] Y.O Bobovish, A.K. Yakhind, *J. Struct. Chem.* **4** (1963) 851.
- [16] T. Sekiya, N. Mochida, S. Ogawa, *J. Non-Cryst. Solids* **176** (1994) 105.
- [17] V. Kozhukharov, S. Neov, I. Gerasimova, P. Mikula, *J. Material Science* **21** (1986) 1707.
- [18] P. Caillet, P. Saumagne, *J. Mol. Struct.* **4** (1969) 191.
- [19] M.F. Daniel, B. Desbat, J.C. Lassegues, B. Gerand, M. Figlarz, *J. Solid State Chem.* **67** (1987) 128.
- [20] H.J. Becher, *J. Less-Common Met.* **76** (1980) 169.
- [21] I. Shaltout, Yi Tang, R. Braunstein, A.M. Abu-Elazm, *J. Phys. Chem. Solids* **56** (1995) 141.
- [22] J. W. Lim, H. Jain, J. Toulouse, S. Marjanovic, J. S. Sanghera, R. Miklos, I. D. Aggarwal, *Proceedings of the 16<sup>th</sup> University Conference on Glass Science*, (RPI, Troy, NY, 2003).
- [23] P.C. Backer, N.A. Olsson, J.R. Simpson, *Erbium-Doped Fiber Amplifiers – Fundamentals and Technology*, Academic Press (1999)
- [24] S. Marjanovic, J. Toulouse, A. R. Kortan, N. Kopylov, “ASE and laser emission in double-clad EDTF”, *OSA Trends in Optics and Photonics (TOPS)*, Vol. **73**, Conference on Lasers and Electro-Optics, OSA Technical Digest, Postconference Edition (Optical Society of America, Washington, D.C., 2002), p. 18.
- [25] S. Sudo (Ed.), *Optical Fiber Amplifiers - Materials, Devices, and Applications*, (Artech House, Inc., Boston, 1997).

- [26] S. Zemon, G. Lambert, W.J. Miniscalco, L.J. Andrew, B.T Hall, *Proceedings of SPIE Conference on Fiber Laser Sources and Amplifiers*, **1171** (1989) 219.
- [27] E. Desurvire, J.R. Simpson, *Optics Lett.* **15** (1990) 547.
- [28] A.A. Kaminskii, V.S. Mironov, A. Kornienko, S.N. Bagaev, G. Boulon, A. Bernier, B. Di Bartolo, *Phys. Stat. Sol. (a)* **151** (1995) 231.
- [29] O. Mazurin, M. Stretsina, T. Shvaiko-Shvaikovskaya (Eds.), *Handbook of Glass data, Single component and Binary Non-Silicate Oxide Glasses*, Physical Science Data **15**, Part B, (Elsevier, Amsterdam, 1985).
- [30] D.L. Dexter, *Solid State Physics*, F. Seitz, D. Turnbull (Eds.) (Academic Press, New York), **6** (1958) 353.

## **Chapter 5**

### **Discussion**

In order to explain the strong and wide erbium emission in tellurite glasses, we first focus our attention on the influence of dopants on the Raman spectra in tellurite glasses, with feedback from supporting XPS results. In addition, we show the connection between the glass structure and its optical properties through the refractive index dependence on the nature and the type of glass molecular units. Finally, we show how emission strongly depends on vibrational properties of the host material.

#### **5.1 Influence of dopants on the Raman spectra of TeO<sub>2</sub> glasses**

We discuss here the influence of dopants on the Raman spectra in tellurite glasses, especially on their network topology. Overall, the 5% Na and 10% Na zinc-tellurite spectra reveal similar effects. Peaks A and C increase with increasing Zn concentration, while peak E decreases. Based on the above results, we are able to comment on how the combined presence of two additional components, Na<sub>2</sub>O and ZnO, in the TeO<sub>2</sub> glass, affects its microscopic structure and its vibrational properties differently as compared to what each would do separately. Stated differently, we are attempting to determine whether their total effect should be described as a simple average of two independent contributions or as a synergistic effect in which the presence of one component enhances the contribution of the other.

The results presented in Chapter 4 indicate that reconstruction of glass network is enabled by the introduction of ZnO in TeO<sub>2</sub> glass. However, it is facilitated or made possible by the additional structural degrees of freedom resulting from the breaking of Te-O bonds by Na. More specifically, we argue here that Zn promotes the formation of new Te<sub>3</sub>O<sub>8</sub> units, shown in FIG. 5.2, from TeO<sub>4</sub> molecular units that have been disconnected by Na. Increasing the concentration of Zn results in the linking of these units into chains. Therefore, sodium opens the glass network and allows zinc to create a new network. However, too high a concentration of Na, at the expense of Te, will prevent chain formation. To justify such a model, it is useful to note that Te<sub>3</sub>O<sub>8</sub> units are present in the β-form of crystalline tellurite and crystalline forms of Zn<sub>2</sub>Te<sub>3</sub>O<sub>8</sub> and Mg<sub>2</sub>Te<sub>3</sub>O<sub>8</sub>. Moreover, according to Sekiya [Sekiya *et al.*<sup>1</sup>], ZnO-TeO<sub>2</sub> glasses have the same structure as MgO-TeO<sub>2</sub> glasses containing about 40% MgO, in which (Te<sub>3</sub>O<sub>8</sub>)<sub>n</sub> units, with n relatively small, are formed. At lower concentrations, giving rise to the A peak, in presence of sodium, Zn plays the role of a network modifier, rather than a network former.

Previously published results in Moawad *et al.*<sup>2</sup> and Marjanovic *et al.*<sup>3</sup> show a greater influence of the Na/Zn ratio at the highest and lowest frequencies for a higher concentration of TeO<sub>2</sub>, but greater at intermediate frequencies for lower concentrations. For high concentrations of TeO<sub>2</sub> (75-80%), low Na concentration makes significant difference in the observed spectra, but increasing the Na/Zn ratio does not make much difference. For low TeO<sub>2</sub> concentrations (60-65%), these effects are not so obvious, probably because there are not enough tellurium atoms present. These effects are connected to the number of NBO atoms in the glass and the way these influence the glass

network. However, with few Te-O-Te linkages, there are too few  $\text{TeO}_4$  units for an effective network reconstruction.

Increasing the Zn/Te ratio, while keeping  $\text{Na}_2\text{O}$  constant at 5%, results in an increase in the ratio of the peak intensities, A/C. This in turn reflects an increase in the number of NBO atoms. Equivalently, this corresponds to the loss of Te-O-Te bridges, which is also reflected in the transfer of intensity from the E peak to a lower F frequency peak. Contrary to binary alkali tellurites, peaks C increases in magnitude with increasing Zn concentration. According to these observations, the presence of Zn modifies the network, i.e. introduces NBO atoms. This is consistent with the formation of  $\text{Te}_3\text{O}_8$  units, having four NBO atoms and two Te-O-Te bridges each. For high Zn/Te ratios that are sufficient to induce the formation of  $\text{Te}_3\text{O}_8$  units, the substitution of Na for Zn inhibits the linking of these units into chains or more elongated structure.

The B peak might be a stretching mode of Te-O bonds in Te-O-Te bridges or Te-NBO stretch in which more weakly connected oxygen atom also interacts (although more weakly) with other Te ions as in  $\text{TeO}_{3+1}$ . The reason why B does not change much might be that there are many different ways to have NBO atoms and many different kinds of environment.

The overall intensity of the E peak at  $\sim 440\text{cm}^{-1}$  remains fairly constant relative to the intensity of the C and D peak. This also suggests that the bonds involved in the vibrational modes giving rise to the C and D peaks are also involved in the network modes giving rise to the E peak. The results presented above confirm that the C and D peaks are characteristic of the original  $\text{TeO}_2$  glass and therefore related to the same molecular  $\text{TeO}_4$  units. The other feature revealed by spectra of glasses presented in Table

3.1 is either a transfer of energy from the E peak to a lower frequency peak or a broadening of the E peak towards lower frequencies. Peak ratio E/F decreases with decreasing TeO<sub>2</sub> content. This is expected if the introduction of dopants breaks the Te-O-Te bridges. The reason for a frequency shifted E peak is not entirely clear at this point, but suggests the presence of Te-O-Te bonds in more massive units such as Te<sub>3</sub>O<sub>8</sub>. Also, bonds can be more rigid in these units, leading to a higher frequency of the E peak. Binary ZnO-TeO<sub>2</sub> glasses have a more pronounced peak since there is no sodium to break bonds and all original Te-O-Te and O-Te-O bridges are preserved. As mentioned above, even though increasing Na/Te while keeping Zn constant breaks network bonds, the introduction of Na restores the ~440cm<sup>-1</sup> peak to its original strength. This effect is more pronounced for higher Te concentration when more Te-O-Te or O-Te-O bridges are available.

Creation of larger network units such as Te<sub>3</sub>O<sub>8</sub><sup>4-</sup> may also facilitate certain bonds and their frequencies over the others, for example, Te-O<sub>eq</sub> over Te-O<sub>ax</sub>. Such trend would be visible from the relative intensities of vibrational modes representing vibrations of those bonds. Due to their bigger effective mass, we expect their (mostly torsional or phonon-like) vibrational frequencies significantly lower than vibrational frequencies of Te-O<sub>eq</sub> or Te-O<sub>ax</sub> bonds. Thus, we observe more closely the Raman spectra of zinc-tellurite glasses for Na/Zn substitution, while TeO<sub>2</sub> is kept constant, shown at FIG. 5.1. Overall, the whole low frequency band is more intense in case of 35% ZnO. At the same time, the ratio of the number of Te-O<sub>eq</sub> over Te-O<sub>ax</sub> bonds increases, which we see as increase of intensity of the peak at ~780cm<sup>-1</sup>, due to creation of TeO<sub>3</sub> from TeO<sub>4</sub> units. For increasing concentrations of zinc, the number of Te<sub>3</sub>O<sub>8</sub> units also increases, allowing

them to connect in larger chain-like  $(\text{Te}_3\text{O}_8)_n$  units. Larger units may allow greater electron movement, which would increase the electronic part of polarizability. This will be discussed in details in 5.3.1.

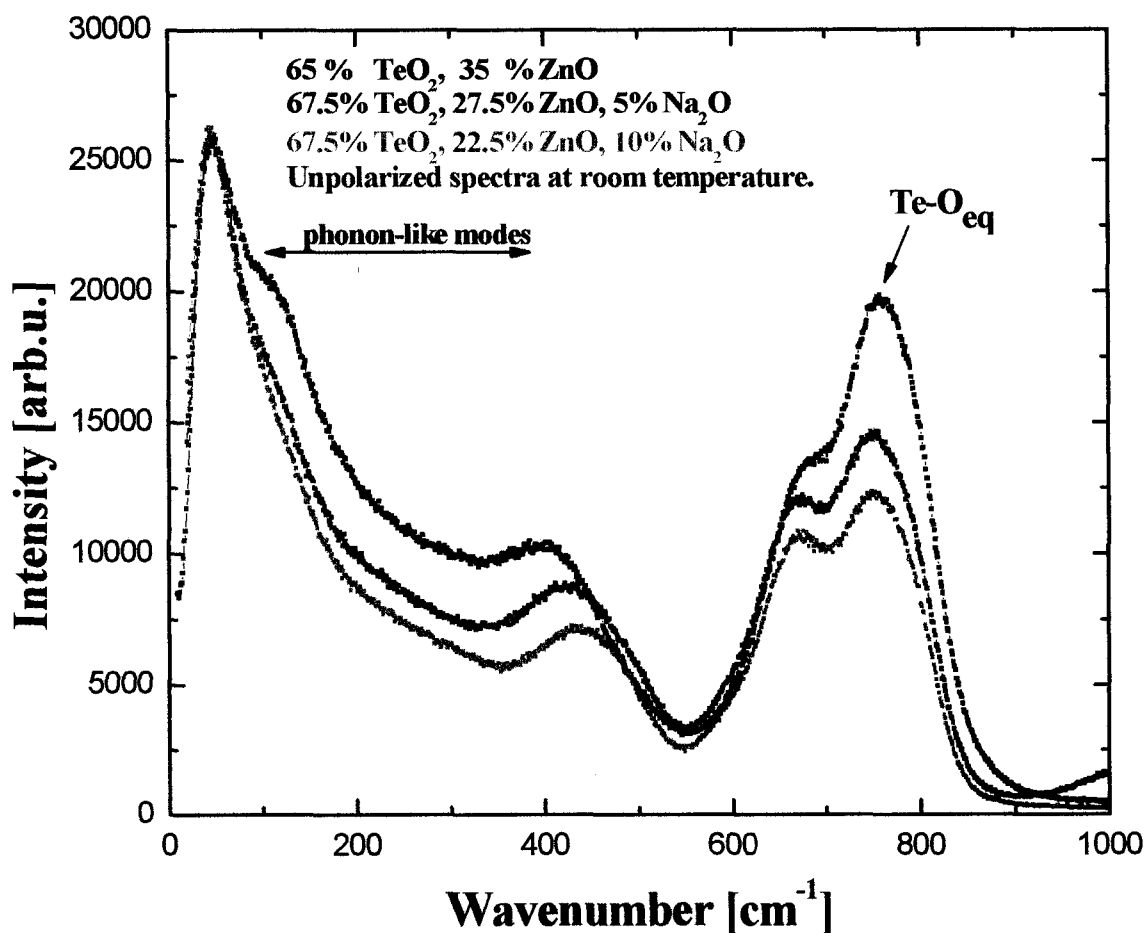


FIG. 5.1 Raman spectra of  $x\text{Na}_2\text{O} \cdot (1-x-y)\text{ZnO} \cdot y\text{TeO}_2$  glasses.

It was shown earlier (see Table 2.2) that the density of tungsten-tellurite glasses increases as  $\text{WO}_3$  concentration increases, due to an increase of the glass molar volume. Shaisha *et al.*<sup>4</sup> and Nasu *et al.*<sup>5</sup> associated this molar volume increase to the increase of the number of  $\text{WO}_4$  units, which they assumed to occupy a smaller space than  $\text{WO}_6$



octahedra. The relative intensity of the band around  $930\text{ cm}^{-1}$  was also shown to decrease continuously with respect to all other bands as  $\text{WO}_3$  content increase above 30% [Shaltout *et al.*<sup>6</sup>, Kim *et al.*<sup>7</sup>]. In the glass containing more than 31.5%  $\text{WO}_3$ , more oxygen can be attracted to tungsten ions converting the structure to octahedral configuration.

With increasing tungsten-oxide, the intensity of the peak at about  $350\text{ cm}^{-1}$  increases, together with the intensity of the peaks at about  $720$ ,  $780$  and  $840\text{ cm}^{-1}$ . This suggests that stretching vibrations of W-O-W linkages appear in a broad wave number range, as reported for several  $\text{WO}_3$  crystal spectra [Daniel *et al.*<sup>8</sup>, Becher<sup>9</sup>]. Peaks at about  $780$  and  $840\text{ cm}^{-1}$  come from Te-O and W-O, respectively, simple stretching bond with NBO atoms. These peaks grow when bonds are broken by the addition of dopants. Lower frequency peaks, at about  $620$ ,  $665$  and  $720\text{ cm}^{-1}$  come also from Te-O bonds, but with Te and O bonded as in perfect  $\text{TeO}_2$  glass. They are characteristics of  $\text{TeO}_4$  units, which indicate formation of Te-O bonds. The D Peak at about  $620\text{ cm}^{-1}$  can serve as reference since its intensity is not affected too much by changing dopants concentration. It appears that for particular composition  $10\%\text{Li}_2\text{O}\cdot 24.9\%\text{WO}_3\cdot 65\%\text{TeO}_2$ , tungsten-tellurite has the strongest Raman intensity at  $100 - 400\text{ cm}^{-1}$  wavenumber range and probably achieves maximal network connection. This suggests that such composition would have network topology that would lead to higher glass softening point, higher phonon energy and broader rare-earth emission.

According to the FIG. 4.9, for 25%  $\text{WO}_3$ ,  $\text{Li}^+$  as modifier mainly affects the Te-O-Te network. From FIG. 4.8, for 20%  $\text{WO}_3$ ,  $\text{Li}^+$  affects both glass sub-networks. For 15%  $\text{Li}_2\text{O}$ , the peak at about  $350\text{ cm}^{-1}$  decreases, as well as the peak at  $460\text{ cm}^{-1}$ , while

the one at  $780\text{ cm}^{-1}$  increase, which is related to the number of NBO atoms. According to these observations, lithium ions clearly break Te-O-Te network bonds. For 5%  $\text{Li}_2\text{O}$ , the intensity of the peaks related to Te-O-Te, W-O-W, and W-O-Te linkages are not affected, since there is not enough  $\text{Li}^+$  to break network bonds.

Looking at the FIG. 4.10, changing the concentration of 10%  $\text{K}_2\text{O}$  to 10%  $\text{Li}_2\text{O}$ , change the whole tungsten-tellurite spectra. Potassium also reduces the number of non-bridging oxygen atoms for both Te and W sub-networks.  $\text{K}^+$  has much bigger ion radius than  $\text{Li}^+$ . When these two are present together in the glass, it looks like  $\text{K}^+$  forces  $\text{Li}^+$  into small sites, so the effect is similar to the one when we put 15%  $\text{Li}_2\text{O}$ . For 5%  $\text{K}_2\text{O}$ , 5%  $\text{Li}_2\text{O}$ , the influence of non-bridging oxygen atoms is even higher and the numbers of linkages decrease (all Te-O-Te, W-O-W, and W-O-Te).

## 5.2 Supporting XPS results

During the analysis of XPS results, excellent fits were obtained with very similar binding energy parameters for a given peak in all the spectra. Greater peak widths indicate a broader distribution of local network environments. The fraction of each type of unit can be estimated from the integrated intensity of the corresponding peak. Results published in [Moawad *et al.*<sup>2]</sup> and presented in FIG. 4.11, reveal that a decrease in  $\text{TeO}_2$ , or a corresponding increase in  $\text{Na}_2\text{O}$  and  $\text{ZnO}$  in sodium-zinc-tellurite glass, results in an increase in the fraction of NBO atoms. This trend intensifies at lower tellurium oxide concentrations.

However, unexpectedly in the 80%TeO<sub>2</sub>·5%Na<sub>2</sub>O·15% ZnO ternary glass, the number of NBO atoms falls below their value in the TeO<sub>2</sub>-ZnO binary glass. This was not expected since sodium breaks the glass network bonds, introducing NBO atoms. In this particular case, it looks like the ternary glass network is better connected than the binary one. This conclusion is further confirmed by a more detailed examination of the XPS results, which indicates that a greater fraction of the TeO<sub>4</sub> units subsists in the ternary with 5% Na<sub>2</sub>O glasses than in both the binary ZnO-TeO<sub>2</sub> or ternary with 10% Na<sub>2</sub>O ones [Moawad *et al.*<sup>2</sup>, Marjanovic *et al.*<sup>3</sup>].

Other important XPS results include the existence of a fourth peak in the Te-3d<sub>5/2</sub> spectrum, shown at FIG. 3.2 (b). This fourth peak, at lower binding energy, can be attributed to a Te<sub>3</sub>O<sub>8</sub> structural unit, in which tellurium has a higher effective charge. This is a supporting evidence for existence of such units in tellurite glasses, which we mentioned in 5.3 as a unit that is possibly responsible for the low frequency modes in the Raman spectra of the ZnO-TeO<sub>2</sub> glasses.

We also compared XPS results on O-1s spectra in zinc-tellurite, FIG. 3.2 (a), and tungsten-tellurite, FIG. 4.11 (a), and found a peak with a slight shoulder in the first, and a single symmetric Voigt (Gaussian- Lorentzian) peak, in the second case. For alkali-silicate glasses, two components attributed to BO and NBO atoms are generally observed [Bruckner *et al.*<sup>10</sup>, Matsumoto *et al.*<sup>11</sup>]. The NBO atoms are detected as a shoulder on the lower binding energy side of the main O-1s peak due to BO. This is the so-called chemical shift, which depends directly on the electron density of the atoms; the higher the electron density around an atom, the lower the binding energy of the ejected photoelectrons [Heo *et al.*<sup>12</sup>]. The O-1s binding energy for alkali tellurite glasses is

smaller than O-1s binding energy for the BO or NBO in alkali silicate glasses (e.g. 531.76 and 529.76 eV, respectively, for 20Na<sub>2</sub>O\* 80SiO<sub>2</sub> glass). It tells us that the electron density on the oxide ions in tellurite glasses is higher than in silicates. In general, for alkali tellurite glass such as Li<sub>2</sub>O-TeO<sub>2</sub>, two components exist in the O-1s spectra. Sekiya *et al.*<sup>13</sup> proposed, through Raman spectroscopic studies, that the NBO atoms that are a part of the TeO<sub>3+1</sub> polyhedra and TeO<sub>3</sub> trigonal pyramid (tp) units were formed in alkali tellurite glass system due to the addition of alkali oxides. Thus, T<sub>g</sub> should decrease with the addition of Li<sub>2</sub>O in the Li<sub>2</sub>O-TeO<sub>2</sub> system due to the disruption of the network formed by TeO<sub>4</sub> tbp units and the consequent increase of NBO atoms. However, there is no NBO atom indicated in our O-1s peak, indicating a more homogeneous electron distribution from the addition of WO<sub>3</sub> [Lim *et al.*<sup>14</sup>].

The core level peaks of the xK<sub>2</sub>O·(10-x)Li<sub>2</sub>O·25WO<sub>3</sub>·65TeO<sub>2</sub> glass system shift toward smaller binding energy with Li → K substitution in figure when the ionic radius of alkali ions increases in the order of Li < K, presented in FIG. 4.11 (a) and (b). However, there is no shape difference when alkali is mixed and there no shoulders are seen in the spectrum. The chemical shift is due to the change of the electronic density of the atoms [Lim *et al.*<sup>14</sup>].

XPS results also confirm that the density of tungsten-tellurite glasses increases with increasing WO<sub>3</sub> content. In contrast to binary alkali tellurite glasses, the core level spectra of the various elements appear unaffected when TeO<sub>2</sub> is replaced by WO<sub>3</sub>, with the alkali oxide concentration remaining constant. The O-1s spectra do not indicate a clear separation of the bridging and non-bridging oxygen contributions. Thus, we conclude that WO<sub>3</sub> behaves essentially as a network former in tellurite glasses.

### 5.3 High refractive index of tellurite glasses

Of the oxide glasses, tellurite glasses have the largest refractive indices, in the range 1.9-2.3. Furthermore, of all tellurite glasses that we tested, glasses containing  $\text{WO}_3$  present the highest polarizability and, therefore, the highest index of refraction. The relatively high polarizability of the glasses containing  $\text{W}^{6+}$  can be attributed to the empty  $d$  orbitals, higher coordination numbers and relatively large ion polarizability. The high refractive index increases the local field correction at an activator site and leads to large radiative transition probabilities. Based upon the large refractive index and dispersion of tellurite glasses, the nonlinear refractive index is also predicted to be very large [Boling *et al.*<sup>15</sup>].

In Chapter 4, FIGS. 4.15 and 4.18-4.20, it is evident that erbium emission in tellurite glasses is broader and flatter than in silica glasses. The same figures also reveal broader spectra in tungsten-tellurite than in zinc-tellurite. Here, we discuss the main reasons for the dependence of erbium emission on different host material. We discuss two aspects of the emission spectra: first, the overall strength of emission, and, second, the emission at longer wavelengths.

Since the refractive index depends strongly on polarization, as shown by Clausius-Mossotti Eq. (2.15), it is valuable to estimate the value of polarizability  $\alpha$  in crystal and glass compounds. Index of refraction depends upon at least these factors:

- the electronic polarizability of the ion, which increases with the number of electrons in the ion,
- the polarizability of the first neighbor ions,

- the ion electronegativity,
- the nature of the bonds (ionic or covalent),
- the coordination number of the ion,
- the glass network connectivity.
- the field intensity from Coulomb interaction,  $\sim z/\alpha^2$ , where  $z$  is the valence of the ion and  $\alpha$  is the distance of separation between ions,

### *5.3.1 Electronic polarizability and ion electronegativity in doped tellurite glasses*

As we can see from the Table 2.3, the average electronic polarizability of glasses with zinc oxide decreases with increasing zinc concentration, while the trend is the opposite in case of tungsten. This is probably due to a slower decrease in average electronegativity of the tungsten-tellurite system compared with the average electronegativity of the zinc-tellurite one, as calculated according to (2.21).

From Table 2.2 we see that the density, linear refractive index and polarizability per unit volume all decrease with increasing concentration of dopants in all cases, except with tungsten where the trend is the opposite. Valence and coordination number are highest in the case of tungsten-tellurite glass. With the substitution of alkali oxide  $M_2O$  for  $TeO_2$  in alkali-tellurite glasses, bridging  $Te-O-Te$  bonds are broken, and non-bridging  $Te-O-M^+$  bonds are formed. The NBO bonds have a much greater ionic character and much lower bond energies. Consequently, the refractive index  $n$  of  $TeO_2-M_2O$  glass mainly depends on the electronic polarizability  $\alpha$  of  $M$ , as listed in Table 2.2. The molar polarizability  $\alpha_m$  decreases with increasing concentrations of alkali-metal oxide. This can

be explained by a decrease in the number of polarizable atoms/unit volume,  $N/V$ , for each binary glass system, according to the molecular percent portion of the metal oxide [El-Mallawany<sup>16</sup>]. Multicomponent glass generally behaves in a similar manner.

We have used alkaline ions such as sodium and lithium to open the glass network, and zinc or tungsten as network formers. As NBO ions replace bridging-oxygen ions in the glass structure, the glass network is less well connected. However,  $O_{\text{NBO}}\text{-Zn}^{++}\text{-O}_{\text{NBO}}$  bonds facilitate the network restoration by forming new units, such as  $\text{Te}_3\text{O}_8$ , which has four NBO ions available for bonding with neighboring ions and units. These units can connect in a chain-like structure, shown in FIG. 5.2, as they are found in natural  $\text{Zn}_2\text{Te}_3\text{O}_8$  crystals. The electronic polarizability may increase with electrons now being delocalized in such restored network. As seen in Table 2.3, one can see that refractive index of zinc-tellurite glass is higher than that in sodium-tellurite glass. This effect appears to be even stronger using tungsten as a network former.

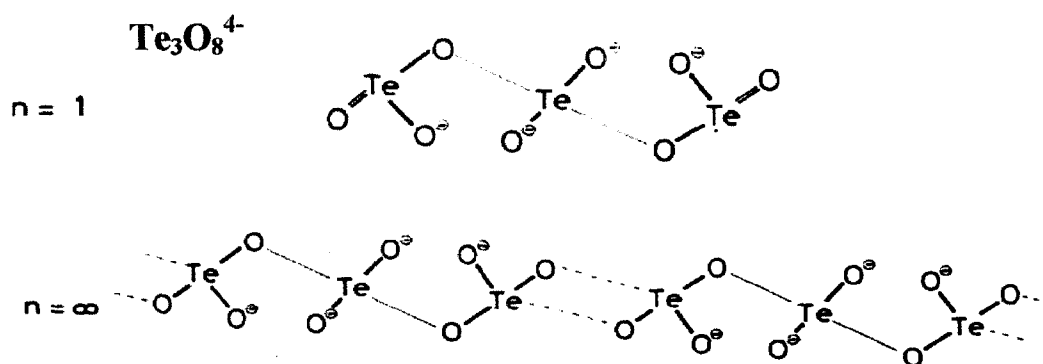


FIG. 5.2 Chain-like  $\text{Te}_3\text{O}_8^{4-}$  units, present in  $\text{ZrTe}_3\text{O}_8$  crystals.

### 5.3.2 Dependence of polarizability on the nature and the number of network bonds

As we stated above, the value of polarizability  $\alpha$  in crystal and glass compounds depends on the nature and the number of bonds, among the other factors. We calculate the number of network bonds per unit volume using the bond compression model for the multicomponent glass of the formula  $x A_{n1} O_{m1} - (1-x) G_{n2} O_{m2}$ , as:

$$n_b = n_f N_f, \quad (5.1)$$

where  $n_f$  is the coordination number,  $N_f$  is the number of formula units per unit volume ( $= x N_A \rho / M_g$ ),  $x$  is the mol % of the oxide,  $\rho$  is the density, and  $M_g$  is the molecular weight of the glass. Calculated values are given in Table 5.1.

Glass	Modifier	$M_g$	$\rho$	$n_f$	$n_b \times 10^{22} (\text{cm}^{-3})$
TeO <sub>2</sub>	...	159.61	5.67	4	8.558
	10.0	151.79	5.556		9.258
	20.0	140.075	5.534	Te – 4	10.469
TeO <sub>2</sub> -ZnO	30.0	128.366	5.465	Zn – 6	11.795
	10.0	166.825	5.73		8.688
	20.0	174.05	5.892	Te – 4	8.970
TeO <sub>2</sub> -WO <sub>3</sub>	30.0	181.275	5.984	W – 6	9.146

Table 5.1 Number of network bonds per unit volume for ZnO and WO<sub>3</sub> tellurite glass.

With increasing concentration of both Zn and W, the number of network bonds increases, with a faster increase in the case of zinc. These might be also due to the size difference of these two atoms. Although tungsten creates fewer network bonds per unit volume than zinc, it is still a better network former because of its tendency to form its own strongly bonded sub-network around the tellurite one. The higher value of the W-O



bond strength, the stronger tendency of tungsten to form covalent bonds with oxygen, its higher polarizability and higher coordination numbers ( $\text{WO}_6$ ), all concur to pull the oxygen atoms away from the basic tellurite network. Two networks are then connected via W-O-Te, O-W-O, and O-Te-O linkages, which overall make a tungsten-tellurite glass network well connected.

### 5.3.3 Dependence of polarizability on network connectivity

Network connectivity depends on the type of units presents and is related to the bond strength and length, the coordination number, and the force constant which can be calculated according to the relation  $F = 17/r^3$  [Bridge & Higazy<sup>17</sup>]. Internuclear distances  $r$ , calculated force constants  $F$  and bond strengths  $D_{298}^\circ$  for some natural diatomic molecules are given in Table 5.2.

Molecule	Internuclear distance $r$ (Å)	Force constant (N/m)	Bond strength $D_{298}^\circ$ (kJ/mol)
K-K	3.9051	28	54.63±0.002
K-Li	...	...	82.0±4.2
K-O	...	...	277.8±20.9
Li-Li	2.6729	89	110.21±4
Li-O	1.68822	353	335±8.4
Zn-Zn	...	...	29
Te-Zn	...	...	117.6±18.0
Te-Te	2.5574	102	257.6±4.1
O-O	1.20752	966	...
O-Zn	1.988	219	159±4
O-Te	1.90-2.08	189-248	376.1±20.9
O-W	1.8-1.93	236-291	672.0±41.8
Na-O	2.05155	197	256.1±16.7
Na-Na	3.0789	58	73.0913±0.0001
Er-Te	...	...	238±42
Er-O	...	...	615±13

Table 5.2 Bond strengths for some natural diatomic molecules.

From Table 5.2, we see that a decrease in internuclear distances results in an increase of the force constant. The force constant is strongest in the case of an O=O bond since it is doubly covalent bond. Therefore, an important observation is the shorter bond distance and stronger force constant of W-O than those of Te-O and Zn-O. Comparing the bond strengths, from the same table, we can see that W-O bonds are the strongest ones, approximately two times stronger than Te-O bonds and more than four times stronger than Zn-O. Tungsten-oxygen bonds are more covalent and more polarizable than Zn-O and Te-O bonds. Moreover, the bonds between the two sub-networks via previously NBO atoms, Te-O-W, also contribute to an overall well connected tungsten-tellurite glass network. The above-mentioned reasons explain why tellurite network is more strongly connected when zinc is replaced by tungsten.

Tellurite oxide has a relatively high average polarizability (Table 2.3), just like other *d* transition-metal oxides, which is attributed to the empty *d* states of the corresponding cations. Still, they belong to the group of oxides with medium polarizing effect of the oxide ion by the cation (with 2-3 Å<sup>3</sup>) [Dimitrov & Sakka<sup>18</sup>, Kordes<sup>19</sup>]. Atoms characterized by low ion polarizability include Si, B, Al, Ge and Ga (with 1-2 Å<sup>3</sup>), but there is a group of elements that form oxides with an average polarizability above 3 Å<sup>3</sup>, such as Cd, Pb, Ba, Sb, and Bi. These latter cations possess very high polarizabilities, large ionic radii [Lide<sup>20</sup>] and very small cation field strengths that do not strongly affect the electron charge cloud of the anion.

Some authors claim that the lone pair in the valence shell is the reason for very high polarizability. Interestingly enough, Te<sup>4+</sup> ion possesses a lone pair in the valence shell, similarly to Bi<sup>3+</sup>, Sb<sup>3+</sup> and Pb<sup>2+</sup> [Galy *et al.*<sup>21</sup>]. According to Gillespie [Gillespie<sup>22</sup>],

a repulsive force act between different electron pairs in the coordination polyhedra of the cation. It is known that the bond-pair – bond-pair (bp-bp) repulsion is smaller than the bond-pair – lone-pair (bp-E) repulsion. This may lead to an additional relaxation of the cation polarizing effect on the anion. In addition, the cation - lone pairs (M-E) distance increases from  $\text{Pb}^{2+}$  (1.16 Å) to  $\text{Sb}^{3+}$  (1.18 Å) and to  $\text{Te}^{4+}$  (1.26 Å) [Kordes<sup>19</sup>]. The repulsion of the bp-E decreases by the same magnitude, resulting in an increase of the polarizing effect of the cation. Moreover, the decrease of  $\text{M-O}_{\text{ax}}$  (axial bonds) and  $\text{M-O}_{\text{eq}}$  (equatorial bonds) distance is observed from  $\text{PbO}$  (2.22; 2.19 Å) to  $\text{TeO}_2$  (2.09; 1.92 Å). This may explain smaller average oxide polarizability of  $\text{TeO}_2$  than those of  $\text{PbO}$ ,  $\text{CdO}$ ,  $\text{Sb}_2\text{O}_3$  and  $\text{Bi}_2\text{O}_3$ . Still, the bond length could change with environment, so the most desirable glasses for optical applications are definitely not binary ones. It would be interesting to make tellurite glasses with dopants like Cd, Pb, Ba, Sb, and Bi, since their optical properties could be better than those of the glasses used in present research: their index of refraction should be higher than that of sodium-zinc-tellurite glass due to their expected higher average polarizability.

#### 5.4 The role of phonons in erbium emission

Nonradiative decay between  $J$  multiplets in erbium is attributed to phonon-induced emission due to interactions of the orbital moment of the ion with the fluctuating crystalline field [Weber<sup>23,24</sup>]. Nonradiative decay arising from energy transfer to other erbium ions or impurities is assumed to be very small. The simultaneous emission of several phonons is required to conserve energy in a purely nonradiative transition. The

highest-energy optical phonons are the most important for nonradiative processes since they minimize the number of phonons required, and hence the order of the process. For zinc-tellurite glass, as derived from our Raman spectra, the phonon frequencies range up to  $780\text{ cm}^{-1}$ . Attempts have been made to make tellurite glasses with even higher maximal phonon frequency, and tungsten-tellurite glass with a mode at  $\sim 925\text{ cm}^{-1}$  is already a known candidate. Phonon frequencies of silica glass range up to  $1000\text{ cm}^{-1}$  [McIntosh *et al.*<sup>25</sup>]. Thus, slightly more simultaneous phonons for the same nonradiative transition are required in tellurite than in silica glass. Therefore, multiphonon nonradiative transitions from upper excited states are more probable in silica than in tellurite glass, meaning a shorter lifetime of the upper excited energy levels of  $\text{Er}^{3+}$  in silica glass. However, radiative processes from the lowest excited levels  $^4\text{I}_{11/2}$  and, especially,  $^4\text{I}_{13/2}$  to the ground state are more efficient in tellurite than in silica.

Despite significant approximation, Judd-Ofelt analysis is a well-accepted approach and provides useful information on the crystal field, wavefunctions and energy levels, for the comparison of optical materials. To the best of my knowledge, there is no direct relationship between any of Judd-Ofelt  $\Omega_k$  ( $k = 2, 4, 6$ ) coefficients and particular optical properties. Obviously, these coefficients are higher for hosts in which erbium emission is higher, as can be seen from Table 4.2, and compared with other materials from the literature. The  $\text{Er}^{3+}$  emission spectra in tellurite glasses and fibers remain the broadest observed so far. The answer for this may lie in higher erbium emission probabilities in these glasses, because of their higher molar polarizability and refractive indices than those of alumina-silica glasses.

What is clear, though, is that overall emission strength can be significantly influenced by nonradiative multi phonon relaxation processes. The rates of nonradiative decays by multiple phonon emission are not directly observable and their presence and relative importance are established by comparing the measured excited-state lifetime with the total radiative lifetime, with any difference being attributed to the existence of nonradiative transitions. Relaxation processes within a  $J$  crystal field manifold lead to rapid thermal equilibration. However, the order of magnitude of a lifetime broadening is much lower than order of magnitude of nonradiative processes between different manifolds by multiple phonon emission. Multiphonon nonradiative probabilities  $W_{JJ'}$  can be calculated for each manifold. These calculations are not trivial and involve time-dependent perturbation theory. Radiative lifetimes of all upper excited states are significantly shorter than that of  ${}^4\text{I}_{13/2}$ . The radiative lifetime of  ${}^4\text{I}_{11/2}$  level is in the same order of the magnitude as that of the first excited state, but still shorter [Kaminskii *et al.*<sup>26</sup>]. In the glasses that we have studied, there is no evidence for the  ${}^4\text{I}_{13/2}$  level to have direct multiphonon relaxations to reduce its lifetime, mainly due to large energy gap between the  ${}^4\text{I}_{13/2}$  and the ground state. However, there are resonant electron-phonon relaxations, which reduce the  ${}^4\text{I}_{13/2} \rightarrow {}^4\text{I}_{15/2}$  lifetime. Phonon sidebands of the main 1530 nm peak at FIGS. 4.21 (b), 4.23 (b), and 4.26 (b) and (c), are sign of resonant electron-phonon coupling [Hüfner<sup>27</sup>].

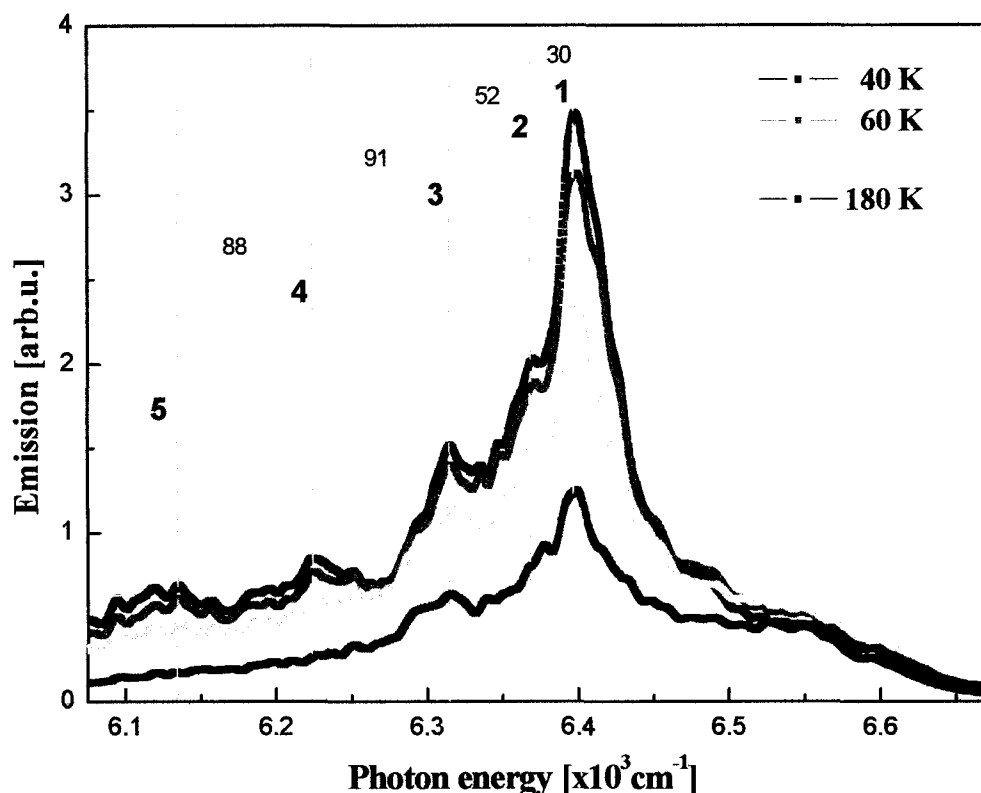


FIG. 5.3 Emission spectra of  $\text{Er}^{3+}$  emission in  $\text{TeO}_2$  fiber at different temperatures.

In order to explain how erbium emission broadens toward lower energy transitions in the tellurite host, we plot in FIG. 5.3, the emission spectra of  $\text{Er}^{3+}$  emission previously shown in FIG. 4.19 (a), but this time as a function of frequency/energy. Robinson [Robinson<sup>28</sup>] suggested distorted octahedral molecule symmetry for erbium in silica, which has a point group  $D_4$  with eight energy levels that belong to eight irreducible representations. This is very interesting since on FIGS. 4.25 and 5.3 we see five different peaks instead of eight. Because of the selection rules for  $^4\text{I}_{13/2} \rightarrow ^4\text{I}_{15/2}$  transition, the five major peaks indicate a close to octahedral symmetry  $O$ , with five irreducible representations, for the  $\text{Er}^{3+}$  ions in  $\text{TeO}_2$  host. Thus, we assume the full octahedral symmetry of erbium in tellurite.

For crystalline rare earth ( $4f^n$ ) spectra, the spin-orbit effects are larger than the crystal field effects [Burns<sup>29</sup>]. Adding spin-orbit coupling effects to  $D_4$  indeed raises the symmetry to  $O$ . It is possible that higher erbium solubility in tellurite glasses, which leads to higher erbium concentrations, increases the influence of these effects.

In Table 5.3, we present the energy separation between emission peaks, which correspond to the separation between the Stark split energy levels of the ground state manifold.

No.	1	2	3	4	5	6	7	8	9	10	11	12	13	14	15	16	17	18	19	20
$\Delta\nu[\text{cm}^{-1}]$	30	52	60	82	88	91	104	118	121	140	143	170	176	179	209	231	264	273	342	364

Table 5.3 The energy separation between emission peaks observed in FIG. 5.3.

Comparing with the phonon energies measured by Raman, such phonons can contribute to electron-phonon resonant processes that may enhance the erbium emission. However, such coupling may occur only if phonons match the energy difference between sublevels of the ground state, as schematically shown at FIG. 5.4: dipole transition directly depends on vibrational and electronic parts of involved energy states,  $\langle a_{v,e} | ED | b_{v',e'} \rangle$ . The transition at  $1.53 \mu\text{m}$  is a direct emission from the first excited  $^4\text{I}_{13/2}$  to the ground  $^4\text{I}_{15/2}$  state and does not involve phonons (zero phonon transition); the other transitions can be phonon assisted.

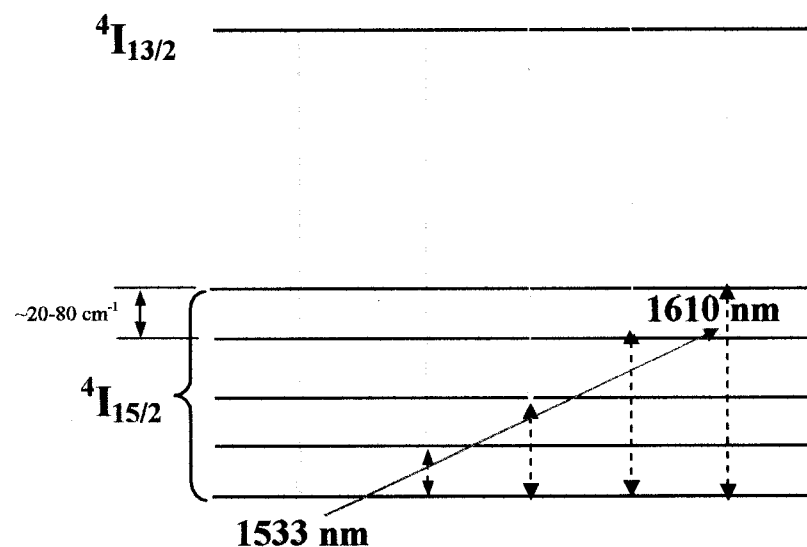


FIG. 5.4 Schematic figure of electron-phonon resonant coupling process.

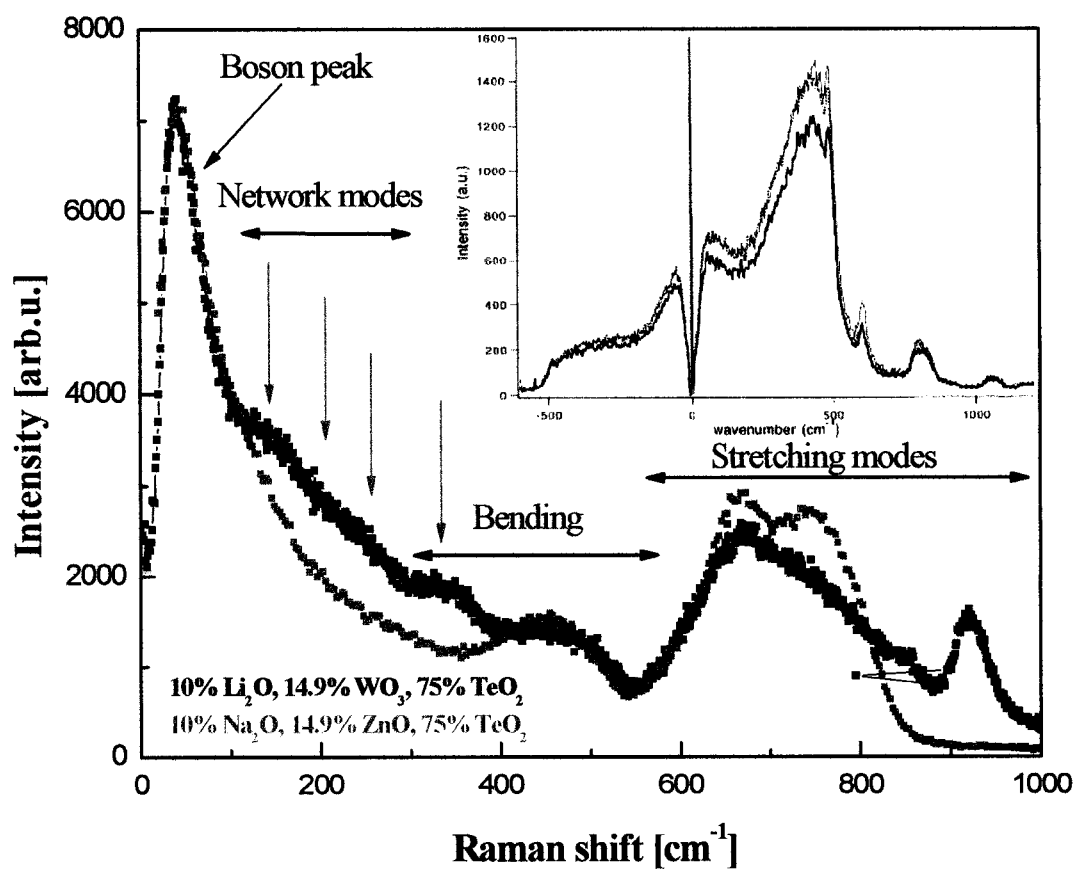


FIG. 5.5 Raman spectra of zinc- and tungsten-tellurite glass.

Inset shows Raman spectra of silica glass [Champagnon *et al.*<sup>30</sup>], for comparison.



Looking for a “recipe” to design a good host for erbium ions, we look for glass materials with phonons at frequencies in the range between 100 and 400  $\text{cm}^{-1}$ . Presented in FIG. 5.5 are Raman spectra of zinc- and tungsten-tellurite glass. The main spectral difference between the Raman spectra of two tellurite glasses is the low frequency region, between 100 and 400  $\text{cm}^{-1}$ . Thus, we expect stronger electron-phonon coupling in tungsten-tellurite than in zinc-tellurite glass, which will lead to higher low energy transition probabilities and broadening of the emission at longer wavelengths. The inset shows Raman spectra of silica glass taken from the literature for comparison. It shows that silica glass possesses a strong bending mode at 440  $\text{cm}^{-1}$  but not so strong a Boson peak as in tellurite glass and no peaks between those two. Broader erbium emission in tellurite than in silica can be now easily associated to the lack of phonons in silica glass at desired wavenumber range.

The effect of higher transition probabilities for low energy transitions is even more important in fibers in tungsten-tellurite than in the zinc-tellurite host. Even small emission differences in bulk materials can be further enhanced along the fiber because Raman scattering intensity increases with increasing length of the fiber. We showed this effect in erbium-doped fibers made of alumina-silica and zinc-tellurite glasses (see FIG. 4.16).

As we said above, the existence of phonon-like modes at low frequencies provides electron-phonon coupling. We argued [Moawad *et al.*<sup>2</sup>, Marjanovic *et al.*<sup>3</sup>] that such phonons could arise from torsional vibrations of chain-like  $\text{Te}_3\text{O}_8$  structure, which is present in zinc-tellurite and  $\beta$ -form of crystalline tellurite [Sekiya *et al.*<sup>1</sup>], shown in FIG.

5.2. A structure of tungsten-tellurite glass, with overall better connected network ( $\text{WO}_6$ , W-O-T and W-O-W) leads to a higher intensity of these phonon-like modes due to higher W polarizability.

Other evidence for the role of phonons in erbium emission are experimental findings that show that there is indeed a coupling to the lattice vibrations because the temperature-dependent linewidths, caused by electron-phonon coupling. Transitions that involve simultaneous excitation of an electron and a phonon (phonon sidebands) are observed [Hüfner<sup>27</sup>]. These two experimental observations demonstrate the possibility of the vibrational coupling, and mixing excited configurations into the  $4f^n$  ground state configuration. Hellwege [Helwege<sup>31</sup>] has shown that for rare earth ions, electron-phonon coupling is strongest at the beginning and the end of rare earth series and weakest in the middle. This can be interpreted to mean that ions like  $\text{Pr}^{3+}$ ,  $\text{Nd}^{3+}$ ,  $\text{Er}^{3+}$ , and  $\text{Tm}^{3+}$  are likely to show a strong vibrational coupling contribution, whereas for ions like  $\text{Sm}^{3+}$ ,  $\text{Eu}^{3+}$ , and  $\text{Gd}^{3+}$  the finite ED transition probability is mostly due to the crystal field [Hüfner<sup>27</sup>].

Another factor that affects the transition probability of emission spectra in fibers is re-absorption and re-emission processes along the fiber. Spectral differences within different host materials are enhanced with increasing fiber length, due to these processes. Thus, we expect to have even broader or at least shifted towards longer wavelengths ASE spectra in fibers made of host materials that have stronger emission in bulk glass at certain wavelengths than other glasses. For example, beside the electron-phonon coupling effect, zinc- and tungsten-tellurite fibers should have broader or shifted towards longer wavelengths ASE than alumina-silica fibers for the same fiber length, due to re-

absorption and re-emission processes. This may provide an additional explanation for the broader ASE spectra in zinc-tellurite than in alumina-silica fiber (FIG. 4.18).

## Bibliography

- [1] T. Sekiya, N. Mochida, A. Soejima, *J. Non-Cryst. Solids* **191** (1995) 115.
- [2] H.M. Moawad, J. Toulouse, H. Jain, A.R. Kortan, Conference preceding, *Proceedings of 103rd Annual Meeting & Exposition of the ACerS Symposium on Optoelectronic and Technology in the Information Age*, **126** (American Ceramic Society, 2001), p. 45.
- [3] S. Marjanovic, J. Toulouse, H. Jain, C. Sandmann, V. Dierolf, A.R. Kortan, N. Kopylov, R.G. Ahrens, *J. Non-Cryst. Solids* **322** (2003) 311.
- [4] E.E. Shaisha, A.A. Bahgat, A.I. Sabry, *J. Mater. Sci. Lett.* **5** (1986) 687.
- [5] H. Nasu, T. Uchigaki, K. Kamiya, H. Janbara, K. Kubodera, *Jpn. J. Appl. Phys.* **31** (1992) 3899.
- [6] I. Shaltout, Yi Tang, R. Braunstein, A.M. Abu-Elazm, *J. Phys. Chem. Solids* **56** (1995) 141.
- [7] S.H. Kim, T. Yoko, S. Sakka, *J. Am. Ceram. Soc.* **76** (1993) 2486.
- [8] M.F. Daniel, B. Desbat, J.C. Lassegues, B. Gerand, M. Figlarz, *J. Solid State Chem.* **67** (1987) 128.
- [9] H.J. Becher, *J. Less-Common Met.* **76** (1980) 169.
- [10] R. Bruckner, H. U. Chun, H. Goretzki, *Glasstech. Ber.* **51** (1978) 1.

- [11] S. Matsumoto, Y. Miura, T. Nanba, A. Osaka, *Proceedings of 17<sup>th</sup> Int. Congress on Glass*, Vol. **3** (1995) 72.
- [12] J. Heo, D. Lam, G.H. Sigel, Jr., E.A. Mendoza, D. A. Hensley, *J. Am. Ceram. Soc.* **75** (1992) 277.
- [13] T. Sekiya, N. Mochida, A. Ohtsuka, M. Tonokawa, *J. Non-Cryst. Solids* **144** (1992) 128.
- [14] J. W. Lim, H. Jain, J. Toulouse, S. Marjanovic, J. S. Sanghera, R. Miklos, I. D. Aggarwal, *Proceedings of the 16<sup>th</sup> University Conference on Glass Science*, (RPI, Troy, NY, 2003).
- [15] N.L. Boling, A.J. Glass, A. Owyong, *IEEE J. Quantum Electron.* **14** (1978) 601.
- [16] Raouf A.H. El-Mallawany, *Tellurite Glasses Handbook* (CRC Press, Boca Raton, 2001).
- [17] B. Bridge, A. Higazy, *Phys. Chem. Glasses* **27** (1986) 1.
- [18] V. Dimitrov, S. Sakka, *J. Appl. Phys.* **79** (1996) 1736.
- [19] E. Kordes, *Z. Phys. Chem. B* **44** (1939) 249.
- [20] D.R. Lide (Ed.), *Handbook of Chemistry and Physics*, 80<sup>th</sup> edit. (CRC Press, Boca Raton, 1999).
- [21] J. Galy, G. Mennier, S. Andersson, A. Aström, *J. Solid State Chem.* **13** (1975) 142.
- [22] R.J. Gillespie, *Molecular Geometry* (Van Nostrand Reinhold, London, 1972).
- [23] M.J. Weber, *Phys. Rev.* **156** (1967) 231.
- [24] M.J. Weber, *Phys. Rev.* **157** (1967) 262.
- [25] C. McIntosh, J. Toulouse, P. Tick, *J. Non-Cryst. Solids* **222** (1997) 335.

- [26] A.A. Kaminskii, V.S. Mironov, A. Kornienko, S.N. Bagaev, G. Boulon, A. Bernier, B. Di Bartolo, *Phys. Stat. Sol. (a)* **151** (1995) 231.
- [27] S. Hüfner, *Optical spectra of transparent rare earth compounds* (Academic Press, New York, 1978).
- [28] C.C. Robinson, *J. Non-Cryst. Solids* **15** (1974) 1.
- [29] G. Burns, *Introduction to group theory with applications* (Academic Press, Boston, 1997).
- [30] B. Champagnon, C. Chemarin, E. Duval, R. Le Parc, *J. Non-Cryst. Solids* **274** (2000) 81.
- [31] K.H. Hellwege, *Ann. Phys.* **40** (1941) 529.

## Chapter 6

### Conclusion

This study provides fundamental physical understanding of the strong and wide erbium emission in tellurite glasses and fibers. Studying the glass network and Raman characteristics of tellurite helped understanding the fundamental origin of their optical properties. We investigated zinc-tellurite and tungsten-tellurite glasses and fibers and compared them with alumina-silica ones.

Our study showed that ZnO addition in TeO<sub>2</sub> glass enables the reconstruction of glass network. We also showed that sodium dopant provides an additional structural degree of freedom by breaking the Te-O bonds. More specifically, we argued that Zn promotes the formation of new Te<sub>3</sub>O<sub>8</sub> units, from TeO<sub>4</sub> molecular units that have been disconnected by Na. Increasing the concentration of Zn results in the linking of these units into chains. Therefore, sodium opens the glass network and allows zinc to create a new network.

Unexpectedly, in the 80%TeO<sub>2</sub>·5%Na<sub>2</sub>O·15%ZnO ternary glass, the number of NBO atoms fall below their value in TeO<sub>2</sub>-ZnO binary glass. This was not expected since sodium breaks the glass network bonds, introducing NBO atoms. In this particular case, it looks like ternary glass has better connected glasses form a network than binary one. This conclusion is further confirmed by a more detailed examination of the XPS results, which indicates that a greater fraction of the TeO<sub>4</sub> units subsists in the ternary with 5% Na<sub>2</sub>O glasses than in both the binary ZnO-TeO<sub>2</sub> or ternary with 10% Na<sub>2</sub>O ones.

The emission probabilities are significantly influenced by nonradiative multi phonon relaxation processes. Tellurite glasses have maximal phonon frequency in the range of  $780\text{ cm}^{-1}$  (in pure and zinc-tellurite glass) and  $930\text{ cm}^{-1}$  (for tungsten-tellurite), which is of a great importance for non-radiative transitions from upper energy levels. The highest-energy optical phonons are the most important for nonradiative processes since they minimize the number of phonons required, and hence the order of the process. This leads to a shorter lifetime of excited energy levels of  $\text{Er}^{3+}$  in tellurite glass and, thus, to more efficient radiative processes from the lowest excited levels  $^4\text{I}_{11/2}$  and, especially,  $^4\text{I}_{13/2}$  to the ground state.

These glasses also have a strong Raman scattering intensity at low phonon frequencies, which is very important because that frequency range corresponds to the Stark splitting of the ground state of  $\text{Er}^{3+}$  ions. This allows efficient resonant electron-phonon processes, which may be the main reason for the broader emission in glasses with strong phonon frequency in  $100 - 400$  wavenumber range, as in tungsten-tellurite glasses. We expect stronger electron-phonon coupling in tungsten-tellurite than in zinc-tellurite glass, which will lead to higher low energy transition probabilities and broadening of the emission at longer wavelengths. The narrower erbium emission in silica than in tellurite can be now easily associated to the lack of phonons in silica glass in the desired wavenumber range. The effect of higher transition probabilities for low energy transitions in tungsten-tellurite than in the zinc-tellurite host is even more important in fibers. Even small emission differences in bulk materials are enhanced along the fiber because the probability of Raman scattering increases with increasing length of the fiber.

This study also showed that the particular tungsten-tellurite composition 10%Li<sub>2</sub>O·24.9%WO<sub>3</sub>·65%TeO<sub>2</sub> has the strongest Raman intensity at 100 – 400 cm<sup>-1</sup> wavenumber range and achieves maximal network connection. This suggests that such composition has the network topology that should lead to higher glass softening point, higher phonon energy and broader rare-earth emission.

We compared the absorption and emission properties of Er<sup>3+</sup>-doped tellurite and alumina-silica glasses and fibers. The emission properties of erbium and distributed effects of emission in fibers are strong due to a high refractive index of tellurite glass. This increases the local field correction at an activator site and leads to larger radiative transition probabilities. Thus, rare earth ions in tellurite glasses typically have larger stimulated emission cross-sections over a broad bandwidth compared to other binary oxide glasses.

It was shown that the density of tungsten-tellurite glasses increases as WO<sub>3</sub> concentration increases, due to an increase of the glass molar volume. The index of refraction also increases with tungsten oxide concentration. This directly influences the emission probabilities, leading to their increase.

It would be interesting to continue this study with additional CEES measurements in temperature range where “structural transition” was observed. This may show the existence of a different mayor site at different temperatures. Our results verify that tellurite glasses with dopants like Cd, Pb, Ba, Sb, and Bi, will have also good optical properties: their index of refraction should be higher than of zinc-tellurite glasses due to expected higher average polarizability.



## Selected publications

### **“Impurity influence on soft modes in SrTiO<sub>3</sub>”**

S. Marjanovic and Z.V. Popovic, Contemporary Studies in Condensed Matter Physics, Milorad Davidovic and Zoran Ikonc, editors; SFKM '97, *Solid State Phenomena*, Vols. **61-62**, Scitec Publications Ltd. (1998) p. 309.

### **“ASE and laser emission in double-core double-clad EDTF”**

S. Marjanovic, J. Toulouse, A. R. Kortan and N. Kopylov, OSA Trends in Optics and Photonics (TOPS), Vol. **73**, *the Conference on Lasers and Electro-Optics (CLEO)*, OSA Technical Digest, Post-conference Edition (Optical Society of America, Washington, D.C., 2002), p. 18.

### **“Characterization of new erbium-doped tellurite glasses and fibers”**

S. Marjanovic, J. Toulouse, H. Jain, C. Sandmann, V. Dierolf, A.R. Kortan, N. Kopylov, and R.G. Ahrens, *Journal of Non-Crystalline Solids*, Vol. **322**, Issues 1-3, 15 July 2003, p. 311.

### **“Structure of alkali tungsten tellurite glasses by X-ray photoelectron spectroscopy”**

J. W. Lim, H. Jain, J. Toulouse, S. Marjanovic, J. S. Sanghera, R. Miklos and I. D. Aggarwal, Proceedings of *the 16<sup>th</sup> University Conference on Glass Science*, (RPI, Troy, NY, 2003).

**“Erbium emission in highly doped tellurite and alumina-silica novelty fibers”**

S. Marjanovic, J. Toulouse, C. Sandmann, Z. Fleischman, V. Dierolf, M.F. Yan, V.S. Johnson, P.W. Wisk, A.R. Kortan, N. Kopylov, and R.G. Ahrens  
OSA Trends in Optics and Photonics (TOPS), Vol. **95**, the *Optical Fiber Communication (OFC) Conference, OSA Technical Digest*, Post-conference Edition (Optical Society of America, Washington, D.C., 2004), p. 364.

**“Comparison of Er<sup>3+</sup> absorption-emission properties in tellurite and ultra highly doped Al-silica fibers”**

S. Marjanovic, J. Toulouse, C. Sandmann, Z. Fleischman, V. Dierolf, M.F. Yan, V. S. Johnson, P.W. Wisk, A.R. Kortan, N. Kopylov, and R.G. Ahrens  
OSA Trends in Optics and Photonics (TOPS), Vol. **96**, the *Conference on Lasers and Electro-Optics (CLEO), OSA Technical Digest*, Post-conference Edition (Optical Society of America, Washington, D.C., 2004), p. 389

## Selected presentations

**“Effect of doping on the soft modes in  $\text{SrTiO}_3$ ”,**

S. Marjanovic and Z.V. Popovic, *the Symposium on the Condensed Matter Physics*, Kladovo, Yugoslavia (1997).

**“ASE and laser emission in double-core double-clad EDTF”**

S. Marjanovic, J. Toulouse, A. R. Kortan and N. Kopylov, *the Conference on Lasers and Electro-Optics (CLEO)*, Long Beach, CA, USA (2002)

**(Invited Talk) “Erbium-Doped Tellurite Glasses and Fibers: Local Structure, Vibrational Spectra, Fiber Fabrication and Characterization for Amplifier and Laser Applications”**

S. Marjanovic, J. Toulouse, H. Jain, C. Sandmann, V. Dierolf, N. Kopylov, A.R. Kortan and R.G. Ahrens, *the American Ceramic society (ACerS) 104<sup>th</sup> Annual Meeting*, Saint Louis, MO, USA (2002)

**(Plenary/Invited Talk) “Erbium-Doped Tellurite Glasses and Fibers: Raman Spectra, Local Structure, Fiber Fabrication and Characterization for Applications”**

S. Marjanovic, J. Toulouse, H. Jain, C. Sandmann, V. Dierolf, N. Kopylov, A.R. Kortan and R.G. Ahrens, *the Silica and Advanced Dielectrics Symposium*, Trento, Italy (2002)

**“Characterization of Erbium-Doped Tellurite Glasses and Fibers”**

S. Marjanovic, J. Toulouse, H. Jain, C. Sandmann, V. Dierolf, A.R. Kortan, N. Kopylov, and R.G. Ahrens, *the American Physics Society (APS) Meeting*, Austin, TX, USA (2003)

**“Raman Study of the Local Structure and Network Topology of  $\text{Li}_2\text{O-WO}_3\text{-TeO}_2$  Glasses”**

S. Marjanovic, J. Toulouse, J. Lim, H. Jain, J.S. Sanghera, *the American Ceramic Society (ACerS) Glass & Optical Materials Division Fall Meeting*, Corning, NY, USA (2003)

**“Erbium emission in highly doped tellurite and alumina-silica novelty fibers”**

S. Marjanovic, J. Toulouse, C. Sandmann, Z. Fleischman, V. Dierolf, M.F. Yan, V.S. Johnson, P.W. Wisk, A.R. Kortan, N. Kopylov, and R.G. Ahrens, *Optical Fiber Communication (OFC) Conference*, Los Angeles, CA, USA (2004)

**“Network formers or modifiers in tellurite glass: A Raman study”**

S. Marjanovic and J. Toulouse, *the American Physics Society (APS) Meeting*, Montreal, Quebec, Canada (2004)

**“Comparison of  $\text{Er}^{3+}$  absorption-emission properties in tellurite and ultra highly doped Al-silica fibers”**

S. Marjanovic, J. Toulouse, C. Sandmann, Z. Fleischman, V. Dierolf, M.F. Yan, V.S. Johnson, P.W. Wisk, A.R. Kortan, N. Kopylov, and R.G. Ahrens, *Conference on Lasers and Electro-Optics (CLEO)*, San Francisco, CA, USA (2004)

**“Erbium emission in tellurite fibers for potential use in biophysics”**

S. Marjanovic and J. Toulouse, *Physics and Biology: A Materials Approach*, Paris, France (2004)

## **Vita**

Sasha Marjanovic was born on September 9, 1969 in Jagodina, a small town in the heart of Serbia. He graduated as valedictorian of Air Force Academy in September 1989. He started working at the Institute of Physics at the University of Belgrade even before the graduation in 1995 from Physics Department of the same university. He participated in studies of ferroelectrics, especially with perovskites structure. In 1999 he was offered to enter graduate school at Lehigh University, where he joined the group of Professor Jean Toulouse to study erbium emission in tellurite glasses and fibers. He is a co-author of sixteen publications and presentations.